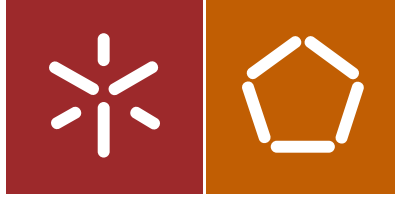


Universidade do Minho
Escola de Engenharia

Vadim Volkov

Phosphorylation of fibrous materials
as a “green” method of their
functional diversification



Universidade do Minho
Escola de Engenharia

Vadim Volkov

Phosphorylation of fibrous materials
as a "green" method of their
functional diversification

Tese de Doutoramento
Engenharia Química e Biológica

Trabalho efectuado sob a orientação do
Professor Doutor Artur Manuel Cavaco-Paulo

April 2015

STATEMENT OF INTEGRITY

I hereby declare having conducted my thesis with integrity. I confirm that I have not used plagiarism or any form of falsification of results in the process of the thesis elaboration.

I further declare that I have fully acknowledged the Code of Ethical Conduct of the University of Minho.

University of Minho, _____

Full name: Vadim Volkov

Signature: _____

Дорогу осилит идущий
(Восточная мудрость)

The walker will prevail over his way
(An Oriental wisdom expression)

Acknowledgments

During my study and stay in Portugal that were not easy, whether from scientific backgrounds, or whether of me being a foreigner, I was fortunate to work in the laboratory of Professor Artur Cavaco-Paulo. Being almost exclusively my own supervisor, Professor Artur made it possible for me to explore the finest virtues of independent, yet challenging, scientific research. Solely now, after the long path passing, I can understand his approach of excellence, whilst he was encouraging me and proposing novel ideas and concepts. For that is why I must express my deepest gratitude to him!

Professor Andreia Gomes, being responsible for the “biological” parts of the research, was extending her aid far beyond the formal duties, thus helping a lot either with physical labor, or with manuscripts preparation. Her helpful advises, physical demonstrations, discussions and comments greatly facilitated the overall experimental and theoretical work.

Notwithstanding, the current research group, assembled and guided by the aforementioned scientists, is a conglomerate of excellent colleagues and friends, always willing to assist at the time of need. I wish just to enumerate those “in the field” whose help was indispensable to me... First of all, Andreia Vasconcelos, my co-supervisor in the beginning. Andreia greatly alleviated the initial problems that always occur when a new person, especially foreigner, comes to the group. Nuno Azoia and Jose Antunes were the guys of solving chemistry-related issues and provided support for any computer or hardware malfunctions in the lab. Celia Cruz granted various protocols for working with keratin, and helped at any rising problem while dealing with this material. In Gualtar division, Marisa Passos made it possible for the immense amount of cell culturing work to operate smoothly, moreover, her part in analyzing statistical data is highly appreciated. Finally, the people of Polymers Department in Azurem division, such as Manuel Oliveira, Mauricio Malheiro and Ana Sofia Abreu assisted in conduction of different spectroscopic and thermoanalytical assays.

I am, therefore, is grateful to all those people, as well as to those whom I occasionally may have forgotten. This work would not be feasible without the support I have been enjoying in the group for almost four years.

Abrços,
Vadim

Abstract

Phosphorylation of fibrous materials as a “green” method of their functional diversification

The current work assesses the possibility of enzymatic modification of fibrous materials for tailoring their physicochemical properties. The need for the material diversification is typically demanded in research and industry, and it stems from the particular applications of the given material. Throughout the years of research, various (bio-) chemical approaches have been established in order to treat and modify fibrous materials. Historically, during the long period of domestication of silkworms and warm-blood animals, different silk and wool types were initially mechanically treated. Later, chemistry was recognized as valuable mean of functionalization of fibrous materials. In the last decades, new types of treatment methods are emerging. These are environmentally friendly, so-called “green chemistry” methods, exploiting the usage of less toxic or hazardous chemicals and biological entities to modify silk and hair (or wool). For instance, recombinant silks can be produced in bacteria and both silk and wool can be enzymatically altered. In addition to saving efforts and lowering the costs, some applications may demand highly discriminating, site-specific modifications of materials of interest that are not available via “conventional” chemical routines. In the latter case enzymes are the best-suited tools for such modifications.

The current work describes three successful applications of *in vitro* enzymatic modification of fibrous materials. The chosen materials are silk fibroin (SF) from *Bombyx mori* (domesticated silkworm) and human hair keratin; the modification is phosphorylation with an ATP as a source of exogenous phosphate group. Protein kinase A from bovine source was the enzyme of choice. Natural fibrous materials are known for their outstanding mechanical properties, environmental stability, biocompatibility and shape control. They often possess a better quality than of man-made materials (*i.e.* polyamide fibers such as nylon).

Silkworm silk is extracted from the cocoons during the sericulture process. Silk has a unique block copolymer structure of large hydrophobic clusters (usually in the form of organized nanoscale crystalline domains, known as β -sheets) and small hydrophilic spacers separating these domains.

Assembled SF is inheritable stable, thus offering a highly stabilizing environment for incorporated compounds.

Keratin is extracted from wool, feathers, horns and other animal sources, including waste by-products of poultry and similar industries. Previously, all the extracted proteins were solely referred to as “keratin”. Nowadays it is established that the term “keratin” actually comprises a mixture of keratins, keratin -associated and some other proteins. It is a potentially useful renewable biopolymer. The step-wise keratin assembly includes several phases. Initially, the primary α -helical chains undergo dimerization, four dimers build up a protofibril. Four protofibrils form a microfibril (or intermediate filament); several microfibrils unite into a macrofibril, which is embedded in intermacrofibrillar material, both surrounded by the cell membrane complex. These fusiform cells are in the hair cortex, which is covered by the cuticle, thus representing the body of a separate hair shaft.

In the last decades, the knowledge on both SF and keratin has considerably increased, regarding their fine structure and molecular biology, similarly to their practical applications in the field of biotechnology. Produced through sustainable, relatively simple and cheap processes, the natural fibrous materials are one of the main raw sources for biomaterial production. Unlike many biologically derived proteins, both silk and keratin are inherently stable to environmental changes and are mechanically robust. Silk and keratin contain several functional groups on the backbone and side chains of their constituting proteins, therefore exerting an ideal components for production of different protein-derived biomaterials.

Therefore, it was of our interest to explore the possibility of “green” treatment of SF and keratin for biomedical (SF) and cosmetic (keratin) applications. The piece of evidence, presented in this thesis, strongly support the idea of enzymatically-mediated *in vitro* modification of both materials. Although high enzymatic specificity, accompanied by steric hindrance, resulted in somewhat low levels of phosphorylation, it was sufficient to cause considerable structural (SF) and chemical (SF and keratin) changes. Tailoring hydrophobicity and self-assembly of SF affected the ability of cultured human fibroblast and Caco-2 cells to attach and proliferate on silk-derived matrices. Moreover, the retention of incorporated Piroxicam and Methotrexate (MTX) drugs was lower in the modified SF. For keratin, the

phosphorylation clearly enhanced the binding of a cationic dye, Methylene Blue (MB), assessed through a keratin-based adsorption system. This facilitated adsorption persisted in various experimental conditions. The obtained results indicate that kinases can be potentially used to diversify both fibrous material types for a wide range of applications. This is particularly important in the fields of biocompatible devices, or any implementations, designed towards a contact with living tissue.

Resumo

Fosforilação como um método “verde” de diversificação funcional dos materiais fibrosos

O presente trabalho avalia a possibilidade de modificação enzimática de materiais fibrosos para alterar as suas propriedades físico-químicas. A diversificação de materiais é normalmente necessária na indústria e investigação, devido às aplicações específicas de um dado material. Ao longo de anos de investigação, várias abordagens (bio-) químicas têm sido estabelecidas a fim de tratar e modificar materiais fibrosos. Historicamente, durante o longo período de domesticação de bichos da seda e animais de sangue quente, os diferentes tipos de seda e lã foram inicialmente tratados mecanicamente. Mais tarde, a química foi reconhecida como um recurso valioso na funcionalização de materiais fibrosos. Nas últimas décadas novos tipos de métodos de tratamento amigos do ambiente estão a emergir. Estes são usualmente denominados de métodos de "química verde", e exploram o uso de produtos químicos menos tóxicos ou perigosos e entidades biológicas para modificar a seda e o cabelo (ou lã). Exemplificando, sedas recombinantes podem ser produzidas em bactérias e tanto a seda como a lã podem ser enzimaticamente modificadas. Além de poupar esforços e reduzir os custos, algumas aplicações podem exigir modificações discriminatórias altamente específicas nos materiais de interesse que não estão disponíveis em rotinas químicas "convencionais". Neste último caso as enzimas são as ferramentas mais adequadas para tais modificações.

O presente trabalho descreve três aplicações bem sucedidas de modificação enzimática *in vitro* de materiais fibrosos. Os materiais escolhidos são fibroína de seda (SF) de *Bombyx mori* (bicho-da-seda domesticado) e queratina do cabelo humano; a modificação é a fosforilação com ATP como uma fonte exógena do grupo fosfato. A proteína quinase A de origem bovina foi a enzima escolhida. Materiais fibrosos naturais são conhecidos por suas excelentes propriedades mecânicas, estabilidade ambiental, biocompatibilidade e controlo de forma, possuindo normalmente melhor qualidade de materiais produzidos por humanos (por exemplo fibras de poliamida, como o náilon).

Seda do bicho-da-seda é extraída a partir dos seus casulos num processo conhecido como sericultura. A seda tem uma estrutura de copolímero em bloco único com grandes aglomerados hidrofóbicos

(usualmente na forma de domínios cristalinos nanoscópicos, conhecidos como folhas- β) separados por pequenos espaçadores hidrofílicos. A SF é intrinsecamente estável, oferecendo assim um ambiente altamente estabilizado para compostos incorporados.

A queratina é extraída de lã, penas, chifres e outras fontes animais, incluindo resíduos do setor avícola e de indústrias semelhantes. Anteriormente, todas as proteínas extraídas eram denominadas apenas como "queratina". Hoje em dia é estabelecido que o termo "queratina" compreende, na verdade, uma mistura de queratinas, queratinas associadas e algumas outras proteínas. É um biopolímero renovável e potencialmente útil. O processo de organização espacial passo a passo da queratina inclui diversas fases. Inicialmente, as cadeias de α -hélice primárias sofrem dimerização, e quatro destes dímeros formam uma protofibrila. Quatro protofibrilas formam uma microfibrila (ou filamento intermediário) e várias microfibrilas se unem numa macrofibrila. Estas últimas estão embebidas no material intermacrofibrilar sendo ambas estruturas rodeadas pelo complexo de membrana celular. Estas células fusiformes estão presentes no cortex capilar, o qual é protegido por uma cutícula, formando assim um feixe de cabelo.

Nas últimas décadas, o conhecimento sobre a SF e a queratina tem aumentado consideravelmente, quer em relação à sua estrutura microscópica e sua biologia molecular, quer às suas aplicações práticas no campo da biotecnologia. Produzido através de processos sustentáveis, relativamente simples e baratos, os materiais fibrosos naturais são uma das principais fontes de matérias para a produção de biomateriais. Ao contrário de muitas proteínas derivadas biologicamente, tanto a seda e a queratina são inerentemente estáveis a mudanças ambientais e são robustas mecanicamente. A seda e a queratina contêm vários grupos funcionais sobre as cadeias principais e laterais das proteínas que as constituem, exercendo assim componentes ideais para a produção de diferentes biomateriais derivados de proteínas.

Portanto, era do nosso interesse explorar a possibilidade do uso de tratamentos "verdes" de SF e queratina para aplicações biomédicas (SF) e para o desenvolvimento de cosméticos (queratina). As evidências, apresentadas nesta tese, apoiam fortemente a ideia da possibilidade de modificação *in vitro* mediada enzimaticamente de ambos materiais. Embora a alta especificidade enzimática, aliada ao impedimento estérico, resultou em níveis relativamente baixos de fosforilação, estes foram suficientes

para causar alterações estruturais (SF) e químicas (SF e queratina) consideráveis. A alteração da hidrofobicidade e da organização estrutural da SF afectou a capacidade de células de fibroblastos humano cultivadas e células Caco-2 em se prenderem e proliferarem em matrizes derivadas de seda. Além disso, a retenção das drogas incorporadas Piroxicam e Metotrexato (MTX) foi menor com a SF modificada. Relativamente à queratina, a fosforilação aumenta claramente a ligação de um corante catiónico, azul de metileno (MB), avaliada por meio de um sistema de adsorção à base de queratina. Esta adsorção facilitado persistiu em várias condições experimentais. Os resultados obtidos indicam que quinases podem ser potencialmente utilizadas para diversificar ambos os tipos dos materiais fibrosos utilizados em uma ampla gama de aplicações. Tal consideração é particularmente importante nas áreas de dispositivos biocompatíveis, ou qualquer implementações, concebidos para um contacto com tecidos vivos.

Table of contents

Acknowledgments.....	iv
Abstract.....	v
Resumo.....	viii
Table of contents.....	xi
List of abbreviations.....	xiv
List of figures.....	xvi
List of tables.....	xxiv
List of equations.....	xxv
Description of the thesis format.....	xxvi
INTRODUCTION CHAPTER (I).....	1
1.1. Fibrous materials: mulberry silk fibroin, a material of choice for the variety of biotechnological applications.....	2
1.2. Fibrous materials: hair keratin and its several usage trends in the context of present research.....	6
1.3. Protein kinase A: a natural catalyst of phosphorylation.....	10
1.4. Principal goals of the work.....	11
CHAPTER II.....	15
Enzymatic phosphorylation of silk fibroins: a platform for the production of tunable materials.....	16
2.1. Introduction.....	17
2.2. Materials and methods.....	18
2.2.1. Materials.....	18
2.2.2. Preparation of silk fibroin solution.....	19
2.2.3. Preparation of phospho-silk fibroin films.....	19
2.2.4. Quantitate determination of phosphate incorporated in phospho-silk fibroin.....	19
2.2.5. Prediction of phospho-sites in silk fibroin.....	20
2.2.6. Fourier transform infra-red (FTIR) spectroscopy.....	20
2.2.7. Secondary structure analysis.....	21
2.2.8. Thermal analysis.....	21
2.2.9. Swelling ratio.....	21
2.2.10. <i>In vitro</i> release.....	21
2.2.11. Cell culture handling.....	22
2.2.12. Cell proliferation assays.....	23
2.2.12.1. Test by indirect contact.....	23
2.2.12.2. Test by direct contact.....	23
2.2.13. Statistical analysis.....	24

2.3. Results.....	24
2.3.1. Preparation of phospho-silk fibroin films.....	24
2.3.2. Chemical and physical properties of silk fibroin.....	25
2.3.2.1. FTIR analysis.....	25
2.3.2.2. Differential scanning calorimetric (DSC) analysis.....	26
2.3.3. <i>In vitro</i> swelling.....	28
2.3.4. <i>In vitro</i> release.....	28
2.3.5. Cytocompatibility of silk fibroin derived materials.....	31
2.4. Discussion and concluding remarks.....	33
S Supplementary material.....	37
CHAPTER III	41
Phosphorylated silk fibroin matrix for methotrexate release.....	42
3.1. Introduction.....	43
3.2. Materials and methods.....	44
3.2.1. Materials.....	44
3.2.2. Preparation of silk fibroin solution.....	45
3.2.3. Preparation of phospho-silk fibroin films and MTX loading.....	45
3.2.4. Quantitate determination of phosphate incorporated in phospho-silk fibroin.....	45
3.2.5. DLS and electrophoretic measurements of silk fibroin and MTX.....	45
3.2.6. Net charge estimations of silk fibroin and MTX.....	46
3.2.7. Thermal analysis of silk fibroin-derived materials.....	46
3.2.8. <i>In vitro</i> release.....	47
3.2.9. Cell culture.....	47
3.2.10. Cell proliferation assay.....	48
3.2.10.1. Test by indirect contact.....	48
3.2.11. Statistical analysis.....	48
3.3. Results.....	49
3.3.1. (Phospho-) silk fibroin solutions: production and net charge estimation.....	49
3.3.2. Optimization of production of MTX-loaded films.....	51
3.3.3. Thermal analysis of silk fibroin-derived films.....	51
3.3.4. <i>In vitro</i> release profiling of incorporated MTX.....	54
3.3.5. Indirect contact effect on cell proliferation.....	58
3.4. Discussion.....	59
S Supplementary material.....	66

CHAPTER IV	71
Enzymatic phosphorylation of hair keratin enhances fast adsorption of cationic moieties.....	72
4.1. Introduction.....	73
4.2. Materials and methods.....	74
4.2.1. Materials.....	74
4.2.2. Preparation of (phospho-) keratin samples.....	75
4.2.3. Infra-red spectroscopic characterization of hair.....	75
4.2.4. Nuclear magnetic resonance spectroscopy of hair.....	75
4.2.5. Methylene blue adsorption/desorption studies.....	76
4.2.6. Acquired data processing.....	76
4.2.7. Sample preparation for confocal microscopy, image acquisition and 3D modelling.....	77
4.3. Results.....	78
4.3.1. Evidence to the phosphorylation of hair keratin.....	78
4.3.2. Preliminary adsorption studies. Calculation of hair adsorption capacity.....	79
4.3.3. Kinetic, modelling and mechanistic aspects of MB adsorption.....	80
4.3.4. Thermodynamic aspects of MB adsorption.....	84
4.3.5. 3D visualization of the hair-bound dye.....	86
4.3.6. Desorption studies of MB dye.....	87
4.4. Discussion.....	88
S Supplementary material.....	95
 CHAPTER V	 101
<i>In vitro</i> phosphorylation as tool for modification of protein fiber materials.....	102
5.1. Introduction.....	103
5.2. Phosphorylation feasibility and its implications on fibrous materials.....	104
5.2.1 The feasibility of phosphorylation reaction.....	104
5.2.1.1. Silk fibroin.....	104
5.2.1.2. Hair keratin.....	105
5.2.2. Phosphorylation implications on fibrous materials.....	106
5.2.2.1. Silk fibroin.....	106
5.2.2.2. Hair keratin.....	110
5.3. Conclusions.....	114
5.4. Further outlook on the feasibility of phosphorylation of fibrous materials.....	115
 REFERENCES	 118

List of abbreviations

[MB] – Methylene Blue starting concentration

3D – 3-dimensional

ϵ – Polanyi potential constant

τ – Time interval, applicable for the model

•OH – Hydroxyl radical

ALP – Alkaline phosphatase

AN – Acrylonitrile

ATP – Adenosine-5'-triphosphate

B.mori – *Bombyx mori*

BCS – Biopharmaceutics Classification System

CTAB – Cetyltrimethylammonium bromide

DDABT – Dimethylpabamidopropyl laurdimonium tosylate

DLS – Dynamic light scattering

D-R – Dubinin—Radushkevich

DRIFT – Diffuse Reflectance Infrared Fourier Transform

DSC – Differential scanning calorimetry

E – Mean energy of adsorption

EO – Ethylene oxide

EtOH – Ethanol

FBS – Foetal bovine serum

FDA – Food and Drug Administration

FTIR – Fourier transform infra-red spectroscopy

H• – Hydrogen radical

H-chain – Heavy chain

HO₂• – Hydroperoxyl radical

HRP – Horseradish peroxidase

K – °Kelvin

k – Interaction constant

K_B – Boltzmann molar gas constant

K_H – Higuchi model-derived constant

K_L – Langmuir effective dissociation constant

K_{RP} – Ritger–Peppas model-derived constant

L-chain – Light chain

LiBr – Lithium bromide

MB – Methylene Blue

MeOH – Methanol
MT – Mushroom tyrosinase
MTS – 3-(4,5-dimethylthiazol-2-yl)-5-(3-carboxymethoxyphenyl)-2-(4-sulfophenyl)-2H-tetrazolium
MTX – Methotrexate
MW – Molecular weight
n – Release exponent
Na₂CO₃ – Sodium carbonate
NP – Non-phosphorylated
NSAIDs – Non-steroidal anti-inflammatory drugs
P – Phosphorylated
PBS – Phosphate-buffered saline
PDI – protein disulphide isomerase
PFO – Pseudo-first order
PKA – Protein kinase A
pNPP – para-Nitrophenylphosphate
PPE – Porcine pancreatic elastase
PSO – Pseudo-second order
PTMs – Post-translational modifications
Q – Adsorption capacity
R – Percentage removal efficiency
R_L – Langmuir separation factor
RSF – Regenerated silk fibroin
SF – Silk fibroin
T_g – Glass transition temperature
TGase – Transglutaminase
UV – Ultraviolet

List of figures

Figure 1.1. Schematic representation of the deduced SF structure. Insets show the fibril overall structure and the fine β -sheet antiparallel alignment of SF polypeptide chains. The image was adapted from [1]3

Figure 1.2. A model, suggesting possible structures of the adsorbed Silk III layers at the air–water interface, obtained at low (**A**) or high (**B**) bulk concentration of silk solution. Figure taken from [2]...4

Figure 1.3. Model of enzymatic degradation of SF crystalline regions. Figure taken from [3].....5

Figure 1.4. Proposed reaction mechanism of ALP with calcium phosphate. Figure taken from [4].....5

Figure 1.5. Evidence to enzymatic phosphorylation of silk. **A.**, autoradiography of reaction. Sample phosphorylation and de-phosphorylation after the indicated hours (in dark blue and red, respectively).

B., ^{32}P transfer to the recombinant silk protein, determined by liquid scintillation. Figure taken from [5]6

Figure 1.6. Accepted model of common wool (and human hair) keratin structure, as appearing in [6]...7

Figure 1.7. The reaction of [2-(acryloyloxy)ethyl] trimethylammonium chloride (2-AE) with a cysteine thiol ($\text{C}-\text{SH}$). Figure taken from [7].....8

Figure 1.8. The cross-linking reaction mechanism catalyzed by TGase, as proposed by [8].....9

Figure 1.9. Preparation of lysozyme-keratin sponge conjugate, after [9].....9

Figure 1.10. Ribbon diagram of PKA co-crystallized with ATP and a peptide inhibitor, as appearing in [15]. Arrows point to the activation loop and the phosphorylation site, p-Thr-197, in the activation loop.....11

Figure 2.1. Dependency between phosphorylated content and the observed silk fibroin protein structure. Amide I resolved curve data for different Silk Fibroin film secondary structures. **A.** Dried films with no treatment. **B.** Dried films, MeOH-treated. **3[10] Helix**, 3_{10} Helix; **Random**, Random coiled structure; **Beta-related**, β -related turns.....26

Figure 2.2. Differential scanning calorimetric analysis of **A.** untreated, **B.** MeOH-treated blended phospho-fibroin films. Individual thermograms of the corresponding samples are shown. T_g values are represented for the untreated group (**A.**, marked by the \blacktriangledown symbol). Crystallization endotherms are designated by the $*$ symbol. Conversely to the MeOH-treated (**B.**). A shift towards lower glass transition temperature and materials' grouping (condensed 0%, 15%; light 30-60%), as function of phosphorylated content, are recognized for untreated phospho-silk fibroin films (**A.**).....27

Figure 2.3. Piroxicam release profiles from silk fibroin films: **A.** enzymatically (subtilisin) mediated. **B.** non-enzymatically (PBS buffer) mediated. Note the arbitrary -1 hour time point, corresponding to MeOH treatment-mediated release of the drug. "Cumulative release" encompasses the total release of

the drug, resulting from MeOH pre-treatment and incubation media as well. The graph is based on one experiment with double sampling.....31

Figure 2.4. The effect of modification degree on cell proliferation, in direct contact measured by MTS and SRB assays. Different letters (a, b) indicate significant differences among treatments. The resulting data are based on three independent experiments.....32

Figure 2.5. Fluorescence microscopy of the cellular proliferation on silk fibroin films with different degrees of phosphorylation. “++” designates a positive control, nuclear stain is Hoechst. Some of the newly divided cells are identified with arrows. Scale bar, 50 μm33

Figure S2.1. An estimation of phosphorylation reaction effectiveness as a function of volume ratio $(\text{Silk fibroin}) / (\text{Other reaction} - \text{constituting reagents})$. The results were normalized according to the control reaction in the absence of protein kinase A. Inset shows the kinetics of the optimized phosphorylation reaction (6:1 volume ratio, favoring silk fibroin) as a function of time. The graph is based on five independent experiments.....37

Figure S2.2. The representation of predicted phosphorylated residues in *B.mori* SF. Asterisks denote the positions, estimated by the software, whilst the remaining sites were deduced upon protein sequence analysis using the consensus motif of protein kinase A. Three major segment types, present in the protein, are indicated. Those include the N-terminal acidic and C-terminal basic domains, and 11 “amorphous” sequences. The rest is repetitive crystalline region [10]. Borders of N- and C-terminal domains are indicated. There is total of 20 estimated phosphorylation sites for each fibroin molecule, of which 14 are found within hydrophobic region and are of primary importance. The only Thr residue undergoing phosphorylation is in the first position from the left, as Ser constitutes the rest of sites. This image was elaborated using the software, included with GPS v2.1 pack [11].....38

Figure S2.3. A. FTIR spectra of non-methanol (MeOH)-treated silk fibroin films of various phosphorylation degrees. Main Amide-related peaks, as well as P-OH deformation vibration-specific peak (of 1039 cm^{-1} , corresponding to the introduced phosphate group, [12]), are indicated. **B.** FTIR spectra of MeOH-treated silk fibroin films of various phosphorylation degrees. Dense β -sheet crystalline structures may prevent the P-OH -specific peak from being detected. The spectral data are based on one experiment with the scan of two different areas.....39

Figure S2.4. Swelling ratio of MeOH-treated phospho-silk fibroin films exposed to different pH conditions (3, 7.4, 11) for 24h. Swelling, or material enlargement due to solvent absorption, was calculated as described in section 3.2.5. The graph is based on one experiment, encompassing two distinct samples tested.....40

Figure S2.5. A. Representative micrograph of L929 live cells adherent to fibroin film with fluorescently labeled nuclei. B. The input field A. , processed by ImageJ v1.42h was used to quantify cell numbers in direct contact assays.....	40
Figure 3.1. Experimental estimation of silk fibroin and methotrexate (MTX) charges as pH function. A. , full-scale representation. B. , zoomed-in representation. The increase of negative charge resulting from phosphorylation is observed. For better clarity, the additional curves, corresponding to material types 15% and 30% (appearing between 0% and 60% types) are relocated to supplementary part.....	50
Figure 3.2. Thermal analysis of silk fibroin films, without (“MTX-”) methotrexate embedded. A. , Fibroin films cast at pH 7.2. B. , Fibroin films cast at pH 3.5. Crystallization peaks are denoted by asterisks. Where possible, the onset temperature glass transition (T_g) is indicated.....	52
Figure 3.3. Thermal analysis of silk fibroin films, with (“MTX+”) methotrexate embedded. A. , Fibroin films cast at pH 7.2. B. , Fibroin films cast at pH 3.5. Several, though not all, methotrexate-related peaks are denoted with arrows. Each arrow type (\blacktriangledown , pseudo-melting or \blacktriangledown , recrystallization coupled to partial decomposition) corresponds to distinct thermal event, resulting from the incorporated MTX.....	52
Figure 3.4. The representation of. DSC curve of methotrexate (MTX) powder. The three main thermal events are indicated. First (\blacktriangledown), pseudo-melting; second (without special designation), solid–solid transition; third (\blacktriangledown), recrystallization coupled to partial decomposition. Due to the specificity of the used procedure (section 4.2.4), MTX dehydration endotherm is not shown in the current presentation.....	53
Figure 3.5. Release profiling of silk fibroin films with incorporated MTX. A. , Fibroin films cast at pH 7.2; B. , Fibroin films cast at pH 3.5. Each curve is an averaged value of the four discrete profiles, corresponding to 0...60% phosphorylated material. Examples of individual release profiles are presented in supporting figure S4.6.....	55
Figure 3.6. Kinetic values, obtained from substitution of MTX release profiling data to Ritger–Peppas (RP) model. The incubation of films in two distinct media (PBS or PPE) was done. Two discrete pH values of 8.0 or 6.2 were used. A. and B. Release exponent n values for different phosphorylated silk fibroin films, computed by model. Direct output of a fitting software. C. and D. For different matrixes, RP model-derived diffusion significative, K_{RP} , was calculated substituting n values to the empirical equation, described previously [13]. Data are reported with standard error and based on one release experiment with double sampling.....	56-57
Figure 3.7. Kinetic values, obtained from substitution of MTX release profiling data to Higuchi model. The incubation of films in two distinct media (PBS or PPE) was done. Two discrete pH values of 8.0 or 6.2 were used. Higuchi diffusion, K_H , values for different phosphorylated silk fibroin films, were computed by the corresponding model. Direct output of a fitting software. Data are reported with standard error and based on one release experiment with double sampling.....	58

Figure 3.8. The viability of Caco-2 cell line, cultivated on lixiviates, derived from 6 hour-incubation of growth medium with silk fibroin MTX-loaded films. A. , pH 7.2-cast films; B. , pH 3.5-cast films. “+” and “-” denote the MTX –loaded or –devoid fibroin materials. DMEM = cell growth medium only, a positive control. MTX = methotrexate at 0.2 mg/ml concentration, a negative control. Statistically significant difference is denoted by asterisk.....	59
Figure S3.1. Theoretical estimation of silk fibroin and methotrexate (MTX) charges as pH function. A. , Full-scale representation. B. , Zoomed-in representation.....	66
Figure S3.2. Experimental estimation of silk fibroin and MTX charges as pH function. A. , Full-scale representation. B. , Zoomed-in representation. Each line is a representative of three sample measurements.....	66
Figure S3.3. A pair-wise comparison of DSC curves corresponding to two main types (acidic- or neutral-pH cast) of elaborated materials. Different films of gradual phosphorylated content, without MTX are presented in panels A. – D. , Where possible, the onset of glass transition temperature (T_g) and crystallization events (*) are indicated.....	67
Figure S3.4. A pair-wise comparison of DSC curves corresponding to the two main types (acidic- or neutral- pH cast) of elaborated materials. Different films of gradual phosphorylated content, with MTX are presented in panels A. – D. , Where possible, the onset of glass transition temperature (T_g) is indicated. Several thermal events, associated with MTX incorporation are marked with the corresponding left-directed arrows. \blacktriangledown – pseudo-melting; \blacktriangledown – recrystallization coupled to partial decomposition. In panel B. , due to graph scaling optimization, some of the curve of 30% type pH 3.5-cast material is truncated.....	68
Figure S3.5. A group representation of DSC curves corresponding to the two main types (acidic- or neutral- pH cast) of elaborated materials, together with MTX only powder. Thermal events, occurring in the pure drug (right-directed arrows) and their presence in MTX-loaded matrixes (left-directed arrows) are shown. \blacktriangledown – pseudo-melting; \blacktriangledown – recrystallization coupled to partial decomposition. A. , Neutral- pH cast films. B. , Acidic- pH cast films. The aberrant 30% type pH 3.5-cast material, similarly to 60% does not show any MTX-derived thermal event. However, because of graph scaling optimization, it almost entirely falls within the Y-axis break range and is not seen.....	69
Figure S3.6. Representative examples of individual profiling curves of MTX release that served as a source for averaging. The bold averaged curves are presented with standard error bars. For simplicity, individual profiles for discrete material types of phosphorylation percentage are shown without error bars. A. , Neutral pH-cast materials, PBS-incubated at pH 8.0. B. , Acidic pH-cast materials, PPE-incubated at pH 8.0.....	70

Figure 4.1. Experimental evidence of hair keratin phosphorylation. A. , DRIFT spectra of hair dust, obtained from its outermost layers. 1 – virgin hair, 2 – chemically damaged (bleached) hair, 3 – bleached and subsequently phosphorylated hair. B. , NMR spectra of keratin peptides, liberated by protease-mediated hair degradation. Top – bleached hair only, bottom – bleached and subsequently phosphorylated hair. C. , schematic representation of protocol, employed for B.  designates a phospho-group.....	79
Figure 4.2. Determination of maximal adsorption capacity (Q_{\max}) for the hair samples of two types. Hair was incubated in MB solutions of varying initial concentration, $[MB]_{\text{init}}$ and Q_{\max} was assessed as described. NP- and P- designate the non-modified or enzymatically modified hair.....	80
Figure 4.3. Time-lapse examination of MB adsorption onto differently treated hair. NP- and P- designate the non-modified or enzymatically modified hair, the digits coming after indicate specific $[MB]_{\text{init}}$. A. , Full-scale representation. B. , Hi-resolution representation of the first hour of incubation..	84
Figure 4.4. Additional factors of dye–hair association, examined in the current study. NP- and P- designate the non-modified or enzymatically modified hair, the digits coming after indicate specific $[MB]_{\text{init}}$. A. , Temperature-dependent adsorption. B. , pH-dependent adsorption.....	86
Figure 4.5. A view from the top of artificially colored 3D visualization of the sites of highest dye affinity (dark-blue) and the bulk hair adsorbent volume (light-gray). A. , non-modified adsorbent. B. , phospho-modified adsorbent. Scale bar, 7 μm	86
Figure 4.6. Time-lapse examination of MB desorption onto differently treated hair. NP- and P- designate the non-modified or enzymatically modified hair, the digits coming after indicate specific $[MB]_{\text{init}}$. A. , Full-scale representation. B. , Hi-resolution representation of the first hour of incubation..	88
Figure 4.7. MB desorption experiments from a differently treated hair. NP- and P- designate the non-modified or enzymatically modified hair, the digits coming after indicate specific $[MB]_{\text{init}}$. A. , Temperature-dependent desorption. B. , pH-dependent desorption.....	88
Figure S4.1. Representation of two different IR techniques for analyzing wool keratin sample. Woven 100% Merino wool fabrics (Albano Antunes Morgado Lda, Portugal) were delipided with cetyltrimethylammonium bromide (CTAB, Cat.nr. H6269, Sigma-Aldrich) and subsequently phosphorylated with protein kinase A (PKA), or left untreated. A. , ATR-FTIR-derived spectra. B. , DRIFT-derived spectra, smoothed prior to final plotting as described in the text.....	95
Figure S4.2. Sensitivity of used NMR equipment to ^{31}P . 2 mM para-Nitrophenylphosphate (pNPP, Cat.nr. P4744, Sigma-Aldrich) in ultra-pure water were scanned as described in the text. 256 transient scans were performed. Inset shows the structure of pNPP.....	96
Figure S4.3. Modelling of MB adsorption onto hair samples. A. , B. and C. correspond to pseudo-first, pseudo-second and intra-particle diffusion models. Q_{equ} and Q_{t} correspond to adsorption capacities at	

experimental equilibrium or at specific time t . All the panels share a common legend, given at bottom. The designations of hair types and dye concentrations are stated in the text.....97

Figure S4.4. Modelling of MB adsorption onto hair samples. **A.** and **B.**, Langmuir-fitted data. **C.** and **D.**, Freundlich-fitted data. **E.** and **F.**, Dubinin–Radushkevich-fitted data. Q_{equ} and $[\text{MB}]_{\text{equ}}$ correspond to adsorption capacities and MB concentration, at experimental equilibrium, respectively. ε is a constant related to the Polanyi potential. Fitting was performed as described in the text.....98

Figure S4.5. The separation factor R_L for (non-) phosphorylated hair. R_L , a Langmuir-derived dimensionless constant, was calculated as described in the text. $[\text{MB}]_{\text{init}}$ corresponds to the initial MB concentration.....99

Figure S4.6. van't Hoff plots for MB dye adsorption onto (non-) phosphorylated hair. $[\text{MB}]_{\text{equ}}$ corresponds to MB concentration at experimental equilibrium, T is temperature in °Kelvin.....99

Figure 5.1. The representation of predicted phosphorylated residues in *B.mori* SF. Asterisks denote the positions, estimated by the software, whilst the remaining sites were deduced upon protein sequence analysis using the consensus motif of PKA. Three major segment types, present in the protein, are indicated. Those include the N-terminal acidic and C-terminal basic domains, and 11 “amorphous” sequences. The rest is repetitive crystalline region [10]. Borders of N- and C-terminal domains are indicated. This image was elaborated using the software, included with GPS v2.1 pack [11] and taken from [157].....105

Figure 5.2. FTIR spectra of SF films of various phosphorylation degrees. Main Amide-related peaks (I, II and III) and phosphorylation-derived peak are indicated. 0%...60% indicate the final phosphorylation degree. Figure was taken from [157].....105

Figure 5.3. Experimental evidence of hair keratin phosphorylation. **A.**, DRIFT spectra of hair dust, obtained from its outermost layers. 1 – virgin hair, 2 – chemically damaged (bleached) hair, 3 – bleached and subsequently phosphorylated hair. **B.**, NMR spectra of keratin peptides, liberated by protease-mediated hair degradation. Top – bleached hair only, bottom – bleached and subsequently phosphorylated hair.....106

Figure 5.4. Phosphorylation impact on silk. **A.**, Dependency between phospho-content and the observed SF secondary structure. **3[10] Helix**, 3_{10} Helix; **Random**, Random coiled structure; **Beta-related**, β -related turns. **B.**, Differential scanning calorimetric analysis of blended phospho-fibroin films. Individual thermograms of the corresponding samples are shown. T_g values are represented (marked by the \blacktriangledown symbol). Crystallization endotherms are designated by the $*$ symbol. A shift towards lower glass transition temperature as function of phosphorylated content, is recognized. Resulting figure is compiled from [157].....108

Figure 5.5. Schematic illustration of SF solution gelation development. The steps of fibroin gelation are shown as a three-stage model, according to [16].....	109
Figure 5.6. The viability of Caco-2 cell line, cultivated on lixiviates, derived from 6 hour-incubation of growth medium with silk fibroin MTX-loaded films. A. , pH 7.2-cast films; B. , pH 3.5-cast films. “+” and “-” denote the MTX –loaded or –devoid fibroin materials. DMEM = cell growth medium only, a positive control. MTX = methotrexate at 0.2 mg/ml concentration, a negative control. Statistically significant difference is denoted by asterisk. Figure taken from [244].....	110
Figure 5.7. Determination of maximal adsorption capacity (Q_{max}) for the hair samples of two types. Hair was incubated in MB solutions of varying initial concentration, $[MB]_{init}$. Q_{max} was assessed as described. NP- and P- designate the non-modified or enzymatically modified hair.....	111
Figure 5.8. Distribution models of the surface topography of adsorption centers for various energies on the solid surface. A. , “Patch-wise” type surface. B. , “Random” type surface. C. , “Intermediate” type surface. Two energetically distinct types of adsorption centers are marked with filled and blank circles. Where possible, the areas of similar energy potentials are marked by cyan filler. The image was adapted from [17].....	111
Figure 5.9. A view from the top of artificially colored 3D visualization of the sites of highest dye affinity (dark-blue) and the bulk hair adsorbent volume (light-gray). A. , non-modified adsorbent. B. , phospho-modified adsorbent. Scale bar, 7 μ m. Figure taken from (manuscript submitted).....	112
Figure 5.10. 3D reconstitution of the sites of highest dye affinity (dark-blue), other binding sites of lesser affinity and the bulk hair adsorbent volume (both in cyan). A. , Bulk hair adsorbent volume shown. B. , Bulk hair adsorbent volume omitted for clarity. Fluorescent artefact is denoted by an arrow. Scale bar, 7 μ m.....	112
Figure 5.11. Regulation of keratin proteins family in live tissues, according to [14]. Proposed functions of hair keratin phosphorylation, emerging from the literature, are shown in red rectangles.....	115

List of tables

Table 2.1. Evaluation of the phosphorylated content by malachite green reaction of different phospho-silk fibroin blends.....	25
Table 2.2. Main thermal peaks identified by DSC for the phospho-silk fibroin films.....	28
Table 2.3. Computed kinetic values for different release profiles of phospho-silk fibroin films.....	30
Table 2.4. Cell counting as function of phospho-content amounts.....	33
Table 3.1. Evaluation of the phosphorylated content (phospho-Ser) by malachite green reaction for different silk fibroin blends. The percentages denote phosphorylation extent of all possible sites.....	50
Table 4.1. Different model equations used in the current work.....	77
Table 4.2. Estimated kinetic parameters of MB dye adsorption on different hair types.....	82
Table 4.3. Parameters of the isotherms, applied on MB dye adsorption curves for different hair types..	83
Table 4.4. Thermodynamic parameters of the MB dye adsorption onto different hair types.....	85
Table 5.1. Various estimated parameters of MB dye adsorption on different hair types.....	113
Table 5.2. Thermodynamic parameters of the MB dye adsorption onto different hair types.....	113

List of equations

Equation 2.1. The calculation of silk phosphorylation degree.....	20
Equation 2.2. The calculation of a swelling ratio.....	21
Equation 2.3. Empirical relationship, given by Ritger–Peppas model.....	22
Equation 2.4. Empirical relationship, given by Higuchi simplified model.....	22
Equation 2.5. Released fraction of piroxicam at discrete time.....	22
Equation 2.6. Linearized empirical relationship, given by Ritger–Peppas model.....	22
Equation 3.1. Rearranged equation for the intrinsic viscosity.....	46
Equation 3.2. Rearranged Stokes–Einstein relationship.....	46
Equation 3.3. The equation of apparent valence.....	46
Equation 4.1. The calculation of adsorption capacity.....	76
Equation 4.2. The calculation of percentage removal efficiency.....	76
Equation 4.3. Pseudo-first order kinetics.....	77
Equation 4.4. Pseudo-second order kinetics.....	77
Equation 4.5. Intra-particle kinetics.....	77
Equation 4.6. Langmuir isothermal model.....	77
Equation 4.7. Freundlich isothermal model.....	77
Equation 4.8. Dubinin–Radushkevich isothermal model.....	77
Equation 4.9. van't Hoff thermodynamics.....	77
Equation 4.10. Gibbs free energy change.....	77
Equation 4.11. The equation of Langmuir model-derived dimensionless separation factor.....	82

Description of the thesis format

This thesis is divided into five chapters, with three of them being a comprehensive experimental research. Three other chapters either overview the theoretical basis of performed research, or conclude additional assumptions derived from it. The contents of each chapter are summarized below.

Introduction Chapter (I)

The first chapter of this thesis is an introduction. Introduction briefly states the properties of fibrous materials, silk and keratin, important in the context of performed research. A necessary description of the natural catalyst, protein kinase A, used during research, follows. The goals of this thesis constitute the last part of Chapter I. Since the major part of the work, presented herein, deals with silk and not keratin, higher attention towards the first material type is given.

Chapters II to IV

The chapters included in this section are based on the series of related manuscripts that resulted from research work, already published or submitted for publication. The chapters are placed chronologically, similarly to the development of an overall work progress. Hence, the first published article constitutes Chapter II, the second — Chapter III and so forth.

Chapter II describes the first attempt to phosphorylate wild-type silk fibroin with a protein kinase. Development of protocols for phosphorylation and phosphate quantification are reported. Phospho-silk-based materials and their biocompatibility are investigated.

Chapter III explores additional important aspects of phosphorylation effect on intra- and inter-molecular interactions within modified silk. Various aspects of encapsulated drug retention and release are described.

Chapter IV describes phosphorylated hair keratin-based adsorption system for a model cationic dye. Pairwise comparison of the modified keratin versus non-modified one is performed. The different obtained kinetic and thermodynamic data and their meaning, along with adsorption modelling approaches are comprehensively discussed.

Chapter V

Chapter V ends the document by summarizing and concluding the research work under the scope of this thesis. This chapter is based on mini-review, submitted for publication.

Introduction Chapter (I)



Image credits: Allison Guy/NEXTNATURE and WINTERCAMPERS

Introduction Chapter (I)

1.1. Fibrous materials: mulberry silk fibroin, a material of choice for the variety of biotechnological applications

For years, silk fibroin (SF) of a domestic silkworm, *B.mori*, has been recognized as a valuable material and extensively used. In the last decades, new application fields are continuously emerging for this material of versatile properties. Those final, specific applications of silk dictate the way it is been processed in industry and research. The detailed description of workflow possibilities from the naturally found, raw material, to a finally formulated product was presented (manuscript submitted).

SF is a natural protein polymer, produced by some of *Lepidoptera* species, such as silkworms and spiders [18]. Depending on its source and biological function, the silk composition, structure and properties may differ significantly [19]. Silks are involved in cocoon formation for protection of eggs and larvae, web formation and support for spiders, and in traps for predation [18]. One of the most characterized silks comes from the silkworm *B.mori* due to its long history of domestication [20], use in textile industry and medicine [19]. Owing to biocompatible and mechanical properties of SF, its use has been increasing dramatically in biotechnology and biomedical areas [18].

Wild type silkworm SF, consists of two different proteins: the structural fibrous protein (fibroin) and sericin, a glue-like protein that covers the fibroin molecules into larger fibre tread [20]. As a polymer, SF consists of $-\text{[Gly-Ala]}_{x2}-\text{Gly-Ser}-$ repetitive motifs that form highly hydrophobic antiparallel β -sheets [21],[22]. Structurally, silk is constituted by three polypeptides: heavy (H, 350kDa), light (L, 25kDa) fibroin chains and P25, a 30kDa glycoprotein, in a molar ratio of 6:6:1, respectively [23]. The L-chain that is linked to the H-chain by a single disulphide bond, possesses 262 residues and a non-repetitive sequence [10]. The H-chain has 5263 residues and is composed primarily of Gly, Ala, Ser, and Tyr [10]. The H-chain possesses a low-complexity repetitive sequence, its majority is formed by repetitions of a $-\text{Gly-X}-$ motif, with X being Ala, Ser, Tyr or Val [10].

Since 1953 a discrepancy regarding precise SF molecular weight (MW) existed, various studies reported significantly different MW values (see [24] for references). Nowadays, the most accepted silk MW value is $\approx 350\text{kDa}$, experimentally reported by Zhou *et al.* [25].

A number of SF structures have been reported (Figures 1.1 and 1.2): the water-soluble state (Silk I), the crystalline silk (Silk II) and an air/water interface orientation (Silk III) [22]. The first two forms are commonly found in nature, with Silk II as a dominating one. Silk III is observed under special conditions, created *ex vivo*. Silk I is ordinarily observed in the silkworm glands [26], it contains random-coil and amorphous regions [27]. Silk I is unstable to mechanical deformation [20], thus upon heat exposure or physical spinning converts to antiparallel β -sheet, *i.e.* Silk II [22]. For the β -conformation, Takahashi *et al.* proposed the antiparallel sheets, established by hydrogen bonds between the opposite Gly and Ala side chains [20, 22, 28]. This crystalline conformation leads to a thermodynamically stable structure, preventing spontaneous separation of molecules [20] and water-based dissolution, including solvents of mild acid and alkaline composition, and some chaotropes [22].

Finally, the crystal Silk III structure involves a hexagonal arrangement of silk molecules in a threefold helical chain conformation. This structure causes the separation of Ser and Ala residues, allowing fibroin to act as a surfactant at the air-water interface [29].

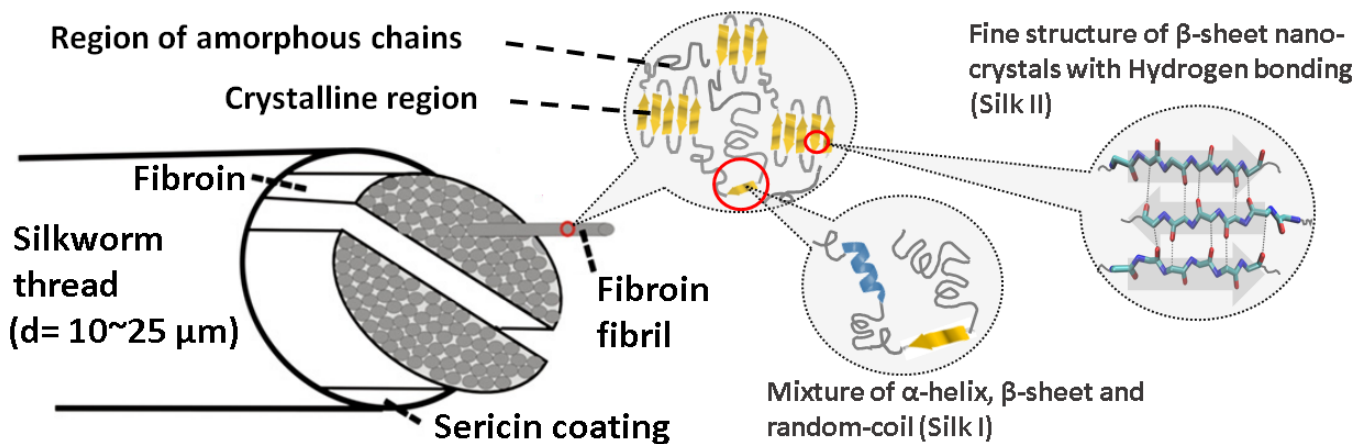


Figure 1.1. Schematic representation of the deduced SF structure. Insets show the fibril overall structure and the fine β -sheet antiparallel alignment of SF polypeptide chains. The image was adapted from [1].

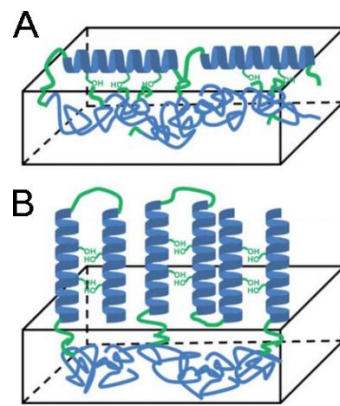


Figure 1.2. A model, suggesting possible structures of the adsorbed Silk III layers at the air–water interface, obtained at low (**A**) or high (**B**) bulk concentration of silk solution. Figure taken from [2].

As a starting point in silk processing, the stifled cocoons need to be de-gummed. The degumming process is a sericin coating removal, so that raw silk fibre mass is obtained. Several ways of degumming have been reviewed before [1, 30], of which boiling in 0.02 M sodium carbonate, Na_2CO_3 , is commonly used [31]. Sericin removal pursues two goals: it abolishes biocompatibility issues of later silk applications [32, 33] and exposes the fibrous molecules for further processing options. SF protein *per se* is considered non-immunogenic [34] and is approved by the American Food and Drug Administration (FDA) as a source for biomaterials production [27]. Nevertheless, degumming affects the fibrous protein by altering its mechanical properties like elasticity and tensile strength [35] *via* modified molecular structure [36].

Sericin-free silk is preferably dissolved prior to its usage. To dissolve SF, in our work a concentrated lithium bromide, LiBr-based aqueous system was employed [31]. The dissolution step was followed by a dialysis in water for salt removal; the prepared material is known as regenerated silk fibroin (RSF).

In most cases the researches wish to customise a final product, rendering (bio-) chemistry indispensable. Hence, with the RSF being at stock, its biochemical alteration in the liquid phase was made before subsequent formulation. In the last decades numerous attempts were made to substitute the “conventional”, purely chemical methods, by a more environment-friendly, so-called “green chemistry” techniques. In that extent, enzymatically-driven reactions attract significant attention, not only for being relatively non-hazardous or harsh treatments, but also due to their high specificity towards the substrates. We now shall briefly focus on some of the reported examples of enzymatic treatments for SF.

Enzymatic treatments of SF commonly pursue two goals: its (selective) degradation [37, 38] or the conjugation with other polymers [39-42]. A comprehensive analysis on SF degradation rates and degradation-related products was presented previously [3] (Figure 1.3).

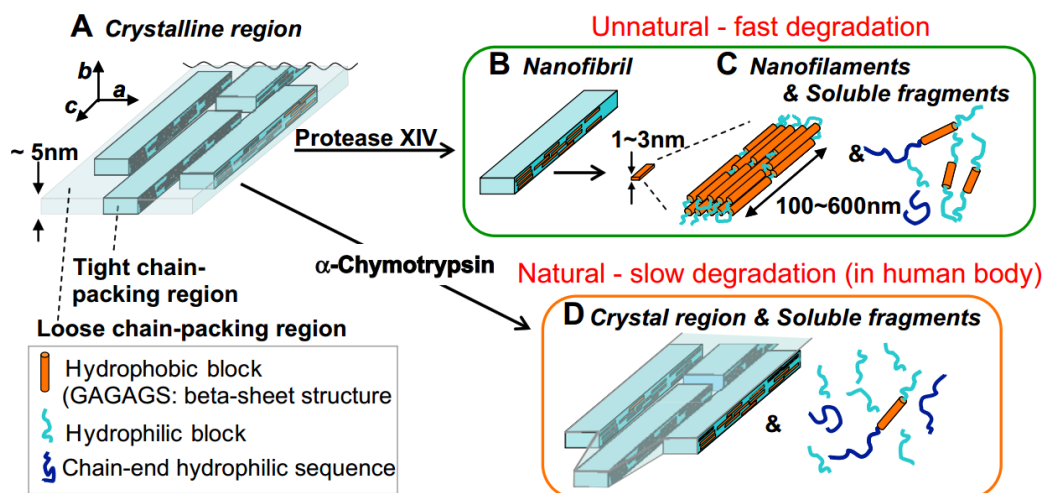


Figure 1.3. Model of enzymatic degradation of SF crystalline regions. Figure taken from [3].

Additional approaches to functionalize silk are comprised of strategies aiming the preparation of fibrous polymeric structures, enzymatically-driven mineralization of silk scaffolds and *in vitro* phosphorylation of SF. For instance, a series of data regarding poly(acrylonitrile-*co*-SF peptide) syntheses was previously divulged. The common strategy was to co-polymerise acrylonitrile (AN) with a vinyl-decorated SF peptides. The peptides were acquired by enzymatic digestion of SF powder by α -chemotrypsin and subsequently reacted with acryloyl chloride in appropriate solution. To obtain the various final products, polymerisation with AN was carried out [43-45].

Alkaline phosphatase (ALP)-assisted *in situ* mineralization of pre-fabricated SF-based porous scaffolds was reported. Electrostatic attractions between ALP and SF scaffolds anchor the enzyme. Later, provided with mineralization medium, deposition of mineral calcium phosphate was observed [4] (Figure 1.4).

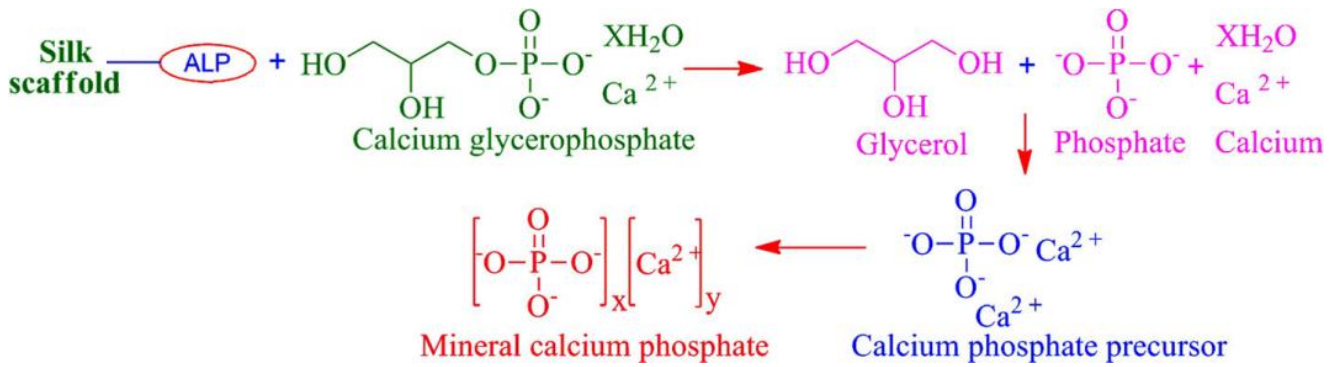


Figure 1.4. Proposed reaction mechanism of ALP with calcium phosphate. Figure taken from [4].

Lastly, *in vitro* enzymatic phosphorylation of specific amino acid, Ser, within a chimeric silk polypeptide was reported [5]. Winkler and co-workers successfully phosphorylated genetically engineered spider silk with protein kinase A (PKA), presenting the possibility to enzymatically modify fibrous materials in a particular way (Figure 1.5). They concluded that silk phosphorylation caused a decrease in the β -structure content of the protein, but was not able to completely inhibit the β -sheet assembly. Additionally, overall solubility of the modified protein increased ≈ 4 -fold compared to the non-modified form. Enzymatic phosphorylation systems can therefore provide opportunities to disrupt the β -sheet assembly processes in cases of need. Thus, if a silk as biomaterial of choice is used and treated by the “green” method, its properties can be tuned and the issues of biocompatibility can be avoided or considerably alleviated.

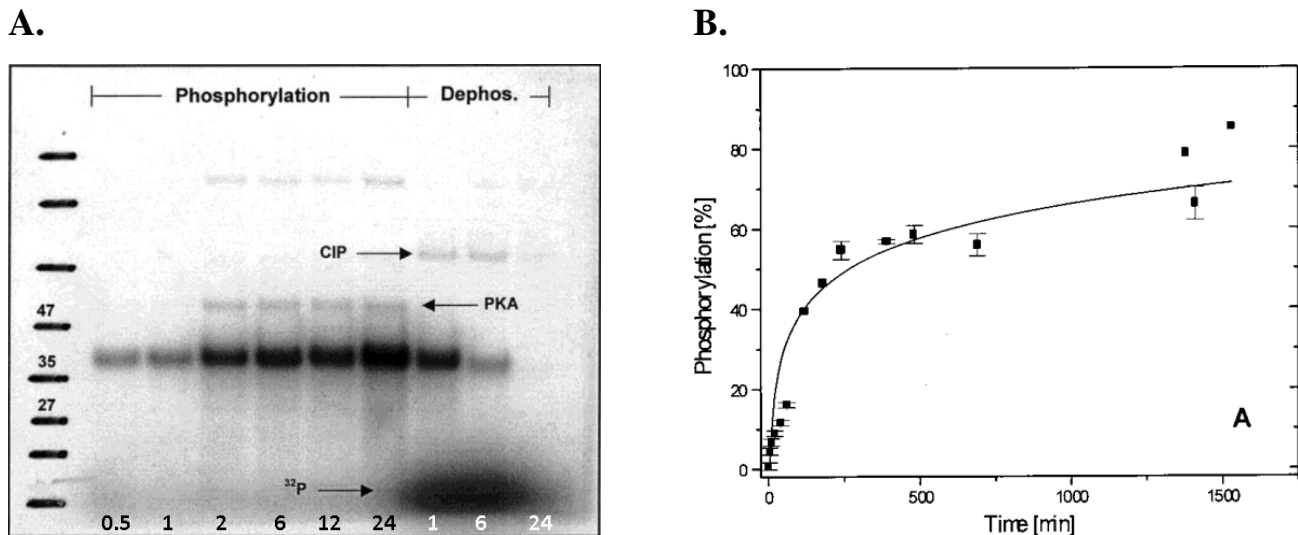


Figure 1.5. Evidence to enzymatic phosphorylation of silk. **A.**, autoradiography of reaction. Sample phosphorylation and de-phosphorylation after the indicated hours (in black and white, respectively). **B.**, ^{32}P transfer to the recombinant silk protein, determined by liquid scintillation. Figure taken from [5].

1.2. Fibrous materials: hair keratin and its several trends of usage in the context of present research

Another fibrous material of natural origin commonly utilized in industry and research is keratin. Beyond its well-known and long history of usage in various textile- and cosmetics- related industries ([46] and references within, [47]), in the last decades new attractive applications in the fields of multifunctional materials through protein engineering emerge. This innovative trend for keratin generally follows the above described methodology development for SF. We now shall briefly revise some of the keratin properties and its latest applications in several fields, including the “green chemistry” context.

Keratins constitute a family of proteins with diverse morphologies and properties, being the major components of hair, feathers, nails and horns of animals and birds [48]. All keratin fibres share a common molecular structure, comprising two layers: an inner cortex and an outer cuticle. The cortex is responsible for the mechanical strength and rigidity of the fibre [49], while the cuticle plays important role in its durability, felting and shrinking. Structurally, keratin associated (KAPs) and keratin intermediate filament (IFPs) proteins are the most notable fibre constituents, contributing $\approx 90\%$ of the its substance by weight [50]. Chemically, type I (acidic) and type II (basic) keratin classes constitute two main kinds of this fibrous material. Hard keratins (5% sulphur) are found in hair, horns, feathers, etc. [51], whereas soft epidermal keratins (1% sulphur) present in the *stratum corneum* of skin [52]. Hard and soft keratins have different amino acid compositions, but they share the similar peptide structures in the coiled conformations [53]. Numerous groups of KAPs and IFPs from Merino wool were identified and described [54]. As for the human hair keratins, they are hard, consisting of 65-96% proteins [55], with MW in the range of 44–66 kDa [56]. Most structural and compositional aspects of both human and animal keratin are similar [57]. Human hair fibres contain three distinct parts: the cuticle, cortex, and medulla, although the medulla may not be present. On the contrary, in animals the medulla is usually absent [58]. The structural generalized model of the hair is depicted in Figure 1.6. Additional aspects regarding keratin biology, chemistry and structure are discussed elsewhere [59-61].

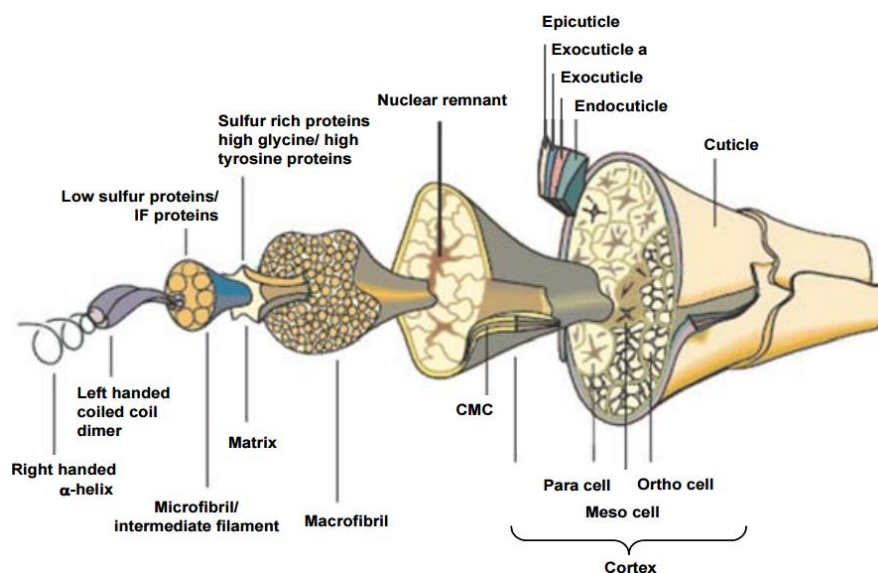


Figure 1.6. Accepted model of common wool (and human hair) keratin structure, as appearing in [6].

The intrinsic biocompatibility, biodegradability, mechanical durability and natural abundance of keratins made them a target of extensive studies as potential (bio-) materials for a variety of applications, especially in the biomedical field (see [62] and references within, [63]). Industrial utilizations of keratin and related materials as exhausting agents in textile dyeing process [64] or promising adsorbents for toxic effluents [65], among others, were reported. To accommodate for different final applications, keratin may be modified and formulated in many ways, similarly to SF. The majority of chemically available modifications are reviewed elsewhere [66]. Some recently reported methods include, but are not limited to, enhanced extraction protocols of keratins [67, 68], thiol-ene click chemistry approaches [7, 69] (Figure 1.7), modifications with iodoacetic acid [70], keratin photo-crosslinking [71], and others.

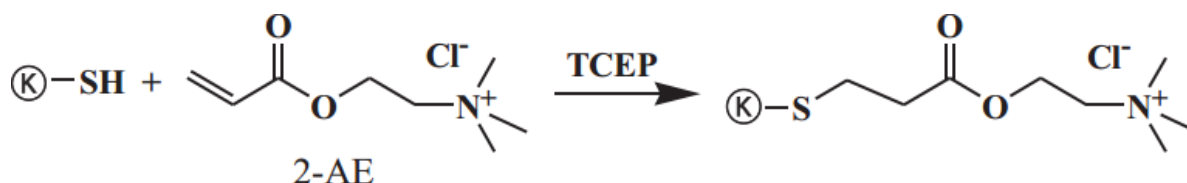


Figure 1.7. The reaction of [2-(acryloyloxy)ethyl] trimethylammonium chloride (2-AE) with a cysteine thiol (Ⓚ-SH). Figure taken from [7].

In this context, enzyme-mediated techniques of keratin processing are but a small portion of all the possibilities present nowadays. The obsolete majority of enzymatic treatments of keratin is its degradation, which can serve various goals, such as keratinous wastes recycling, being auxiliary factor in medical applications, drain pipe and tank cleaning, and some others (reviewed in [72]). Different

keratinolytic proteases (keratinases) were also obtained from bacterial (*B.licheniformis*) and fungal (*A.niger* and *P.lilacinum*) species [73-75]. For those material-degrading enzymes, potential applications in the field of detergent formulations, leather and textile industries are proposed. Transglutaminase (TGase; protein-glutamine-glutamyltransferase) –treated and subsequently cast keratinous solutions were examined for their mechanical and structural properties [8]. The cross-linking reaction of TGase (Figure 1.8) led to an improvement of the mechanical properties and stability under aqueous conditions of a keratin-derived film, whose surface became rougher and tighter network structure was formed. Instead of traditional chemical anti-felting pre-treatment of wool, the fabrics can be treated with low temperature air plasma, followed by the combination of TGase and Savinase 16L protease [76]. This recently reported approach allows to control the tensile strength and improve shrinkage resistance of the wool fibre. Another ways of modification of keratin fibres can be found in patents, dealing with wool in textile industry [77], or in

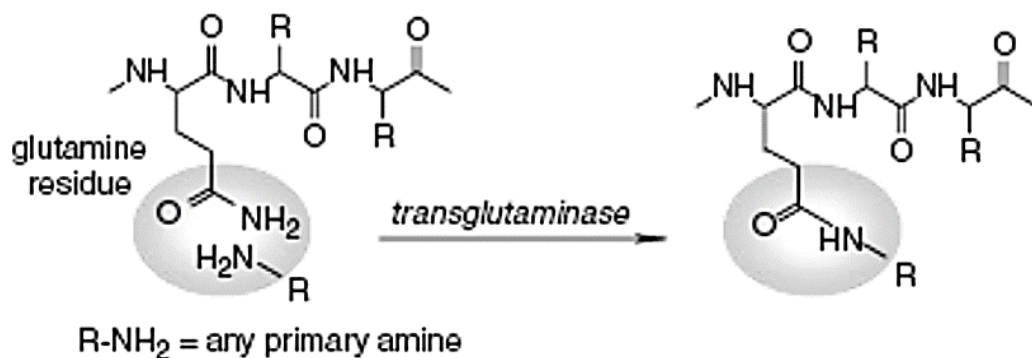


Figure 1.8. The cross-linking reaction mechanism catalyzed by TGase, as proposed by [8].

cosmetic applications [78-80]. The usage of protein disulphide isomerase (PDI) for incorporation of functional molecules onto keratinous substrates was previously reported by our group [81, 82].

Yet another enzyme-related data on keratin-based materials can be found. However in the next two cases HRP and lysozyme were immobilized on wool, either preliminary activated with cyanuric chloride [83], or through crosslinking reactions, involving *N*-Succinimidyl 3-(2-pyridyldithio) propionate (SPDP) and sulfosuccinimidyl-4-(*N*-maleimidomethyl)cyclohexane-1-carboxylate (S-SMCC) [9]. The latter method is shown on Figure 1.9. Moreover, α -amylase was covalently immobilized on cyanuric chloride-activated wool [84]. In all of the above cases the enzymes were attached to keratinous substrates with

good preservation of their properties, *i.e.* their stability was increased. However, these are not methods of enzymatic treatments of wool.

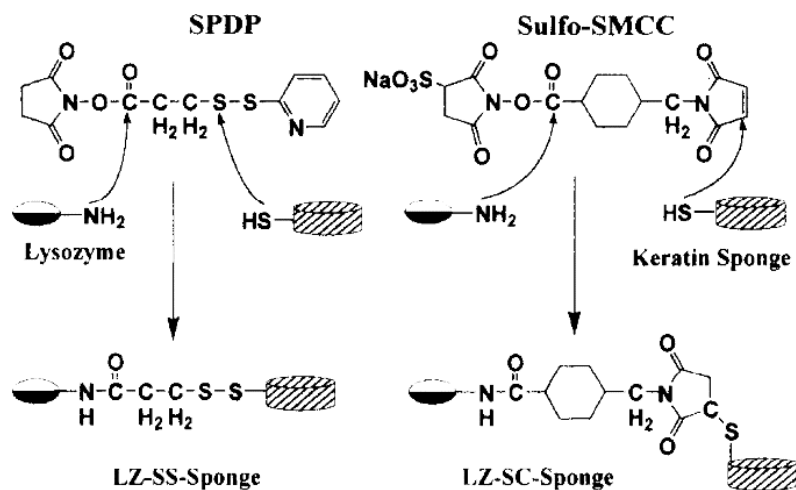


Figure 1.9. Preparation of lysozyme-keratin sponge conjugate, after [9].

Finally, the phosphorylation of keratinous fibers *in vivo* and *in vitro* was reported. *In vivo* phosphorylation of different keratinous filaments is known for years, and it is accepted that this phosphorylation has one of the paramount roles in routine functioning of the living systems [85, 86]. Currently, solely one study encompassing *in vitro* phosphorylation of extracted keratin, was encountered [87].

1.3. Protein kinase A: a natural catalyst of phosphorylation

In this context, several words must be said about PKA that was the catalyst of our choice. PKA, a cyclic AMP-dependent protein kinase, transfers the γ -phosphate of ATP to serine and threonine residues [88] of many cellular proteins. It is, by far, the best understood protein kinase from a mechanistic point. PKA is a hetero-tetramer, composed of a regulatory dimer (R₂) and two catalytic subunits (2C). The C-subunits are activated upon cAMP binding of R₂ and the following dissociation of the tetramer [89]. The C-subunit of PKA is comprised of two domains. These are a small ATP binding domain, composed primarily of α -helices, and a larger substrate binding domain, generally built of β -strands (Figure 1.10). The essential phosphorylation site in PKA, Thr-197, is part of an activation loop segment. Phospho-Thr-197 enhances catalytic activity by ≈ 3 orders of magnitude in PKA and is a substantial PTM [90]. In addition, the two domains are connected by a linker region, thus generating an ATP and substrate

binding pocket. ATP is located deeply between the domains and the inhibitor peptide resides on the periphery of the pocket. The recognition or consensus sequence of the substrate that may undergo PKA-mediated phosphorylation, was previously divulgated [91]. In the course of enzymatic reaction, phosphoryl transfer is fast and ADP release is considered to be the rate-determining step [92]. PKA has an intrinsic ATPase activity, utilizing water as phosphorylation target, if no other proteinaceous substrate is available [92]. While substrate phosphorylation by this kinase is pH dependent, it has been demonstrated that the rate of γ -phosphate group transfer is invariant over a wide pH range of 6-9 [93]. The latter datum is very important, since it enables the researcher to perform an enzymatic reaction in physiological conditions, in terms of pH and, also, temperature. Our working PKA buffer has a pH value of ≈ 7.3 . Bearing in mind the characteristics of PKA best performance, we were able to successfully utilize this enzyme in our work, as will be shown throughout this document.

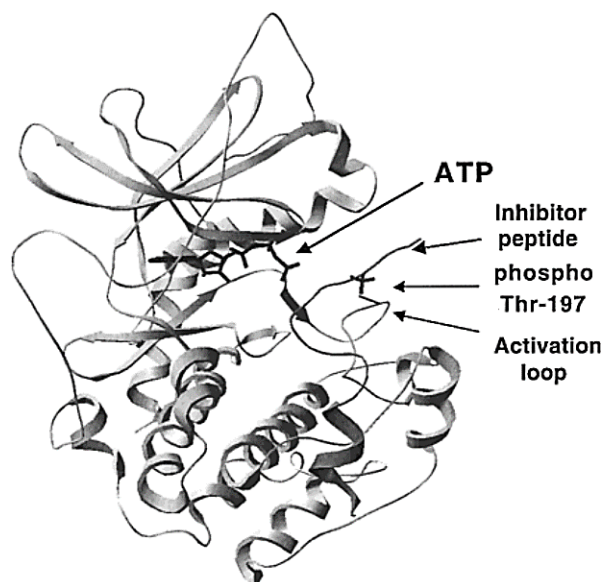


Figure 1.10. Ribbon diagram of PKA co-crystallized with ATP and a peptide inhibitor, as appearing in [15]. Arrows point to the activation loop and the phosphorylation site, p-Thr-197, in the activation loop.

1.4. Principal goals of the work

Since phosphorylation of both SF and keratin occurs in nature, it was of our interest, whether we can reconstitute the aforementioned reaction. As stated previously, the usage of enzymes, accompanied by other “green” methods is been lately seen as an attractive alternative to “canonical” chemistry,

especially where high-specificity, *in situ* modifications of substrates of interest are required [94].

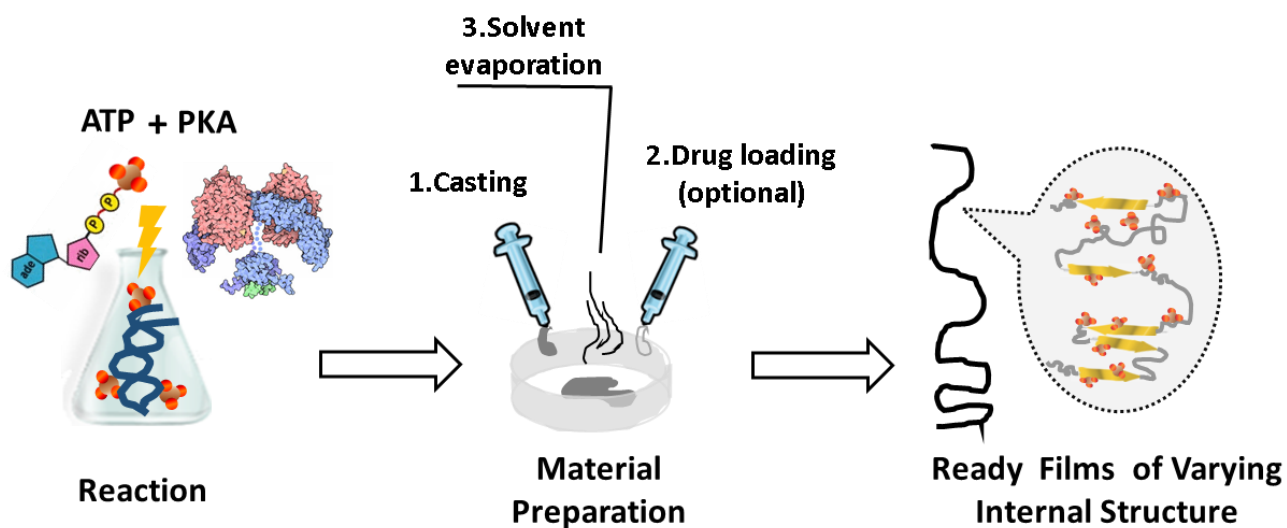
Therefore, the current research aimed five specific goals:

1. Attempt to reconstitute *in vitro* enzymatically-driven phosphorylation reaction for SF. Due to the structural specificities of raw silk packing, it can't be phosphorylated directly. Initially, silk has to be stripped from its sericin outer coating. Subsequently, it is extracted into aqueous media and later mixed with appropriate buffer. At this stage, fibroin is modified *in vitro* by protein kinase A, using exogenous ATP as a source of incoming phosphate γ -group (Chapter III). Success of phosphorylation opens a new path towards diversification of SF that can potentially be used in a pre-formulation step;
2. Once the phosphorylation reaction is proven and optimized, batch production of phospho-silk-derived materials and their subsequent characterization can initiate. As a first trial, the simplest formulation is attempted — SF-based films. The films are obtained by solution casting, followed by solvent evaporation. At the liquid stage, it is possible to add any other compound of interest, to the phosphorylated silk solution. The compound (typically a drug or any molecule of biological action, if the films are intended to be used as biomaterial) will be incorporated in the solid structure of a formed films upon solvent evaporation. I was using Piroxicam (Chapter III), a relatively hydrophobic drug, as a model for incorporated compound. Regardless of Piroxicam addition, the produced films are needed to be assessed for chemical and structural changes, (if any present), as a result of phosphorylation;
3. Additional important structural and chemical aspects of the phospho-silk are to be elucidated in the altered environment (Chapter IV). For that, pH of the modified silk solution is adjusted, solution cast and let the solvent evaporate. From the previous study [16] it is known that aqueous solutions of SF are highly sensitive to pH. Thus, adjusting pH poses an interesting opportunity of modulating the degree of silk self-folding during solvent evaporation. Moreover, influence of phosphorylation on protein net charge at varying pH values was studied by direct charge measurements. Similarly to the preceding paragraph, the retention and release behavior of incorporated drug, Methotrexate, was inspected;

4. Somewhat apart from the aforementioned work stands the reconstitution of *in vitro* phosphorylation of keratin fibers. The unusual obstacle in this case posed the fact that a trial is made to modify the *solid* fiber (Chapter V). Attempts to phosphorylate the extracted (*i.e.*, delipided and solubilized) keratin, although successful, are not in the scope of the current research. Therefore, I tried to modify the solid, yet delipided hair keratin. Instead of delipidation protocol *per se*, the chemical bleaching of human hair was performed, aiming to get rid of the pigments and of lipid layer (with the outer parts of cuticle). Since considerable amount of cosmetic applications are formulated for the bleached hair, it was of interest to reconstitute the bleached and phosphorylated system during the course of my work. Again, successful phosphorylation of the solid hair shafts opens a novel opportunity in keratin-based materials engineering;
5. Once the phosphorylation reaction is proven, it is possible to elucidate the outcomes of phosphorylation on keratin (Chapter V). A model dye, Methylene Blue (MB) is used to assess the degree of affinity of cationic species to the modified keratin. As incoming phosphate groups are known to increase negative charges on the modified surfaces, the adsorption of MB is expected to increase accordingly. Various kinetic and thermodynamic studies are undertaken in order to clarify additional aspects of behavior of the obtained, keratin-based system;

With the enumerated goals in mind, the present work generally aimed to phosphorylate naturally found fibrous materials throughout a “natural” catalyst way. The idea was to demonstrate the very possibility of such phosphorylation, as well as to elucidate its effects on the modified materials. Pairwise comparison between modified and non-modified SF- and keratin- based materials made it possible to precisely conclude the impact of phosphorylation on the chosen fibrous materials.

Chapter II



Chapter II

Enzymatic phosphorylation of silk fibroins: a platform for the production of tunable materials

Abstract

Regenerated silk fibroin was modified by *in vitro* enzymatic phosphorylation for the first time and casted into films. Phosphorylation was achieved for up to 60% of all possible sites of the silk fibroin chain. Films were produced by blending at several ratios the phosphorylated and un-phosphorylated fibroin solutions and assessed for qualitative changes. DSC measurements have shown that phosphorylation altered the intra- and inter-molecular interactions. Further experiments demonstrated that phosphorylation can be used to tailor the hydrophylicity/hydrophobicity ratio and crystallinity of silk fibroin films. Encapsulation and release profile of a model drug, piroxicam, was highly dependent on silk fibroin modification level. Cytotoxicity assays showed that exposure to lixivates of phosphorylated of silk fibroin films only slightly affected cellular metabolism and proliferation, although direct contact denoted a strong correlation between phosphorylation level and cell proliferation. This study reports a novel methodology for tuning silk fibroin biomaterials to obtain specific structural and biochemical features, which can be adapted for a wide range of applications. Thus, phosphorylation may be practically applied to improve, in terms of cytocompatibility, any silk-based device that is considered to be in contact with live animal or human tissues.

This chapter is based on the following publication: **Vadim Volkov**, Andreia Vasconcelos, Marisa P. Sárria, Andreia C. Gomes, Artur Cavaco-Paulo; Enzymatic phosphorylation of silk fibroins: a platform for the production of tunable materials, *Biotechnol. J.*, 2014 Oct; 9(10):1267-78

2.1. Introduction

Silks are naturally occurring protein polymers produced by a wide variety of insects and spiders [95]. Silk fibroin from silkworm *Bombyx mori* consists of two proteins: light (25 kDa) and heavy (391 kDa) chains, presenting in an equal ratio and linked by a disulphide bond [96]. The amino acid composition of a heavy chain is primarily presented by glycine, alanine, and serine in the molar ratio of 3:2:1 which form typical $-(\text{Ala-Gly})_n-$ hydrophobic motifs known as β -sheet crystalline domains [10]. Based on silk fibroin biocompatibility, biodegradability and mechanical strength, different silk-derived materials were developed for biomedicine [22, 97].

Several properties of silk, such as mechanical characteristics, solubility and biodegradability, can be controlled by manipulating its structure. Silk proteins have been genetically engineered in a variety of host systems [98]. Furthermore, multi-component blended systems of silk fibroin with various substances have been produced [99, 100]. Silk-based materials may be selectively degraded to modulate their porosity and their surface may be altered by coupling peptides or other molecules of biological significance [101-103]. Amino acid residues in silk such as Tyr and Ser can be modified enzymatically [40, 104] which can be exploited for functionalizing silk-based materials.

Phosphorylation is one of the most important post-translational modification of proteins and incorporation of a single phosphate group can establish many strong hydrogen bonds that affect intra- and inter-molecular interactions [105]. Protein phosphorylation is stable under physiological conditions, thus suitable for directing the formation and reorganization of dynamic protein interaction networks [106]. However, using phosphorylation for silk fibroin protein functionalization studies is largely unexplored. Only one report on silk fibroin phosphorylation *in vitro* has been published so far [5]. The authors describe the phosphorylation of recombinant spider dragline silk fibroin variant with the engineered kinase recognition sequence in order to increase silk fibroin solubility [5]. In turn, we were interested in modifying by phosphorylation *B.mori* reconstituted silk fibroin heavy-chain proteins. To the best of our knowledge, this is the first study attempting such a modification of regenerated silk fibroin. The enzyme protein kinase A can be used to achieve phosphorylation of silk protein, with Ser as the only possible phosphate acceptor [15, 88].

Biocompatibility is a pivotal aspect in developing new materials for application to living systems. One of its most important aspects is cytotoxicity, often measured in terms of cell viability or proliferation. Significant research has been devoted to fabrication of bio-inspired materials with different cell -differentiating and -sustaining features [107-109]. If the materials are not cytotoxic, they may or may not promote cell proliferation and, inversely, cell differentiation. By lowering the probability of cell attachment to the surface of the material, cell proliferation is not favored. One of the possible approaches is to create a negatively charged bio-material surface, owing to the electrostatic repulsion between partially negative charge of cell outer membrane and the bio-material.[110]

The goal of this study was to demonstrate a straightforward methodology to produce biocompatible silk-based materials with tunable characteristics. Phosphorylated silk fibroin solutions were made to produce cast films of variable phosphorylated Ser (phospho-Ser) content. The obtained materials were submitted to several tests that confirmed a dependency between the amount of phospho-Ser and their bio-chemical properties, including loading of a model pharmacological compound with anti-inflammatory activity.

2.2. Materials and methods

2.2.1. Materials

Silk cocoons from *B.mori* were donated from “Sezione Specializzata per la Bachicoltura” (Padova, Italy). The L929 cell line was used. Kinase-GLO[®] luminescent kinase assay kit (Cat.no. V6712) and CellTiter 96[®] Aqueous One Solution (Cat.no. G358B) were obtained from Promega Corporation, USA. Petri dishes (Cat.no. 391-2072) were from VWR International, tissue culture test plates of various well amounts (12, 24, 96) were from TPP Techno Plastic Products AG, Switzerland, and Whatman grade 2 filter paper (Cat.no. 1002-070) was from Whatman, USA. Glass culture cylinders (Cat.no. 070303-10) were supplied by Chromaphor Analysen-Technik GmbH, Germany. All the other reagents were purchased from Sigma-Aldrich, Spain.

2.2.2. Preparation of silk fibroin solution

Silk was degummed from the sericin content as described elsewhere [111]. Briefly, silk was boiled for 40 min in an aqueous solution of 0.02 M Na₂CO₃ and subsequently rinsed with water. Silk fibroin was dried for 2 to 3 days at room temperature. Silk solution of 2 wt% was prepared by dissolving the degummed fibroin in 9.6 M LiBr solution at 60 °C for 3 hours. The resulting solution was filtered and dialyzed against double distilled water until salts' completely removal, using cellulose tubing of molecular-weight cut-off of 12–14 KDa. The concentration of silk fibroin was assessed on Whatman paper via dry weight method, in triplicate.

2.2.3. Preparation of phospho-silk fibroin films

Dialyzed raw silk fibroin solution was enzymatically phosphorylated using protein kinase A (EC 2.7.1.37) at the concentration of 1 protein kinase A Unit for 95 µL reaction total volume in appropriate buffer (50 mM TRIS-HCl, 10 mM MgCl₂, pH 7.5 [5]). 0.5 mM Adenosine-5'-triphosphate (ATP) was a source of phosphate. 3 µM Na₃VO₄, a phosphatase inhibitor and 55 µM 3',5'-cyclic-AMP were added to the reaction mixture, followed by an incubation at 20 °C with stirring at 30-40 rpm for 5 to 6 hours [15, 88]. The reaction progress was qualitatively assessed hourly using Kinase-GLO[®] kit. After the reaction the desired blends, containing various amounts of phospho-silk fibroin content were prepared by casting and mixing the appropriate quantities of raw silk fibroin and phospho-silk fibroin solutions in Petri dishes. The casted solutions of 5 mL volume were left for drying under constant air flow in laminar flow hood for 2 to 3 days at room temperature.

2.2.4. Quantitate determination of phosphate incorporated in phospho-silk fibroin

An aliquot of reaction mixture was initially precipitated with cold ethanol (1:9 volume ratio), centrifuged at 5000 RPM, re-suspended in double distilled water with vortexing and incubated in warm bath (35°C) with 2.5 mM NaOH [112] for 15 min. A 40 min centrifugation at 9000 RPM followed, and supernatant was carefully taken. A mixture of 22 volumes of supernatant to 1 volume of 70% w/v HClO₄ was centrifuged anew at 9000 rpm for 30 min [113]. The final supernatant is diluted with double

distilled water and used for malachite green reaction ((malachite green reagent):(sample) volume ratio 1:6 [114, 115]). The reaction mixture was incubated at 20 °C for 30 min and optical absorbance read at 630 nm against a standard curve.

Knowing the amount of phosphorylation sites present in fibroin chain (section 2.3) and the fact that each discrete site may be modified only once, the phosphorylation degree was calculated. The calculation is formulated as following:

$$\frac{\text{Pi amount released}}{\text{Maximum possible Pi amount to be released}} \times 100 \quad (2.1)$$

Where **Pi** is the concentration of inorganic phosphate, originating from phospho-sites.

2.2.5. Prediction of phospho-sites in silk fibroin

To obtain initial pool of possible sites, three programs: GPS (as stand-alone software v2.1 [11]), KinasePhos [116] and PPSP [117] (both available online) were used on fibroin sequence (DDBJ/EMBL/GenBank accession no [AF226688](#)). High sensitivity was used in all programs, followed by filtering out false-positive predictions. For GPS, threshold was reset to “all” and the results of cut-off ≥ 0.9 were taken; for KinasePhos an HMM bit was set to 8.8 and all non-repetitive results taken; for PPSP “high sensitivity” of performance was used, only the results with risk-differential > 1.43 taken. Exact site positions, observed in any two of the tree resulting groups, were considered as phosphorylation-probable, what resulted in 16 sites. Those sites, as well as the entire sequence, were inspected for characteristic motif -Arg(Lys/Thr)-Arg(Lys/Ser/Thr)-X-**Ser**-X(Leu)-X(Ser)- [91]. Seven of computationally predicted sites were discarded, and 11 newly found sites were assigned.

2.2.6. Fourier transform infra-red (FTIR) spectroscopy

FTIR spectra of different Silk fibroin films were measured with a JASCO FT/IR-4100 type A spectrometer in the spectral region of 4000–600 cm^{-1} with a ZnSe cell in Attenuated total reflectance (ATR) mode and 8 cm^{-1} resolution. The analysis was performed in 64-pass rescan mode, on two different film areas.

2.2.7. Secondary structure analysis

FTIR-derived convoluted curves, corresponding to Amide I spectral interval of [1600; 1700] cm^{-1} , were processed in “Feat Peaks (Pro)” routine of “Peak Analyzer” in OriginPro, v.8.5.0 (OriginLab Corporation, USA). For each compound curve, the baseline subtraction was followed by a multiple pass fit. Discrete initial peak values used for fitting were identified by a Second Derivative in-built method. The secondary conformational data, resulting from individual peaks, were obtained basing on the reported peak assignments [118].

2.2.8. Thermal analysis

Differential scanning calorimetry (DSC) measurements were performed, of two distinct samples, with a DSC-30 instrument (MettlerToledo), from room temperature to 120 °C, at a heating rate of 10 °C min^{-1} , and kept at 120 °C for 10 min, to induce sample dehydration. The temperature was lowered to 25 °C and increased to 350 °C at a heating rate of 10 °C min^{-1} . Mean sample weight was 1.8 ± 0.17 mg. During the analysis the aluminum cell was swept with 80 mL min^{-1} N_2 flow.

2.2.9. Swelling ratio

Phospho-silk fibroin materials, treated with MeOH and completely dry (30 °C for 24 h) were immersed in phosphate-buffered saline (PBS 0.1 M; pH 3, 7.4 and 11) at 37 °C for 24 h. The excess buffer was removed and the wet weight of the films was determined. The swelling ratio was calculated as follows:

$$\frac{W_s - W_d}{W_d} \quad (2.2)$$

Where W_s is the mass of the swollen material and W_d is the initial dry mass. This analysis was performed on two different samples.

2.2.10. *In vitro* release

The release profile of piroxicam, at final concentration of 1.8 mM in phospho-silk fibroin materials, was studied. Piroxicam was initially dissolved in dimethyl sulfoxide and an equal volume of double distilled

water. Control phospho-silk fibroin samples were casted devoid of piroxicam and all the materials were treated with MeOH. MeOH solution was collected from each sample and the released piroxicam due to alcohol application was quantified. Phospho-silk fibroin films were incubated at room temperature under constant shaking (50-60 rpm) in PBS (0.1 M, pH 7.4) or in a solution containing protease, subtilisin from *Bacillus* sp. (EC 3.4.21.62) at 0.075 U mL⁻¹ [119]. At determined time points, piroxicam release was quantified by absorbance measurements at 353 nm against a standard absorbance curves. No buffer exchange was performed throughout the entire assay. All the release experiments were carried out in duplicates for 5 days.

The release behavior was determined by fitting the release data to the empirical relationships given by Ritger–Peppas (2.3) and Higuchi simplified (2.4) equations [13, 120].

$$\frac{M_t}{M_\infty} = kt^n \quad (2.3)$$

$$f_t = K_H \sqrt{t} \quad (2.4)$$

Where $\frac{M_t}{M_\infty}$ is a released piroxicam fraction, calculated as a ratio:

$$\frac{\text{released at discrete incubation time } t}{\text{what is left to be released after MeOH treatment}} \quad (2.5);$$

k is a constant incorporating structural and geometric characteristics of the drug dosage form; **n** is the release exponent and obtained by a linear fitting of log(fraction) versus log t from the modified equation (2.3):

$$\log(\text{fraction}) = \log k + n * \log t \quad (2.6)$$

f_t is the amount of drug released at discrete incubation time and **K_H** is the Higuchi dissolution constant. According to the model, **K_H** is obtained from a linear fit of **f_t** as a function of square root of time **t**, where **K_H** is a slope.

2.2.11. Cell culture handling

The L929 fibroblast-like mouse cell line (ATCC® CCL1™), was maintained in Dulbecco's Modified Eagle medium with L-glutamine and high glucose and supplemented with 10 vol% heat inactivated fetal

bovine serum and 1 vol% antibiotic/antimycotic (10.000 units mL⁻¹ penicillin, 10.000 µg mL⁻¹ streptomycin, 25 µg mL⁻¹ amphotericin) solution. The cells were maintained, in exponential growth, at 37 °C in a humidified atmosphere of 5% CO₂. Cell viability was monitored by Trypan Blue dye exclusion. For experiments, cells were seeded at a concentration of 5,5 x 10⁴ cells mL⁻¹.

2.2.12. Cell proliferation assays

MTS (3-(4,5-dimethylthiazol-2-yl)-5-(3-carboxymethoxyphenyl)-2-(4-sulfophenyl)-2H-tetrazolium) compound, in the presence of phenazine ethosulfate, is bio-reduced by cells into a formazan product with an absorbance maximum at 490 nm, thus assaying active cell metabolism [121]. Sulforhodamine B is a negatively charged pink aminoxanthine dye of absorbance maximum at 540 nm, adsorbed by basic amino acids in the cells, thus proportional to cell number and translating cell proliferation [122]. Triplicate replicates for each individual assay were done.

2.2.12.1. Test by indirect contact

Phospho-silk fibroin films were disinfected by triple washings with antibiotic/antimycotic solution, placed into 12-well culture plate (each film in a separate well) and culture medium (without fetal bovine serum) was added. After an incubation of 1 or 3.5 days at 37 °C, the medium was harvested and supplemented with fetal bovine serum. Additionally, 0.6 g L⁻¹ of L-Glu was added to 3.5-days conditioning batch by the end of conditioning period. The conditioned medium was then applied to adhered L929 cells, replacing the regular medium. The cells were then incubated for 48 and 72 hours and the proliferation was assessed by MTS or sulforhodamine B techniques.

2.2.12.2. Test by direct contact

After disinfection, 10 mm circles were excised from each hydrated film type using a borer and placed in 24-well culture plate, ensuring a flat contact area between the surfaces. Glass culture cylinders were placed on top of the film and 250 µL cell suspension solution was applied to the inner area of each cylinder. After 24 hours of contact the cells were stained with 1 µg mL⁻¹ Hoechst 33258 for 15 minutes.

Cellular adhesion was visualized by epifluorescent bright field microscopy (Olympus IX71 controlled by Cell[^]F Olympus Imaging Solutions software v3.4, GmbH). The quantity of cells was assessed using “Analyze Particles” routine in ImageJ v1.42h using the fluorescence emitted from Hoechst 33258-stained nuclei. Three different regions were examined of each film type.

2.2.13. Statistical analysis

In order to detect differences between phosphorylation treatments in the swelling ratio, a *t*-test was conducted with the observed values. A piecewise regression was conducted in order to detect the breaking point of the swelling ratio curve. Percentage of phospho-content was used as the dependent variable (least square method was applied). The detection of the breaking point had two separate purposes: i) evaluate if different pH conditions showed different breaking points and ii) determine the percentage of phospho-content that corresponds to the inflection value.

Prior to analysis all cell proliferation-related data were tested for normality (Shapiro–Wilk test) and homogeneity of variances (Levene’s test). To investigate the influence of the modification degree of serine residues on cell proliferation, a three-level nested design ANOVA test was conducted: the type of bio-film matrix, conditioning period and time point. Post hoc comparisons were conducted using Student-Newman-Keuls. A *P* value of 0.05 was used for significance testing. Analysis were performed in STATISTICA (StatSoft v.7).

2.3. Results

2.3.1. Preparation of phospho-silk fibroin films

Our work implied using regenerated mulberry silk, which required the establishment of a suitable protocol for its phosphorylation. Previously, Winkler performed the phosphorylation of recombinant dragline silk using protein kinase A enzyme without its activator, 3',5'-cyclic-AMP [5, 88]. Different protein kinase A amounts, ATP and 3',5'-cyclic-AMP concentrations and raw silk fibroin solution quantities were attempted. Figure S2.1 demonstrates that 6:1 volume ratio between silk solution and reaction buffer (constituting \approx 161 mg of silk fibroin in 10 mL reaction) is the most favorable.

To calculate the exact level of phosphorylation, quantification of phosphate ion (Pi) was performed by the malachite green method [123]. Pi originated from dephosphorylation of silk by β -elimination (section 2.2.4). Malachite green indicates that phosphorylation can reach $\approx 60\%$ of all predicted sites. Similar values were reported previously [5]. Of all amino acids, constituting the fibroin chain, and that could undergo phosphorylation (Ser, Tyr, Thr) only Ser is a phosphate acceptor, as Tyr is not a substrate for protein kinase A [18] and Thr is $\approx 0.89\%$ of amino acids. It was estimated that a small portion of Ser (19 residues, or 3% of its total amount) and the single Thr can be phosphorylated ([3] and Figure S2.2).

The phospho-silk fibroin solution was prepared and diluted to the desired phosphorylation level, obtaining the four solutions (designated as 60%, 45%, 30% and 15%). Those solutions were casted to form films. The dilution was made with unprocessed silk fibroin solution which was also casted separately and served as a negative control (0%). The phospho-content in five distinct batches of prepared films was evaluated and is presented in Table 2.1.

Methanol (MeOH) treatment, as an indispensable step of the workflow, was made on a separate group of prepared materials. That treated group, and the untreated one, were further examined and compared in parallel, as described throughout the document.

Table 2.1. Evaluation of the phosphorylated content by malachite green reaction of different phospho-silk fibroin blends.

Silk fibroin blend type	Blends elaborated for the characterization/analysis of type				
	FTIR	DSC	Swelling	Piroxicam Release	Cytotoxicity
60%	61.3 \pm 1.5	58.8 \pm 3.4	57.8 \pm 2	60.4 \pm 4.3	54.4 \pm 1.7
45%	40.8 \pm 2.4	44.3 \pm 0.8	38.3 \pm 1.9	40.3 \pm 3.1	36.5 \pm 1.4
30%	32.1 \pm 2	31 \pm 2.2	28.8 \pm 1.5	28.4 \pm 4.6	25.2 \pm 3
15%	15.3 \pm 2	14 \pm 2.4	14.4 \pm 6.6	16.8 \pm 3.5	11 \pm 2.8

The current quantification was based on one assay (for each discrete batch) with double sampling. The calculated data represent the percentage of the maximally estimated value of inorganic phosphate (Pi), released during phospho-Ser hydrolysis.

2.3.2. Chemical and physical properties of silk fibroin

2.3.2.1. FTIR analysis

FTIR analysis showed that, regardless of MeOH treatment, characteristic absorbance spectra were obtained from the two groups (Figure S2.3). The silk fibroin conformation, reported for the untreated

films is predominantly random coil and corresponds to Amides I-II [124, 125]. Such random coil suggests prevailing amorphous structure, mainly consisting of β_1 -turns and anti-parallel chain-pleated sheets (Amide I). 3_{10} - and α - helixes [126] are also encountered (Amide II). The proximity of IR frequencies of both helical structures makes it difficult to distinguish between them [127]. Yet, our results of structural analysis indicate that β -related structures (β -sheets and β -turns) can constitute at least 40% of the secondary silk fibroin conformation even in the untreated group (Figure 2.1, **A**).

Secondary structure conformations of silk were found to be phosphorylation-dependent. The incorporation of phosphate disrupts β -sheet organization of fibroins [5]. Results demonstrate that the films with lower phosphate content have enhanced β -sheet formation, in line with previous studies [124, 125, 128]. Upon alcohol application, total amount of β -structures represented $\approx 72 \pm 5.3\%$ (specifically $\approx 60.6 \pm 2.3\%$ of β -sheets) of the total protein conformation (Figure 2.1, **B**). β -related turns formation, associated with β -sheet stacking was also increased [129].

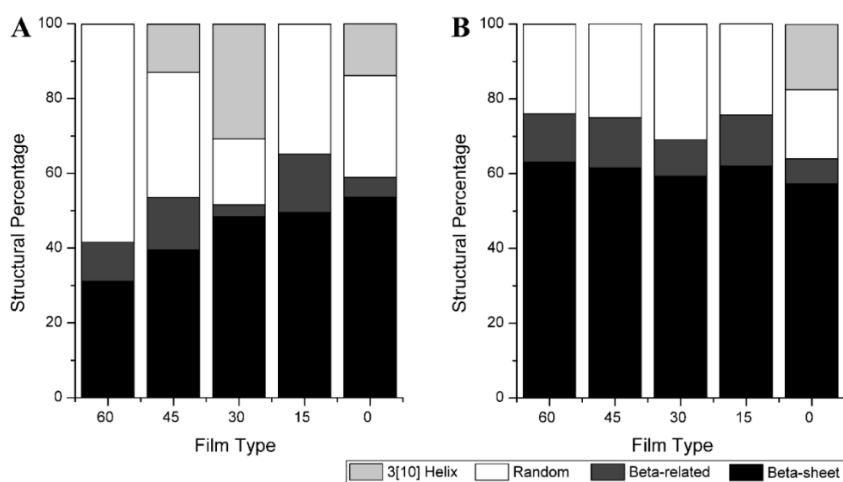


Figure 2.1. Dependency between phosphorylated content and the observed silk fibroin protein structure. Amide I resolved curve data for different Silk Fibroin film secondary structures. **A.** Dried films with no treatment. **B.** Dried films, MeOH-treated. **3[10] Helix**, 3_{10} Helix; **Random**, Random coiled structure; **Beta-related**, β -related turns.

2.3.2.2. Differential scanning calorimetric (DSC) analysis

The interactions within phospho-fibroin films were further investigated by DSC. The corresponding DSC scans are shown in Figure 2.2 **A** and **B**, main thermal peaks identified are presented in Table 2.2. A characteristic thermal trend was obtained for MeOH treated and untreated samples. Upon temperature rising, residual water evaporation, glass transition, crystallization and the decomposition of material take

place [111, 130]. After phosphorylation the intermolecular hydrophobic interactions within silk fibers decrease [131]. Thermodynamic parameters such as heat capacity depend on these intermolecular interactions [132]. A complex tendency can be demonstrated in the untreated group, which clearly defines two types of curves – related to more (0 and 15 %) and less (30, 45 and 60%) condensed materials. The order in which the MeOH-untreated materials absorb energy (in terms of measured heat flow) is different from the order in which the untreated materials do.

The glass transition temperature is inversely dependent on intermolecular interactions and protein flexibility [131]. Glass transition temperature and the crystallization peaks determined herein were found to be dependent on phospho-Ser content (Table 2.2). Higher percentage of phosphorylation results in lower glass transition temperature and crystallization onset values. Yet, T_g and crystallization peaks cannot be determined for the MeOH-treated materials. The transition from random coil to β -sheet is observed after T_g in untreated films and if β -sheet was induced prior to DSC analysis, T_g and crystallization peaks become unrecognizable. [130, 133, 134]. MeOH-treated group heat flow curves preserve their spectral localization with temperature increase. The higher uniformity of the treated group is dictated by alcohol-induced dehydration and partial pre-crystallization that counteracts the effects introduced by phosphate groups. The treated group exhibits much more pronounced decomposition endotherm peaks, indicating that the fibroin proteins building the films are found in more crystalline β -sheet state.

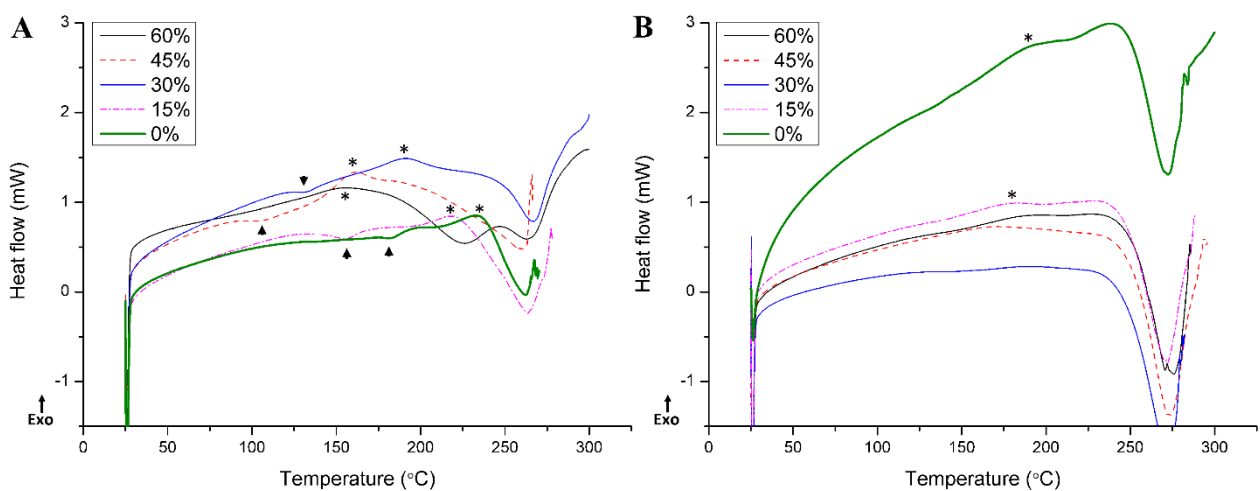


Figure 2.2. Differential scanning calorimetric analysis of **A.** untreated, **B.** MeOH-treated blended phospho-fibroin films. Individual thermograms of the corresponding samples are shown. T_g values are represented for the untreated group (**A.**, marked by the ▼ symbol). Crystallization endotherms are

designated by the * symbol. Conversely to the MeOH-treated (**B.**). A shift towards lower glass transition temperature and materials' grouping (condensed 0%, 15%; light 30-60%), as function of phosphorylated content, are recognized for untreated phospho-silk fibroin films (**A.**).

Table 2.2. Main thermal peaks identified by DSC for the phospho-silk fibroin films.

Treatment group	Peak t °C	Peak assignment	Silk fibroin blend type
MeOH untreated	>100	Glass transition temperatures determined for specific type of blends	60%
	103		45%
	130.5		30%
	155.5		15%
	181.5		0%
	150-160		60%
	160-165	Crystallization endotherms determined for specific type of blends	45%
	190-195		30%
	220-225		15%
	230-241		0%
MeOH treated	175-181	Crystallization endotherm	All types
Both groups	261-275	Decomposition endotherm	All types

2.3.3. *In vitro* swelling

Swelling behavior of materials was examined upon incubation of MeOH-treated films in a discrete pH for 24 hours. Non MeOH-treated materials could not be examined since they degrade rapidly in aqueous media. The experiment outcome is presented in Figure S3.4. From the acquired data, three important conclusions can be drawn: i) the material swelling is phosphorylation-dependent and is highest when 30% of the starting silk fibroin is phosphorylated; ii) the swelling is pH-dependent and is most pronounced at basic pH value; iii) a moderately increasing tendency to swell exists at phosphorylation range between 0% and 30%.

When analyzing the results of the t -test's, the swelling ratio values were shown to be significantly different considering the percentage of P-Ser content for all pH conditions tested (t -value(4)=2.7; $P<0.05$). Interestingly, independently of the pH condition, the estimated breakpoint occurred, in all treatments, invariably at 30% of phosphorylation.

2.3.4. *In vitro* release

For release evaluation piroxicam was chosen as a model compound. Piroxicam belongs to non-steroidal anti-inflammatory drugs (NSAIDs), used to relieve inflammatory-derived symptoms, commonly of rheumatoid and osteoarthritis, postoperative pain with good efficacy. Being a relatively small and non-polar molecule, piroxicam is particularly adequate for elucidation of alterations in

hydrophobicity of fibrous material. Prepared phospho-silk fibroin films were MeOH treated and incubated either with protease (subtilisin) or in PBS buffer. The release profiles reveal that the drug dissipates from films bi-phasically (Figure 2.3 **A** and **B**). The initial burst phase reflects the loss of piroxicam molecules possibly located very close to the film surface, lasting 3 – 10 hours, depending on material type and incubation conditions [105]. This burst is followed by slower release, decreasing over the remaining time. Prolonged incubation (>2.5 days) causes certain drug degradation, in some cases resulting in decline of release profiles [135]. Piroxicam release is very marked when silk fibroin films were incubated with protease except those with 15% phosphorylation. This effect is more leveled out for highly phosphorylated films (30, 45 and 60%). It is worth noticing that the graphs in Figure 2.3 also depict the MeOH-related release prior to incubation (-1 hour time point). It is clear that a significant amount of piroxicam is released during insolubility induction (starting from \approx 11.3% of total drug amount for 0% phospho-silk fibroin up to 55.5% of the amount for 60% phospho-silk fibroin).

Various models have been proposed for handling the release profile data, though for the case of thin slabs or solid matrixes two are commonly used: Ritger – Peppas semi-empirical model and Higuchi model [13, 120, 136]. In the current work, we exploited the above models to calculate the parameters of interest: constant k ; diffusion or release exponent, n ; and Higuchi dissolution constant, K_H . The parameters are listed in Table 2.3, designated as “Samples”, except the 0% immersed in PBS sample, since it did not result in any considerable release. Time interval τ is an additional variable used in the calculations of the models, is presented in Table 2.3. τ values have a unit of hours and differ from each other, since they depend on the release dynamics and on the extra conditions that each model may pose. The burst phase of piroxicam release from fibroin films can be qualitatively defined in the column of Higuchi τ values, as based on visual appearance of profile release (Figure 2.3 **B**). The burst phase values are considered to be suitable for applying to both models. However, some of time intervals used for Ritger – Peppas modeling are shorter than those of the whole burst phase, used in Higuchi model. These smaller values correspond to protease-mediated release. Ritger – Peppas equation (2.3) imposes that only the profile data, corresponding to the initial 60% of the released compound, may be included in kinetic calculations [13, 136]. The Higuchi model does not have such limitation, thus the full range of

burst release values can be used [136]. The output of Ritger – Peppas model provides the researcher with indication of the release mechanism and characteristics of the macromolecular network system and the drug, deduced from **n** and **k** values, respectively. The calculated **n** values appoint at quasi-Fickian release mechanism, as they are below the value of 0.5. **k** sometimes can be seen as interaction significative between the drug and its trapping material [137]. The two kinetic models mentioned can be compared through the **k** and **K_H** values. Since neither **k** nor **K_H** have unambiguous definition (although describing similar concepts), it can be examined whether they originate from the same distribution or not [136]. That is, the degree of similarity among them can be assessed. A Mann–Whitney U test was performed on these two sets of values, indicating a similarity between the sets [138]. The obtained two-tailed *p*-value of 0.34 is above the defined threshold of 0.05, therefore it cannot be out ruled that the obtained numerical sets are similar. Thus the two modeling approaches can be used in this case to analyze the data.

Table 2.3. Computed kinetic values for different release profiles of phospho-silk fibroin films.

Sample	Ritger – Peppas				Higuchi simplified		
	T	n	k	R ²	τ	K _H	R ²
60% ^{a)}	4	0.102	0.547	0.780	10	0.359	0.821
45% ^{a)}	3	0.110	0.545	0.954	10	0.528	0.906
30% ^{a)}	6	0.108	0.486	0.949	9	0.446	0.964
15% ^{a)}	4	0.0489	0.392	0.827	4	0.262	0.836
0% ^{a)}	4	0.075	0.503	0.971	6	0.429	0.675
60% ^{b)}	7	0.191	0.389	0.983	7	0.519	0.934
45% ^{b)}	5	0.256	0.366	0.929	5	0.833	0.970
30% ^{b)}	4	0.181	0.334	0.913	3	0.732	0.968
15% ^{b)}	3	0.131	0.367	0.988	3	0.655	0.924

The produced silk fibroin films loaded with piroxicam were assessed for the release of incorporated compound. **τ**, time interval applicable; **n**, release exponent; **k**, interaction constant, **K_H**, Higuchi model-derived constant. R² is the correlation coefficient. The table is based on one experiment.

^{a)} profiling obtained from protease (subtilisin)-incubated films

^{b)} profiling obtained from PBS-incubated films

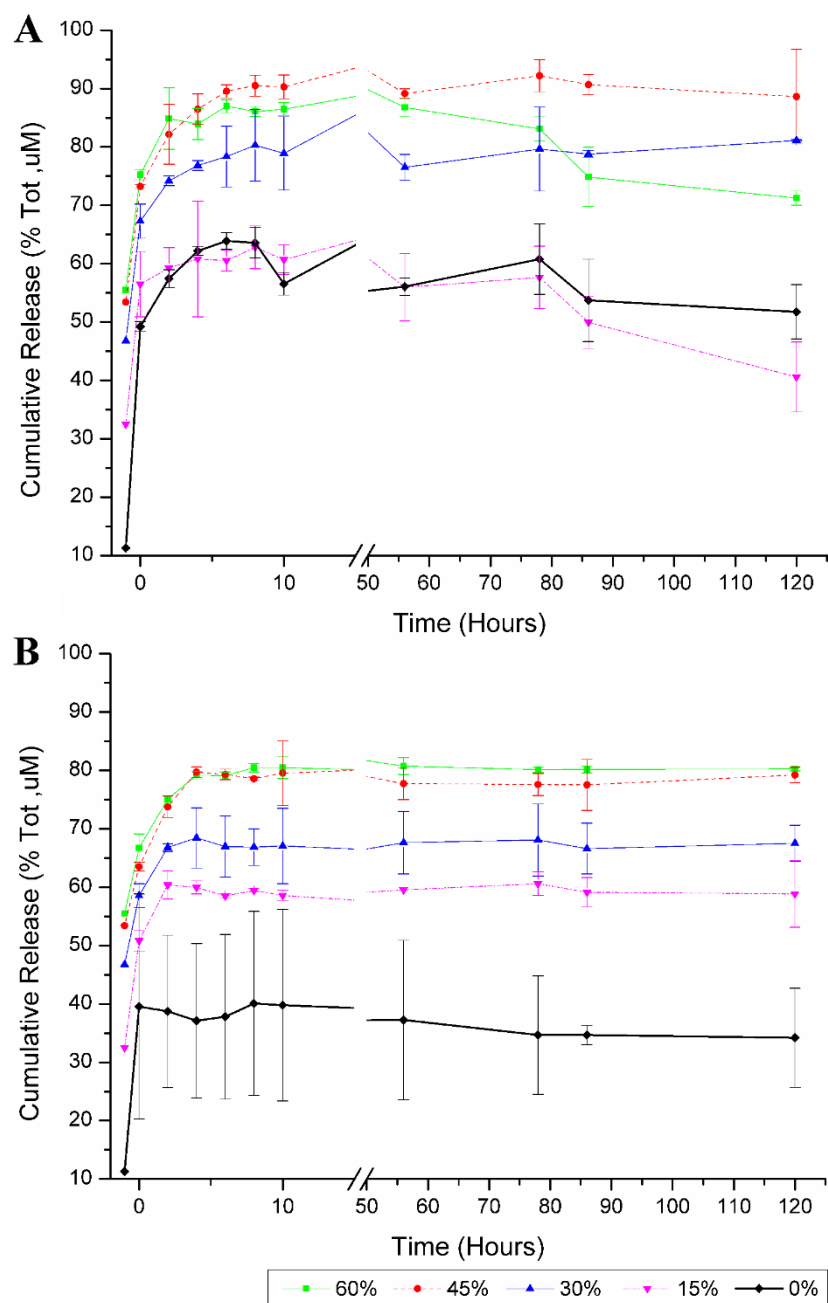


Figure 2.3. Piroxicam release profiles from silk fibroin films: **A.** enzymatically (subtilisin) mediated. **B.** non-enzymatically (PBS buffer) mediated. Note the arbitrary -1 hour time point, corresponding to MeOH treatment-mediated release of the drug. “Cumulative release” encompasses the total release of the drug, resulting from MeOH pre-treatment and incubation media as well. The graph is based on one experiment with double sampling.

2.3.5. Cytocompatibility of silk fibroin derived materials

To validate silk fibroin films for contact with cells and tissues, cellular proliferation as result of indirect contact (by exposure to media pre-incubated with the films), and direct contact (cells seeded on the films) — were examined. The outcomes of these experiments are presented in Figures 2.4 and 2.5. For indirect contact, the results show a significant inverse correlation between phosphorylation

percentage and cell proliferation (MTS-estimated, $P < 0.05$; SRB-estimated, $P < 0.05$). Nevertheless, cell viability (i.e. metabolism as assayed by MTS assay) is only meaningfully affected (<60%) by lixiviates from films with 60 or 45 % phosphorylation (Figure 2.4) (a), differently from the other types of films tested (b).

For comparison between different film modifications, direct contact of cells with phosphorylated films was quantitatively monitored by counting number of adhered cells. Cells counts are presented in Table 3.4 and representative image is depicted at Figure S2.5. The results demonstrate an inverse correlation between cell proliferation and film modification degree. The inferior cell proliferation rate per se does not necessarily signify cell death, as the environment may disfavor proliferation, while being non-toxic to cells [139, 140].

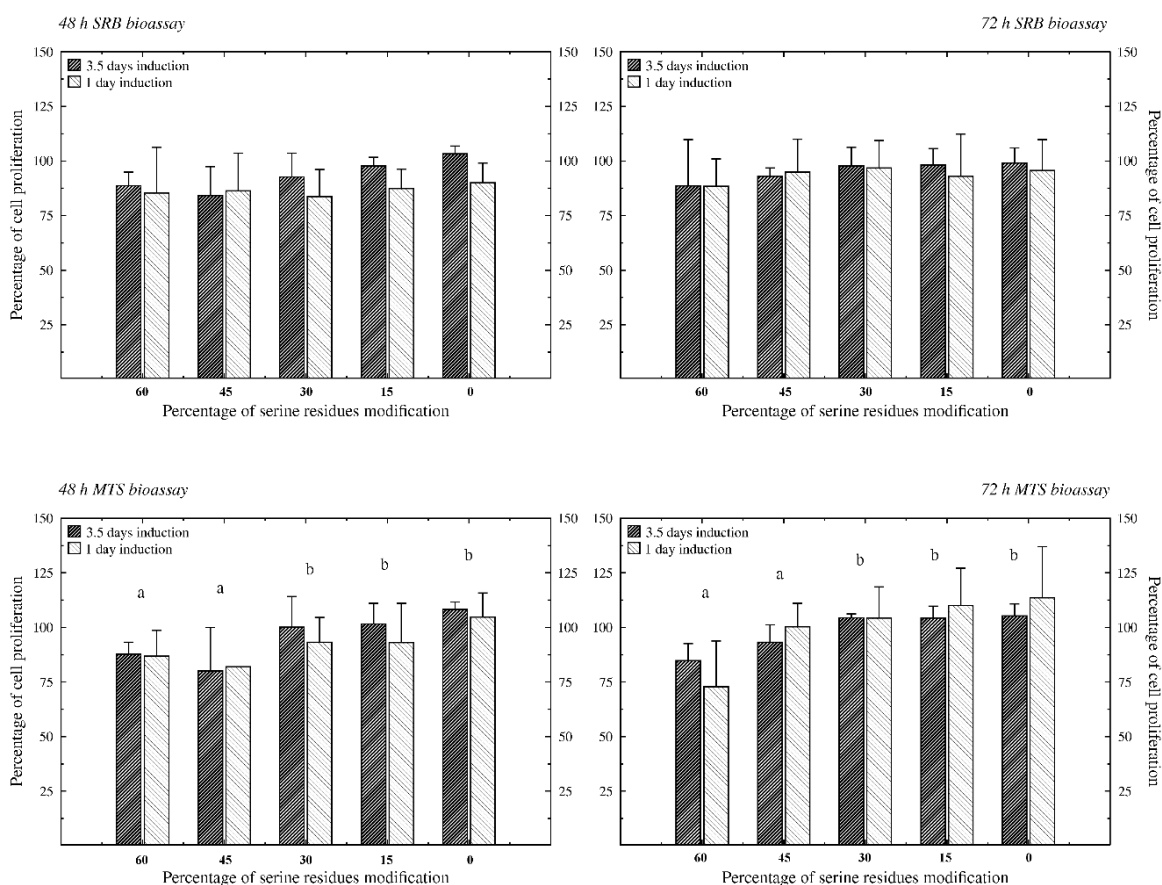


Figure 2.4. The effect of modification degree on cell proliferation, in direct contact measured by MTS and SRB assays. Different letters (a, b) indicate significant differences among treatments. The resulting data are based on three independent experiments.

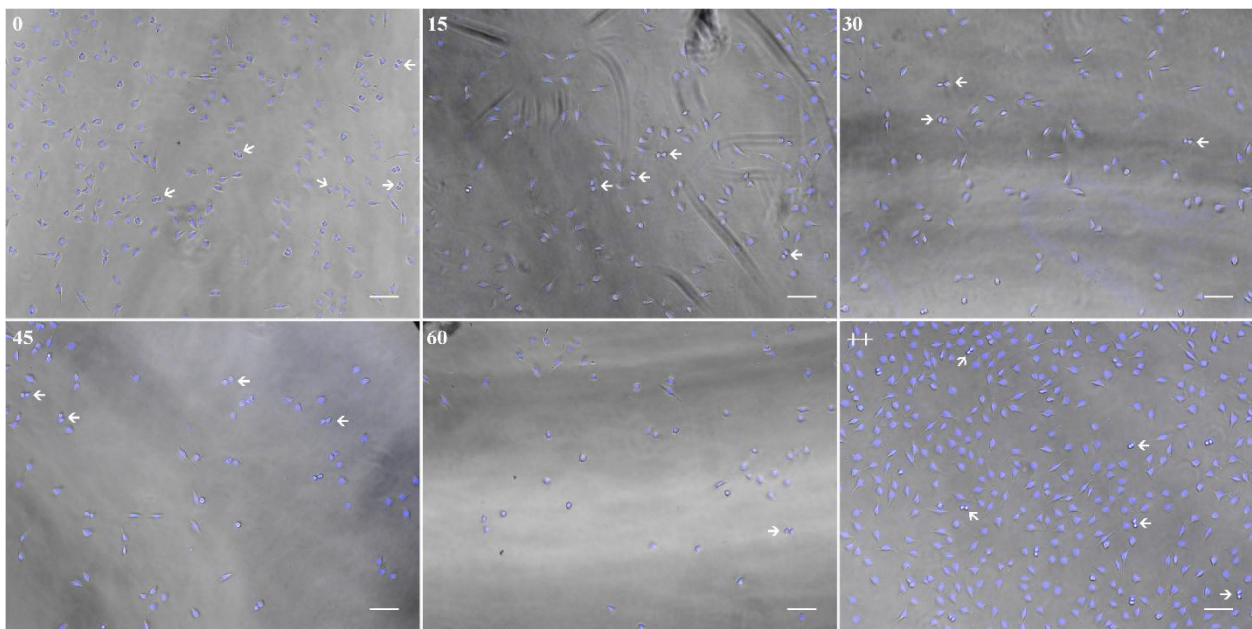


Figure 2.5. Fluorescence microscopy of the cellular proliferation on silk fibroin films with different degrees of phosphorylation. “++” designates a positive control, nuclear stain is Hoechst. Some of the newly divided cells are identified with arrows. Scale bar, 50 μm .

Table 2.4. Cell counting as function of phospho-content amounts.

Silk fibroin blend type	Cell count	Standard deviation
60%	50.25	8.131
45%	78.5	6.364
30%	96.5	24.455
15%	118	13.435
0%	152.25	30.759
Positive control (no film)	307	48.083

The current quantification was based on two independent assays.

2.4. Discussion and concluding remarks

Winkler and co-workers established a method to control the secondary structure of a genetically engineered fragment of spider dragline silk (of ≈ 25 kDa) by means of phosphorylation [5]. The protein used in their study was purified from a bacterial expression host and processed. We were interested in modifying regenerated mulberry silk fibroin, bearing in mind the expected impact of phosphorylation. Prior to enzymatic reaction, the number and location of possibly modified sites in the fibrous protein were determined *in silico*. Information of primary importance was the number of sites (and not their location), since it made possible to calculate the phosphorylation level. The exact positions of modification were not known. If one considers maximum of 12 phosphorylations for each fibroin

molecule (60% of 20 sites), the minimal amount of phosphorylations, intended to affect β -structures formation, will constitute only half. Six other modifications, then, are located on the N- and C- terminal hydrophilic domains, therefore not contributing to β -sheet disruption (Figure S2.2). Yet, the data of DSC and release profiling strongly support the dependency of fibroin structure on phosphate content. This means one the following: i) the majority of phosphorylation occur within the hydrophobic core; ii) the consequences of structural alteration are evident already at $\approx 43\%$ (6 of 14 inner sites, located in the hydrophobic part of the protein) of phosphorylation. Similarly to Winkler's previous report, we observed that phosphorylation of silk fibroin caused a decrease in the hydrophobic content of the protein, but did not completely inhibit β -sheet assembly.

We observed an opposing order of energy absorption as a function of phospho-content between the treatment groups visualized by DSC. This may result from two stabilizing effects: i) innate crystallization or hydrophobic self-association of silk fibroin; ii) polar or dipole-induced protein stabilization introduced by phosphate group. The latter effect is expected to have a strong influence on protein stability and conformation. Proteins with a highly negative value of net charge per residue tend to reduce the number of negative–negative contacts in order to accommodate the phosphate group [141]. For proteins with a moderate net charge per residue, an increase of negative–negative contacts might correlate with stronger structural stabilization and reduced hydrophobicity [141]. The local decrease of hydrophobicity near phospho-sites is approximately constant. Such a uniformly distributed effect in the case of silk fibroin strongly interferes with hydrophobic attractions between Ala and Gly. A similar stabilization effect was previously reported for other proteins as well as the formation of stable pairs between Arg and phospho-Ser residues [142, 143].

Phosphorylation influences swelling in a way that material with none or a reduced level of modification is less solvent accessible, while extensively phosphorylated material (45% and upwards) has too relaxed structure. In the first case, it may be difficult for the solvent to penetrate the hydrophobic domains; on the contrary, at high phosphorylation, solvent enters freely but is not captured within the material, therefore not contributing to swelling. Since the phospho-group of Ser has a pK_{A1} of 2.19 and pK_{A2} of 5.78 [144], the double negative charge will be present on modified Ser at neutral and basic pH.

This fact explains why the swelling ratio of films is greater at basic pH, but not acidic pH. Moreover, below pH 5 there is protein clustering due to the dominating inter-molecular hydrogen bonding, which correlates with the theoretical isoelectric point of silk fibroin ($pI = 4.53$) [145]. Extreme pH values may induce molecular contraction within the silk fibroin. Indeed, it was demonstrated that acidic pH promotes silk insolubility in aqueous media [145]. The electrostatic free energy of a protein is pH-dependent and influences its stability and conformation. This pH dependence results from the thermodynamic coupling of the side chain ionization constants and the unfolding energy [146].

Increasing phosphorylated content led to more intense release of piroxicam upon contact with subtilisin. Since it is a weakly ampholytic compound, piroxicam is negatively charged at pH values > 5.40 [147]. When the level of phosphorylation increases, a less hydrophobic compartment is formed and a negative charge predominates within the fibroin-based materials, favoring piroxicam release even without protease involvement. Similar finding was reported, stating that the higher the crystalline content of the silk, the slower the release of the encapsulated model substance [148].

The demonstration that phospho-silk fibroin film leachates are not cytotoxic but do not directly promote cell proliferation is particularly interesting. The presence of very possibly newly divided cells (indicated by arrows in Figure 2.5) on all the phospho-silk fibroin films supports this notion. Indeed, morphologically it's evident that those newly divided cells are duplets, found separately on film surface, without neighbors. These results are also in line with the previously obtained data for a L929 cell line cultivated on modified polyurethane films [149]. The determination of the film's non-cytotoxicity is a necessary step for a biomaterial to be considered biocompatible [150, 151].

To conclude, this work reports on a method for adjusting structural and biochemical features of reconstituted silk fibroin biomaterials to different uses. These modified materials can be loaded with bioactive compounds, seem to be cyto-compatible but do not actively promote cell growth or attachment. This creates the possibility of modulating drug delivery but also biological interactions. Examples of this idea may be the support of highly differentiated cells or preventing the attachment and activation of macrophages on implant surfaces [152, 153]. Phosphorylation of silk fibroin proteins may

be used to further functionalize and extend the possibilities of usage of silk fibroin for other applications.

Acknowledgements

The authors would like to acknowledge the support granted to the authors by European NOVO Project, contract no. FP7-HEALTH 2011-two-stage 278402.

Enzymatic phosphorylation of silk fibroins: a platform for the production of tunable materials

S Supplementary material.

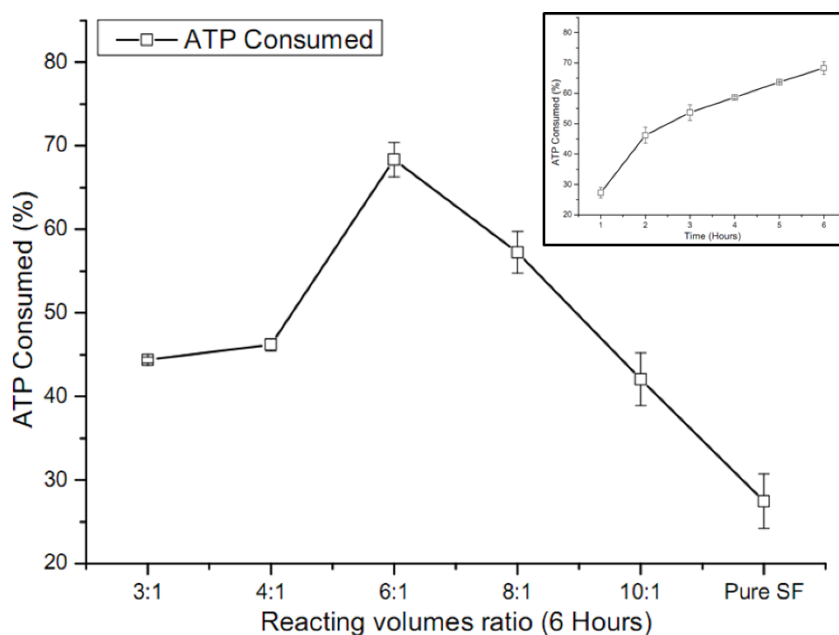


Figure S2.1. An estimation of phosphorylation reaction effectiveness as a function of volume ratio $(\text{Silk fibroin}) / (\text{Other reaction} - \text{constituting reagents})$. The results were normalized according to the control reaction in the absence of protein kinase A. Inset shows the kinetics of the optimized phosphorylation reaction (6:1 volume ratio, favoring silk fibroin) as a function of time. The graph is based on five independent experiments.

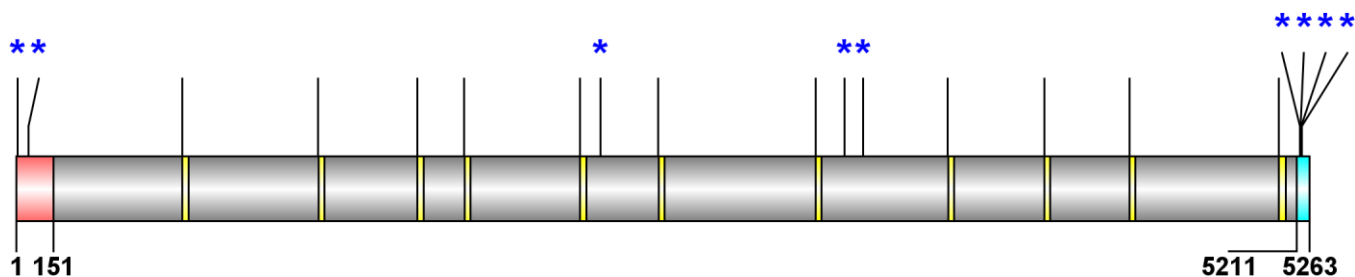


Figure S2.2. The representation of predicted phosphorylated residues in *B.mori* SF. Asterisks denote the positions, estimated by the software, whilst the remaining sites were deduced upon protein sequence analysis using the consensus motif of protein kinase A. Three major segment types, present in the protein, are indicated. Those include the N-terminal acidic and C-terminal basic domains, and 11 “amorphous” sequences. The rest is repetitive crystalline region [10]. Borders of N- and C-terminal domains are indicated. There is total of 20 estimated phosphorylation sites for each fibroin molecule, of which 14 are found within hydrophobic region and are of primary importance. The only Thr residue undergoing phosphorylation is in the first position from the left, as Ser constitutes the rest of sites. This image was elaborated using the software, included with GPS v2.1 pack [11].

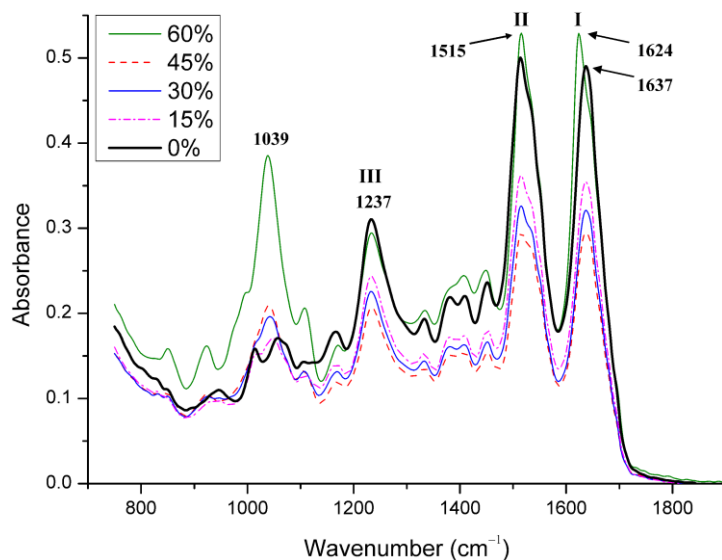
A

Figure S2.3. A. FTIR spectra of non-methanol (MeOH)-treated silk fibroin films of various phosphorylation degrees. Main Amide-related peaks, as well as P-OH deformation vibration-specific peak (of 1039 cm^{-1} , corresponding to the introduced phosphate group, [12]), are indicated. The spectral data are based on one experiment with the scan of two different areas.

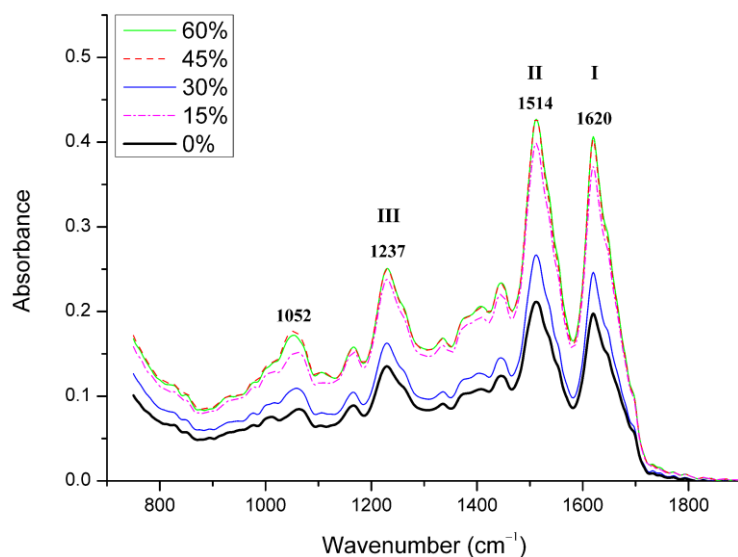
B

Figure S2.3. B. FTIR spectra of MeOH-treated silk fibroin films of various phosphorylation degrees. Dense β -sheet crystalline structures may prevent the P-OH -specific peak from being detected. Main Amide-related peaks are indicated. The spectral data are based on one experiment with the scan of two different areas.

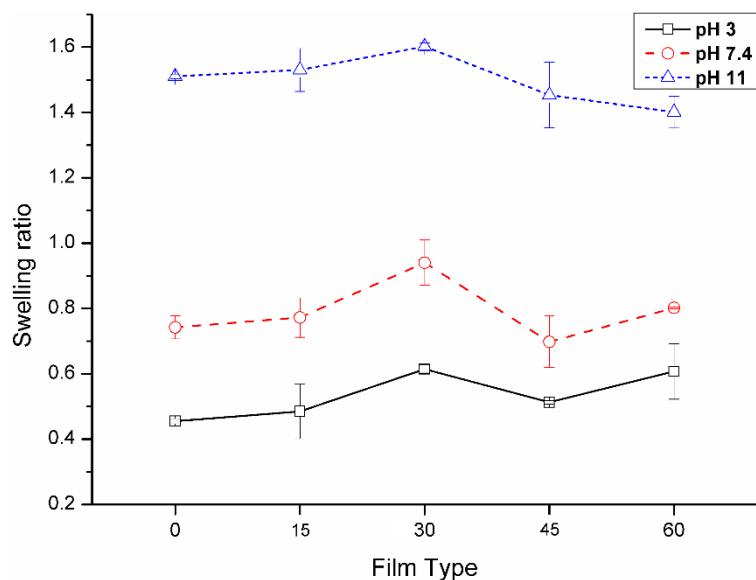


Figure S2.4. Swelling ratio of MeOH-treated phospho-silk fibroin films exposed to different pH conditions (3, 7.4, 11) for 24h. Swelling, or material enlargement due to solvent absorption, was calculated as described in section 3.2.5. The graph is based on one experiment, encompassing two distinct samples tested.

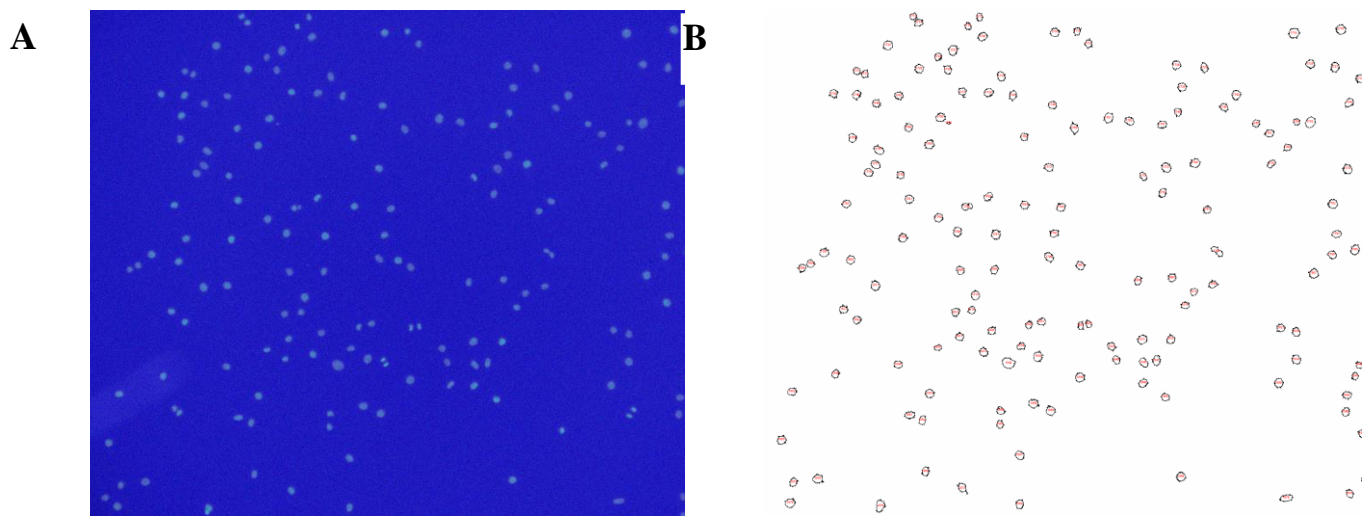
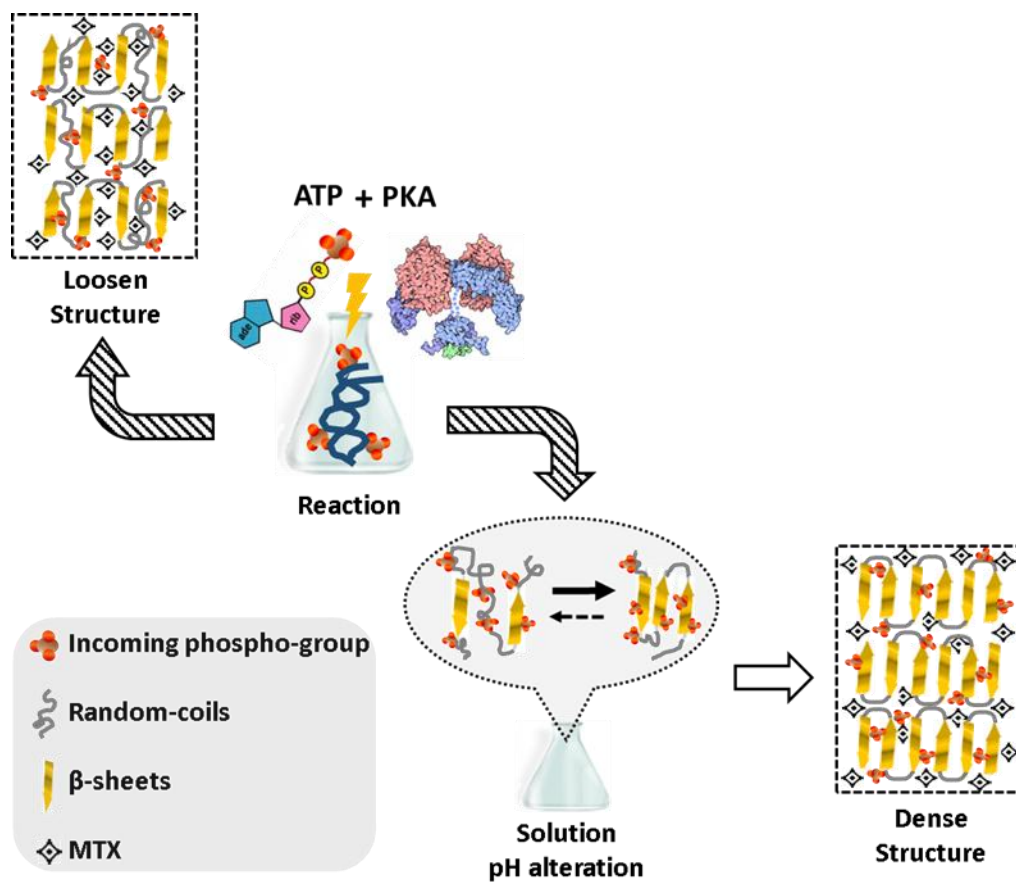


Figure S2.5. A. Representative micrograph of L929 live cells adherent to fibroin film with fluorescently labeled nuclei. **B.** The input field **A.**, processed by ImageJ v1.42h was used to quantify cell numbers in direct contact assays.

Chapter III



Chapter III

Phosphorylated silk fibroin matrix for methotrexate release

Abstract

Silk-based matrix was produced for delivery of a model anticancer drug, methotrexate (MTX). The calculation of net charge of silk fibroin and MTX was performed to better understand the electrostatic interactions during matrix formation upon casting. Silk fibroin films were casted at pH 7.2 and pH 3.5. Protein kinase A was used to prepare phosphorylated of silk fibroin. The phosphorylation content of matrix was controlled by mixing at specific ratios the phosphorylated and unphosphorylated solutions. *In vitro* release profiling data suggest that the observed interactions are mainly structural and not electrostatical. The release of MTX is facilitated by use of proteolytic enzymes and higher pHs. The elevated β -sheet content and crystallinity of the acidified-cast fibroin solution seem not to favor drug retention. All the acquired data underline the prevalence of structural interactions above the electrostatical between methotrexate and silk fibroin.

This chapter is based on the following publication: **Vadim Volkov**, Marisa P. Sárria, Andreia C. Gomes, Artur Cavaco-Paulo; Phosphorylated silk fibroin matrix for methotrexate release, *Mol. Pharm.*, 2015 Jan; 12(1):75-86

3.1. Introduction

In the last decades considerable attention has been drawn towards the production of biocompatible and bioinspired materials based on silk fibroins [18]. Silk possesses remarkable properties such as high mechanical strength, low degradability and immunogenicity [18]. Silk is a material of choice for many applications, because it is easily isolated from source cocoons and can be processed to obtain a variety of morphologically different devices [154]. Examples include silk-based materials for tissue regeneration [155], drug delivery systems [98], modulation of host immune responses [156] among others.

As a tool of material engineering, phosphorylation remains largely unexplored. Yet, in nature, phosphorylation plays a fundamental role in protein stabilization and allosteric control [106]. Thus phosphorylation can be used as tool to develop new materials. On a previous work [157], modulation of hydrophobicity and crystalline content of silk fibroin-based materials was done through *in vitro* phosphorylation of regenerated silk using the protein kinase A (PKA). It is known that under physiological conditions, the phospho-Ser residues of a protein bear a double negative charge [144] which considerably influences their microenvironment [105]. A correlation between phospho-Ser amount and the physicochemical properties of the produced films was observed, due to increased negative charge and loosen structure of phosphorylated chains.

Methotrexate (MTX) is a known folate antagonist, applied in chemotherapy for broad range of human malignancies (those overexpressing folate receptors on their surfaces [158]). MTX usage, however, may be restricted due to undesired side effects, like the toxicity to hematopoietic and gastrointestinal tissues [159], nephrotoxicity [160]. Eventually, cancer cells may acquire resistance to MTX by different mechanisms, mostly by a defective transport of the drug [161], thus compromising its therapeutic effect.

Hence, the emerged idea of controlled release of antitumor agents poses attraction as it allows for a more uniform and prolonged level of a circulating drug, accordingly lessening the negative side effects. The efficiency of MTX and similar compounds that require prolonged administration of the drug for efficient cancer treatment, is increased. Various strategies of MTX-containing formulations for medical research are currently being attempted. Among several, the injectable, thermo-sensitive polymeric

hydrogels for the intra-articular delivery [162]; combined magnetite-chitosan microspheres [163]; gelatin [164]- and chitosan [165]-based nanoparticles have been prepared. Other carrier systems of MTX delivery are known: a nanostructured lipid carrier [166] and a sophisticated dextran-peptide-MTX auto-cleaved conjugate construct [167]. In this context, materials for controlled delivery and/or release of MTX, based on silk fibroin, are described by solely one report of silk-albumin nanoparticles [168] and two patents [169, 170] dealing with the same formulation type.

In this work we studied the effect of phosphorylation and the casting conditions on a solid matrix for the delivery of MTX. Casting was done at pH 3.5 and pH 7.2 when both MTX and phosphorylated fibroin have similar charges. Initially, theoretical net charge of silk as function of phosphorylation level and the pH of resulting solution, was estimated. For MTX the charge was also estimated throughout the range of discrete pH values. Later, by combining dynamic light scattering (DLS) [171] and electrophoretic mobility measurements [172], the empirical net charges of both compounds were determined. Differential scanning calorimetry (DSC) of and release profiling of MTX from the polymeric matrixes of silk fibroin were performed to elucidate the nature of interactions between both molecules. A hypothesis of prolonged release of MTX from films of different hydrophobicity and varying incubation buffer conditions was empirically examined. A trial was made to find, in terms of pH, a favorable condition for polymer–drug interactions (whether structural or electrostatic, or both) to be used in solution-cast fibroin films production.

3.2. Materials and methods

3.2.1. Materials

Silk cocoons from *B.mori* were donated from “Sezione Specializzata per la Bachicoltura” (Padova, Italy). Kinase-GLO[®] luminescent kinase assay kit (Cat.no. V6712) and CellTiter 96[®] Aqueous One Solution (Cat.no. G358B) were obtained from Promega Corporation, USA. Tissue culture test micro plates were from TPP Techno Plastic Products AG, Switzerland, and Whatman grade 2 filter paper (Cat.no. 1002-070) was from Whatman, USA.

3.2.2. Preparation of silk fibroin solution

Sericin content was removed from the silk as described elsewhere [111]. Fibroin solution of final 2 wt% was prepared. The concentration of silk fibroin was assessed on Whatman paper *via* dry weight method, in triplicate.

3.2.3. Preparation of phospho-silk fibroin films and MTX loading

Dialyzed raw silk fibroin solution was phosphorylated as reported [157]. The phospho-silk solution (of pH ≈ 7.25) was then divided and the pH of one part adjusted to ≈ 3.5 using a 50% aqueous HCl. Consequently, kinase reaction buffer was added to the unreacted, raw fibroin solution, and mixture pH was adjusted to ≈ 3.5 value, or left untreated. Finally, the desired blends, containing various amounts of phospho-silk fibroin content and of two pH values, were prepared by casting and mixing the appropriate quantities of unmodified fibroin and phospho- fibroin solutions in 24-well plate. 60 μL of MTX stock solution was added, so that the drug final concentration of 0.2 mg ml^{-1} was established. Control samples were cast without MTX. Cast solutions of 3 mL volume were left for drying under constant air flow in laminar flow hood for 2 to 3 days at room temperature. Dry film thickness (at the bottom) was measured using caliper.

3.2.4. Quantitate determination of phosphate incorporated in phospho-silk fibroin

Phosphate amounts were determined according to the previously established protocol [157].

3.2.5. DLS and electrophoretic measurements of silk fibroin and MTX

DLS was performed on Zetasizer Nano SZ instrument, run under Zetasizer Software v.7.02 (Malvern, UK). Samples were equilibrated at 25 °C for 2 minutes prior to measurements. For 0.5 g L^{-1} MTX, the material definition was “polystyrene latex in water solvent” (all pre-defined by Malvern). For silk fibroin the material was chosen as “protein” (pre-defined by Malvern), but the solvent was determined as “silk fibroin solution” (a user-created, custom pattern). Two constants were introduced for this

“solution”: refractive index, $Ri_{(SF)}$ and solution viscosity, $\eta_{(SF)}$. $Ri_{(SF)}$ was measured for 2 wt% proteinaceous solution using ATAGO RX-9000X refractometer (ATAGO Co., USA), resulting in a value of 1.335. $\eta_{(SF)}$ was theoretically estimated from the rearranged equation for the intrinsic viscosity, $[\eta]$ [173]:

$$[\eta] \equiv \frac{\ln\left(\frac{\eta_{(SF)}}{\eta_S}\right)}{C_{(SF)}} \quad (3.1)$$

Where η_S is the solvent viscosity, i.e. water, with the value of 0.8872 cP and $C_{(SF)}$ is the fibroin solution concentration. The value of $[\eta]$ was previously given [173] as $0.23 C_{(SF)}^{-1}$, so that one obtains $\eta_{(SF)} = 1.4054$ cP. For net charge estimations, involving DLS, the results of forward scattering were exclusively used.

Electrophoretic mobility measurements were carried out at the same equipment. Malvern disposable capillary cells of DTS1070 type were used for both measurement kinds. All the measurements were performed in triplicates.

3.2.6. Net charge estimations of silk fibroin and MTX

Effective valence, or net charge, values were calculated via a stepwise process. Initially, a hydrodynamic radius, R_H of material of interest was measured by DLS. Subsequently, D_0 was calculated from the rearranged Stokes–Einstein relationship:

$$D_0 = \frac{k_B T}{6\pi\eta_S R_H} \quad (3.2)$$

Where k_B is the Boltzmann constant, η_s is the solvent (and, the solution, for the case of silk fibroin) viscosity, T is the temperature, D_0 is the diffusion coefficient. Separately measuring the electrophoretic mobility, μ and substituting D_0 and μ values into the equation of apparent valence z :

$$z = \frac{\mu k_B T}{D_0 e} \quad (3.3)$$

Where e is the elementary charge, gives the final result [172].

Theoretical estimation of net charge for both compounds was performed by the calculation of individual acid/base-derived charges, corresponding to specific pKa, using Henderson–Hasselbalch equation.

3.2.7. Thermal analysis of silk fibroin-derived materials

DSC measurements were performed with a NETZSCH-DSC 200F3 instrument (Netzsch GmbH). The experimental program consisted of sample pre-treatment and the measurement itself. Pre-treatment included heating from room temperature to 120 °C and holding the temperature for 10 min to induce sample dehydration. The temperature was then lowered to 25 °C. From this point it was increased to 300 °C, and the measurement was performed. Constant energy flow rate of 10 °C min⁻¹ was used in all steps. In case of MTX addition, its averaged weight was 0.431±0.077 mg. Average total sample weight was 2.28±0.63 mg. During the analysis the aluminum cell was swept with 50 mL min⁻¹ N₂ flow.

3.2.8. *In vitro* release

The release kinetics of MTX in two different solutions (PBS, 0.1M; ammonium bicarbonate, NH₄HCO₃, 0.1M) and two different pH values (6.25 and 8.0) was studied. Both pH values are applicable to PBS and NH₄HCO₃ solutions. The discrete pH values were chosen according to Sigma-Aldrich[®] product datasheet (code E0127), defining that pH 8.0-8.5 is optimal for the protease. Hence a lesser enzymatic activity was anticipated for the lower pH. Silk fibroin-derived materials were incubated at 37 °C in the aforementioned solutions, of which only NH₄HCO₃ contained a protease, porcine pancreatic elastase (PPE, EC 3.4.21.36) at 1:100 elastase : substrate w/w ratio. At determined time points, MTX release was quantified by absorbance measurements at 403 nm against a standard absorbance curves. To obtain kinetic values characterizing different conditions and materials, the incubation during 4 hours with 20 min sampling was done. The buffers were flashed each hour. The release behavior of MTX from polymeric systems was determined by fitting the experimental data as described [157]. Ritger–Peppas- and Higuchi- derived constants were designated as **K_{RP}** and **K_H**, accordingly. The fitting was performed in OriginPro software, v8.5.0 (OriginLab Corporation, USA), using “Linear fit” routine.

3.2.9. Cell culture

The human intestinal Caco-2 cell line (ATCC[®] HTB37[™]) was maintained under a humidified atmosphere containing 5% CO₂ at 37 °C, in high glucose Dulbecco's modified Eagle medium (DMEM) with L-glutamine and 1% non-essential amino acids, supplemented with 20% heat-inactivated fetal bovine serum (FBS) and 1% antibiotic/antimycotic solution (10.000 units mL⁻¹ penicillin, 10.000 µg mL⁻¹ streptomycin, 25 µg mL⁻¹ amphotericin).

3.2.10. Cell proliferation assay

MTS compound, in the presence of phenazine ethosulfate, is bio-reduced by cells into a soluble formazan product with an absorbance maximum at 490 nm, thus assaying active cell metabolism [121]. CellTiter 96[®] Aqueous One Solution, containing MTS, was used to assess cell viability. Triplicates for each individual assay were considered.

3.2.10.1. Test by indirect contact

(Phospho)-silk fibroin films were disinfected by triple washings with antibiotic/antimycotic solution and pre-conditioned with culture medium devoid of FBS for 6 hours at 37 °C. The medium was later harvested and supplemented with 10% serum. This pre-conditioned medium was then applied to previously seeded (1 x 10⁵ cells mL⁻¹) and adhered Caco-2 cells. The cells were further incubated for 48 hours and the proliferation was assessed with MTS. The assay was performed in duplicate.

3.2.11. Statistical analysis

All assumptions were met prior to data analysis. To investigate the kinetic modeling of MTX release among different pH-cast silk fibroin films, the dissolution constants of Higuchi (K_H) and Ritger–Peppas (K_{RP}) mathematical models were considered. These kinetic values were determined using different strategies (K_H, by fitting software; K_{RP}, by fitting and subsequent calculation), therefore, distinguished statistical methods were applied for drug release profile comparisons. A factorial ANOVA [three factors: pH of cast-film (two levels: pH 7.2 and pH 3.5); type of film matrix (four levels: 0, 15, 30, 60 % of serine residues modification) and type of incubation solution (four levels: PBS pH 8.0, PBS pH 6.25, PPE pH 8.0 and PPE pH 6.25)] was conducted to evaluate the influence of pH on release rate of MTX-

loaded SF-films, considering the Ritger–Peppas kinetic values. T-test for independent groups was applied to determine the influence of pH on release rate of MTX-loaded SF-films, considering the Higuchi kinetic values. Wilcoxon matched pairs test was considered to compare the kinetic profile of MTX-loaded SF-films among mathematical models.

ANOVA analysis [two factors: pH of cast-film (two levels: pH 7.2 and pH 3.5) and type of film matrix (four levels: 0, 15, 30, 60 % of serine residues modification)] was conducted to investigate the influence of the MTX-loaded SF-films modification degree (of serine residues) on cell proliferation.

Post hoc comparisons were conducted using Student-Newman-Keuls (SNK). A *P* value of 0.05 was used for significance testing. Analyses were performed in STATISTICA (v.7)

3.3. Results

3.3.1. (Phospho-) silk fibroin solutions: production and net charge estimation

Phosphorylation of initial silk fibroin solution was made using the developed protocol and resulted in $\approx 60\%$ of phosphorylation after 3–4 hours. The phosphorylation % is the percent of all sites, suitable for enzymatic phosphorylation that were successfully modified [157]. Phosphorylation of Ser residues in fibroin was further analyzed by malachite green for their % of released maximal phosphate (Table 3.1).

In an attempt to enhance MTX–fibroin electrostatic interactions and thus promote more prolonged drug release, we initially theoretically estimated the charges of both compounds as a function of pH, and specifically to fibroin, also as function of its phosphorylation. The rationale for doing this was the inability of existing tools to accurately calculate net charge (*z*) of the phosphorylated protein. It can be seen that phosphorylation level inversely correlates with overall positive charge of a protein (Figures 3.1 and S3.2). The pH range between 3.5 and 4.0 was of particular interest, since the extensively modified protein (60% phosphorylated) and MTX possess opposite charges in that interval. With pH increment, both proteinaceous solution and the drug acquire negative charges, rendering electrostatic interactions less favorable. This trend of silk charge change is in agreement with the results obtained by *in silico* tools, available online (for example, Protein Calculator v3.4, <http://protcalc.sourceforge.net>) applied on full protein sequence (accession nr. [AF226688](#)). To test the polymer–drug interactions, two discrete

casting pH values were chosen: 3.5 and 7.2. Phosphorylated fibroin was produced, its pH value adjusted and net charge calculated, while MTX charge was elucidated for two distinct pH values.

During the experimental estimation of net charges of both compounds they demonstrated a positive z values within acidic pH range (Figs. 3.1; S3.2). This magnitude of charge is clearly seen for fibroin solution and, to a lesser extent, for MTX.

Table 3.1. Evaluation of the phosphorylated content (phospho-Ser) by malachite green reaction for different silk fibroin blends. The percentages denote phosphorylation extent of all possible sites.

Phosphorylation degree	Blends elaborated for the characterization/analysis of type		
	DSC (Batch 1)	MTX Release (Batch 2)	Cytotoxicity (Batch 3)
60%	61.0±1.11	59.95±4.96	56.94±2.52
30%	29.9±1.54	30.67±2.4	32.61±2.7
15%	15.54±2.76	16.32±2.64	15.05±1.92

The current quantification was based on one assay (for each separate batch type) with double sampling. The calculated data represent the percentage from the maximally estimated value of inorganic phosphate (Pi), released during phospho-Ser hydrolysis.

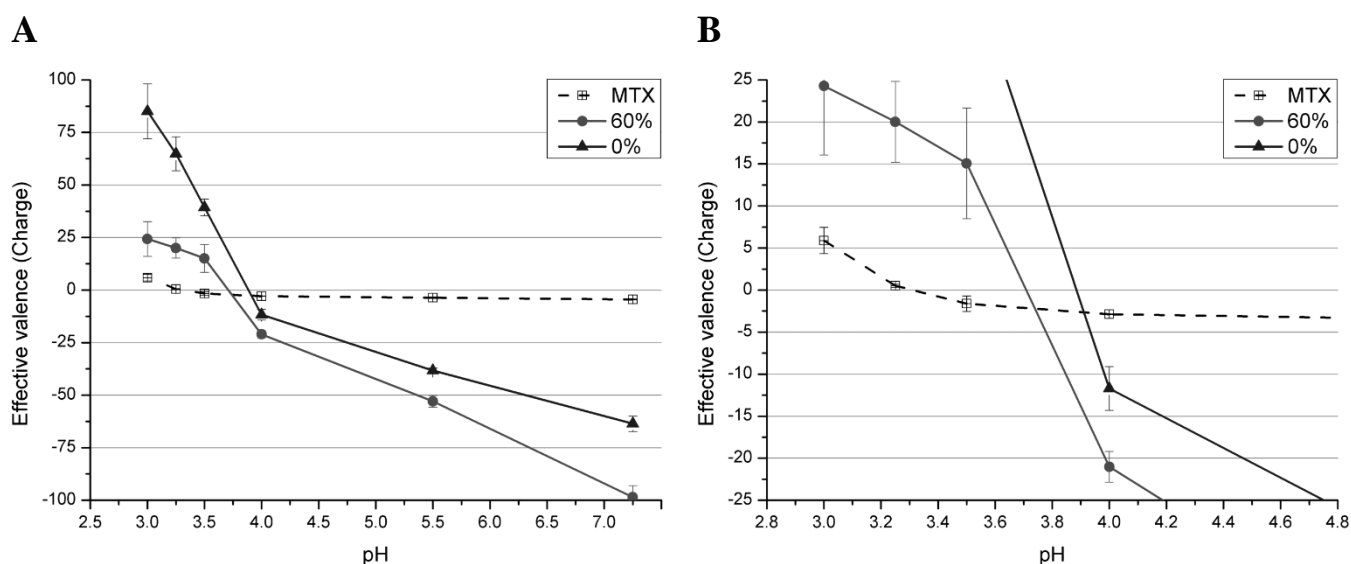


Figure 3.1. Experimental estimation of silk fibroin and methotrexate (MTX) charges as pH function. **A.**, full-scale representation. **B.**, zoomed-in representation. The increase of negative charge resulting from phosphorylation is observed. For better clarity, the additional curves, corresponding to material types 15% and 30% (appearing between 0% and 60% types) are relocated to supplementary part.

3.3.2. Optimization of production of MTX-loaded films

Considering the desired effect of weaker electrostatic repulsion between fibroin and MTX, at acidic pH, we cast proteinaceous solutions at two discrete pH values and added the drug. The first casting was performed at nearly neutral pH of 7.25 and the second at pH 3.5. During fibroin solution titration with HCl, a protein loss of $\approx 3\%$ from its soluble amount was detected. This happened due to the hydrophobic self-aggregation of silk, where the local pH drop (at the immediate environment of HCl) was the most significant [16]. To avoid the possible gelation of acidified silk solution during the drying process, considerable air flow is needed. In the current work, thicker films obtained by solvent casting in tissue culture test plates (3 mL solution in 3.29 mL well, of 7.45 cm² bottom square), rendered methanol treatment (insolubility induction of dried materials) dispensable. “Thicker films” on this context have increased thickness, related to the previously employed approach [157], where 5 mL solution was cast in 10 mL Petri dish of 32.17 cm² bottom square. The currently obtained films were of 0.08 – 0.12 mm or 0.12 – 0.16 \pm 0.03 mm thickness, originating from casting pH values of 3.5 and 7.2, respectively.

3.3.3. Thermal analysis of silk fibroin-derived films

The thermal analysis of silk fibroin-derived films pursued two goals: to demonstrate structural differences of dried materials imposed by pH and phosphorylation, and to monitor existing interaction between fibroin and MTX. As seen in Figs. 3.2 and 3.3, in comparison to neutral pH-cast films, acidic pH-derived materials exhibit increased amount of β -sheet structures, resulting in the smoothing of thermogram curves [130]. Silk fibroin glass transition temperature (T_g) characterizes a structural shift, preceding the formation of β -sheet arrangements. For the material cast at neutral pH with the following phosphorylation degree of 0%, 15% and 30%, T_g onset was \approx 135-145 °C; similar result was observed solely for the unmodified material (0%), cast at acidic pH (Figs. 3.2, **A**; S3.3). Thermodynamically, acidic pH favors silk self-aggregation [16], therefore T_g is not observed for pH 3.5-cast films. A crystallization peak is only clearly evident for 0% phosphorylation for the pH 7.2-cast film (\approx 217 °C;

Figure 3.2, **A**). Fainter crystallization events could still be observed for 0 and 15% phosphorylated matrices, casted at acidic and neutral pH, respectively (Figures 3.2, **B**; S3.3, **C**). For all the materials at different phosphorylation degrees the decomposition occurs at 275 °C. Some films presented a bimodal decomposition endotherm [174], as can be seen on Figures 3.2 and 3.3, **B**. This fact may be due to the non-uniformity of the material that causes stepwise energy absorption.

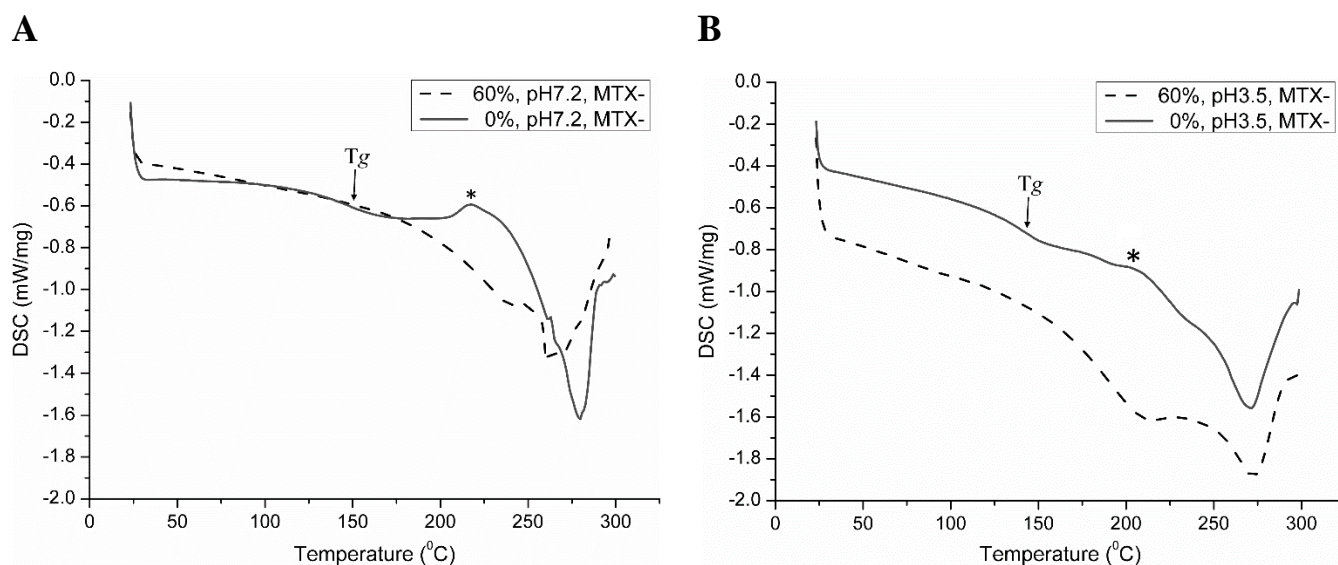


Figure 3.2. Thermal analysis of silk fibroin films, without (“MTX-”) methotrexate embedded. **A.**, Fibroin films cast at pH 7.2. **B.**, Fibroin films cast at pH 3.5. Crystallization peaks are denoted by asterisks. Where possible, the onset temperature glass transition (T_g) is indicated.

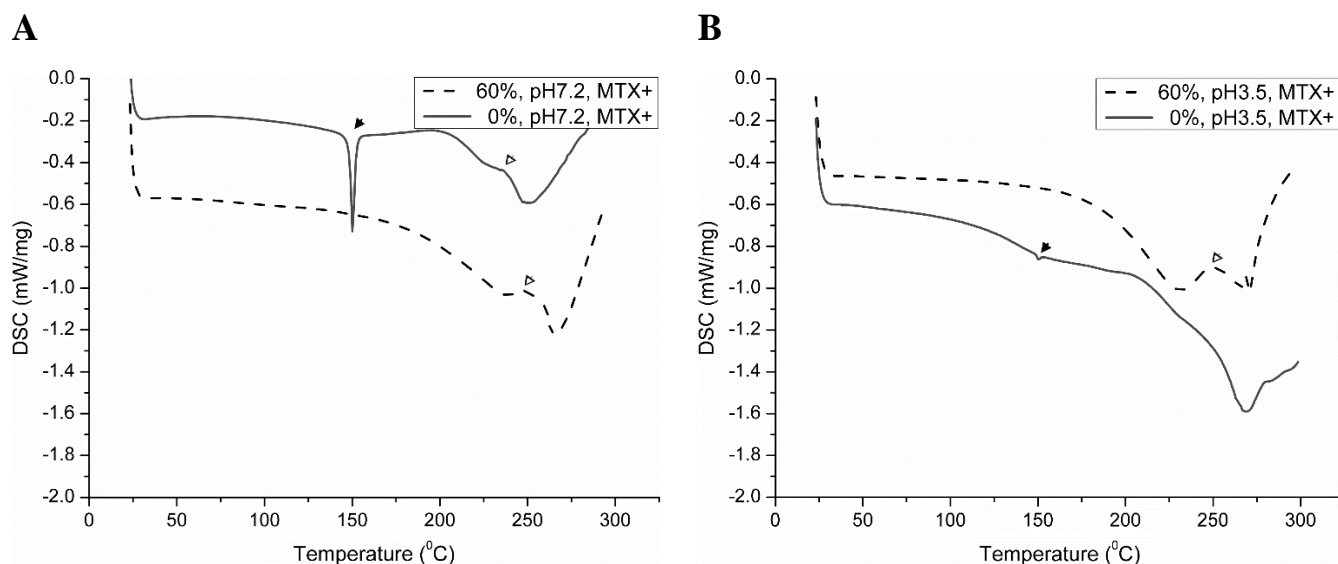


Figure 3.3. Thermal analysis of silk fibroin films, with (“MTX+”) methotrexate embedded. **A.**, Fibroin films cast at pH 7.2. **B.**, Fibroin films cast at pH 3.5. Several, though not all, methotrexate-related peaks are denoted with arrows. Each arrow type (\blacktriangledown , pseudo-melting or \blacktriangledup , recrystallization coupled to partial decomposition) corresponds to distinct thermal event, resulting from the incorporated MTX.

The DSC curve of MTX powder presents several distinct peaks (Figure 3.4). The first peak at ≈ 175 °C can be attributed to pseudo-melting or dissolution [175]. While the second peak at ≈ 224 °C is mainly due to solid–solid transition [176] or partial melting of the drug crystalline form [175]. Finally, MTX has short recrystallization peak at ≈ 238 - 247 °C, which precedes its thermal decomposition at 252 °C. In general, MTX thermogram displays gradual, ongoing crystallization, throughout the entire observation. Thus, the positive enthalpy, or absorbed heat, is constantly decreasing.

The addition of the drug to the cast silk solution suggests variable interactions between MTX and fibroin upon film drying. When comparing the DSC curves for silk-based films with and without the MTX, independently of the phosphorylation degree of the material, a similar trend of emerging MTX-derived thermal peaks was observed. The three main events, developed as only MTX powder had been heated, are depicted in Figure 3.4. Consequently, addition of the drug to the non-phosphorylated material induced the formation of pseudo-melting peak at 150 °C with a partial decomposition at 240-250 °C (designated by filled (\blacktriangledown) and empty (\triangledown) arrows, respectively, on Figures 3.3; S4). MTX incorporation also shifted the main decomposition endotherm. This shift was significant for the 0% phosphorylation material cast at pH 7.2 ($280 \rightarrow \approx 249$ °C), but less pronounced for the other materials (Figures S3.3 and S3.4, **D**). Moreover, a clear decrease on the energy absorption (E_{abs}) was evident for all, except 60% modified and near neutral pH-casted matrixes (compare Figures 3.2 and 3.3; S3.3 and S3.4). Acidic pH-casted materials of 0% and 15% phosphorylation demonstrated slight and more pronounced increase of E_{abs} upon MTX addition, respectively. 30% and 60% material types had mainly and highly decreased E_{abs} , respectively, with MTX incorporated. However, it can't be concluded that the stronger drug–polymer interaction is evident for 7.2 pH-derived materials, based solely on the presented DSC findings.

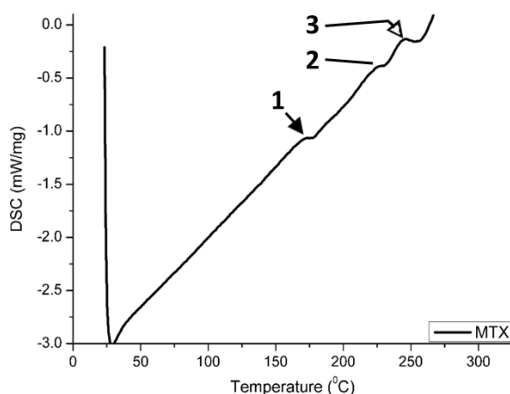


Figure 3.4. The representation of. DSC curve of methotrexate (MTX) powder. The three main thermal events are indicated. First (▼), pseudo-melting; second (without special designation), solid–solid transition; third (▽), recrystallization coupled to partial decomposition. Due to the specificity of the used procedure (section 4.2.4), MTX dehydration endotherm is not shown in the current presentation.

3.3.4. *In vitro* release profiling of incorporated MTX

The structure of the material influences the incorporated MTX release profile. Prepared phospho-fibroin films were incubated in PBS with or without protease (porcine pancreatic elastase, termed as PPE solution). It is important to mention that no methanol treatment was performed prior to incubation. From our previous work, it is known that the pre-treatment of the material with methanol can lead to a significant loss of incorporated drug (up to 55% of its initial content [157]). Thus, it is important to carefully choose protocols that preserve the drug prior to its actual release.

Since preliminary tests with MTX indicated rapid drug dissolution (data not shown), a short-term profiling with frequent sampling was conducted. The release profiles, depicted in Figure 3.5, reveal several important conclusions about the drug dissipation from the films. For all incubation conditions, the release of 80% of MTX was achieved within two hours and there is no significant difference between PBS- or PPE- mediated release for neutral pH-cast films. A different profile was seen for the acidic pH-derived materials, where protease facilitated drug dissolution (Figure 3.5, **B**). In the latter case, it is possible to denote the burst phase during the first hour of incubation, resulting in nearly complete drug release (>90%). It is worth mentioning that each individual curve in Figure 3.4 results from the average of four independent profiling experiments, corresponding to 0%, 15%, 30% and 60% of phosphorylation content. Such representation was chosen since the existence of considerable similarity between discrete release profiles for each matrix type (Figure S3.6). Thus, for simplicity of the display, only averaged profiling curves for two major matrix types (neutral- versus acidic- pH-cast) were presented. What nevertheless does not mean that the later reported kinetic values resulted from the calculation, involving cross-averaging of materials with varying phosphorylation.

Two theoretical approaches were implemented in order to better understand the release profiling of MTX from the phosphorylated materials, namely Ritger–Peppas semi-empirical and Higuchi models

[13, 120, 136]. For Ritger–Peppas, the constant K_{RP} and diffusion (or release exponent) n values were estimated, similarly to the K_H diffusion value for Higuchi method.

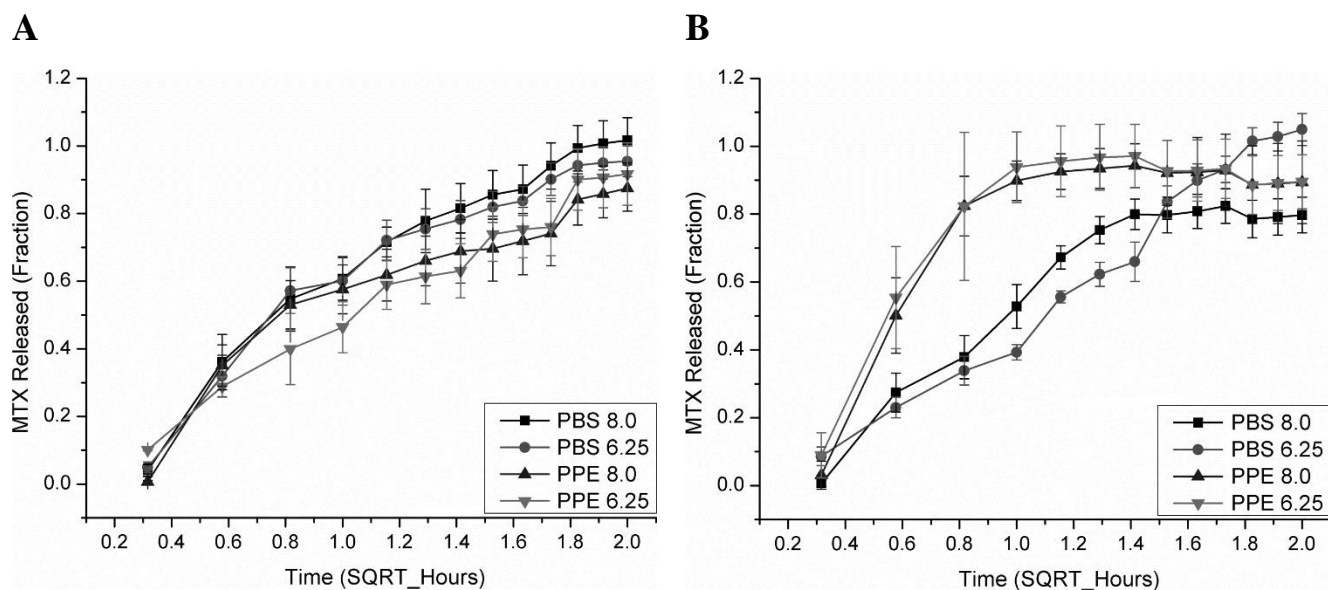
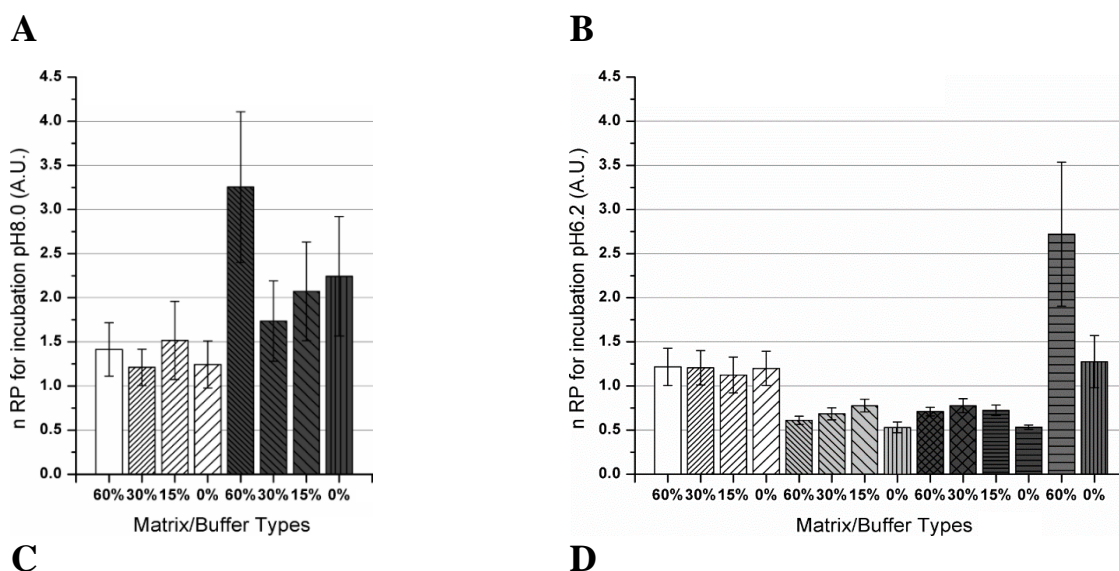


Figure 3.5. Release profiling of silk fibroin films with incorporated MTX. **A.**, Fibroin films cast at pH 7.2; **B.**, Fibroin films cast at pH 3.5. Each curve is an averaged value of the four discrete profiles, corresponding to 0...60% phosphorylated material. Examples of individual release profiles are presented in supporting figure S4.6.

The release mechanism and characteristics of both macromolecular network system and the drug can be deduced from n and K_{RP} values by applying Ritger–Peppas (RP) model to release profiles. Software-given n values suggest super Case-II transport[177] for all the films incubated at pH 8.0 (Figure 3.6, **A**). Near-neutral pH cast matrixes, incubated in PBS at pH 6.2, also demonstrate super Case-II transport values. Nevertheless these are very similar in between and close to the values characterizing a Case-II mechanism (for which $n = 1$ [178]; average of the presented four amounts is 1.184 ± 0.036 ; Figure 3.6, **B**). Other materials, cast at pH 7.2 and pH 3.5 and immersed in PPE and PBS, respectively, have an anomalous release mechanism (for which the inequality: $0.5 < n < 1.0$ holds). Finally, pH 3.5-cast and pH 6.2 PPE-immersed films again demonstrate a super Case-II release process. Importantly, n values were not available for all the conditions examined. For all the materials in both casting groups, pH 8.0 PPE-assisted MTX release resulted in initial burst phase that was so great that it rendered impossible to apply

RP modeling. Accordingly, MTX release from 15% and 30% modified matrixes, acidic pH-cast, in pH 6.2 PPE-assisted incubation generated drug burst, non-compliable with RP conditions [178]. Anomalous transport appoint on complex release process, resulting from coupling of solvent diffusion into the material and its subsequent relaxation [179]. Case-II and super Case-II mechanisms relate to the state of rapid solvent mobility due to increased polymer relaxation [178, 180], provoking massive release of entrapped compound. The only difference between the latter two situations is that in a super Case-II system type, saturation of the release curve is reached faster.

MTX diffusion values from RP model, K_{RP} , are presented in Figure 3.6, **C** and **D**. In RP model, pH 8.0, PBS-immersed matrixes of both casting groups seem to release the drug more easily upon lesser phosphorylation, although for neutral pH-cast this tendency is more prominent (Figure 3.6, **C**). For incubation pH 6.2, both PBS- and PPE- immersed matrixes of 7.2-casting group showed the aforementioned trend (Figure 3.6, **D**). Surprisingly, the PPE-mediated diffusion sub-group manifested decreased K_{RP} values. 3.5-casting group in PBS incubation did not display a considerable bias and PPE-incubated values were high (Figure 3.6, **D**). It can be seen that K_{RP} values for incubation pH 6.2 substantially repeat the tendency of n values (compare panels **B** and **D** of Figure 3.6).



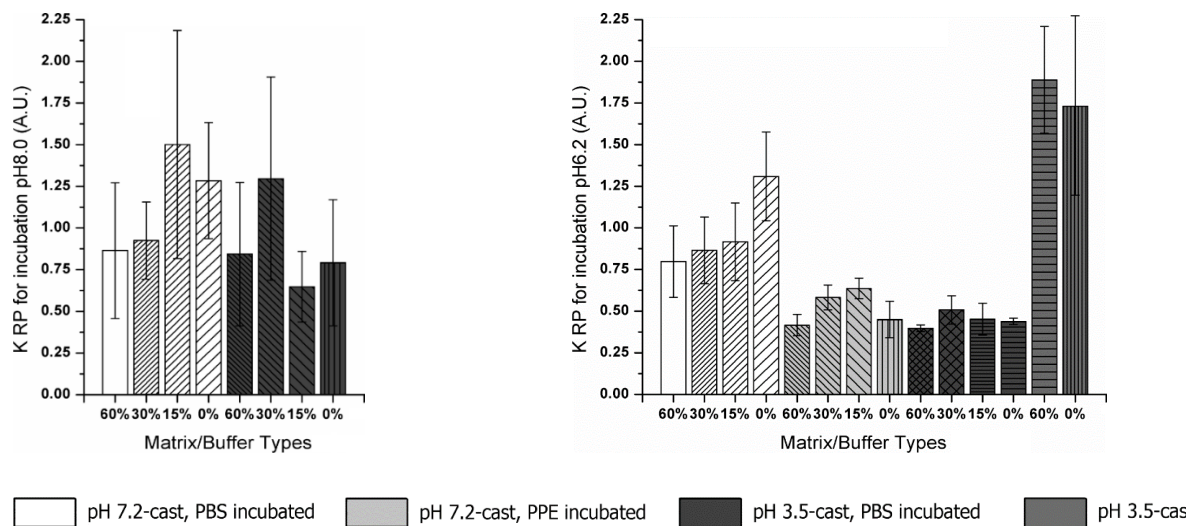


Figure 3.6. Figure legend is at the bottom of the next page.

Higuchi model-derived diffusion parameter, K_H , is depicted in Figure 3.7. Being a more simplified model, Higuchi made it possible to fit the empiric data for all of the conditions. Thus, K_H was obtained directly from the fitting algorithm. From the incubation buffers of two discrete pH it can be concluded that, akin to K_{RP} , K_H values undergo gradual increase as modification levels drop (Figure 3.7). But K_H increment within each group is more prominent than that of K_{RP} . The clear exception is constituted by a pH 3.5-cast group of materials, incubated with PBS, showing somewhat decreased diffusion of MTX within a group, as function of phosphorylation. It can be also stated that pH 8.0 facilitates drug release.

Based on statistical analysis, performed for K_{RP} and K_H , it is evident that for K_{RP} no significant differences were observed among values of two major types of MTX-loaded films (7.2- versus 3.5-cast). The phosphorylation level does not influence K_{RP} , yet the incubation solutions do. Specifically, pH 7.2-cast matrixes of 60% modification, immersed in pH 6.2 PPE, correspond to the lowest K_{RP} and this value is different from all other conditions. Conversely to pH 3.5-cast, non-modified matrixes, incubated in pH 6.2 PPE, where 0% and 60% correspond to the highest K_{RP} . K_H values analysis reveals that no differences were observed among values of two major types of MTX-loaded films, considering percentage of degree modification (0...60% phosphorylation), however, various incubation solutions were significantly different. Independently of pH value (3.5 or 7.2) of the cast films, no differences among modification degree was encountered, whilst all incubation solutions observed were different among themselves.

Kinetic values, obtained from substitution of MTX release profiling data to Ritger–Peppas (RP) model. The incubation of films in two distinct media (PBS or PPE) was done. Two discrete pH values of 8.0 or 6.2 were used. **A.** and **B.** Release exponent **n** values for different phosphorylated silk fibroin films, computed by model. Direct output of a fitting software. **C.** and **D.** For different matrixes, RP model-derived diffusion significative, K_{RP} , was calculated substituting **n** values to the empirical equation, described previously [13]. Data are reported with standard error and based on one release experiment with double sampling.

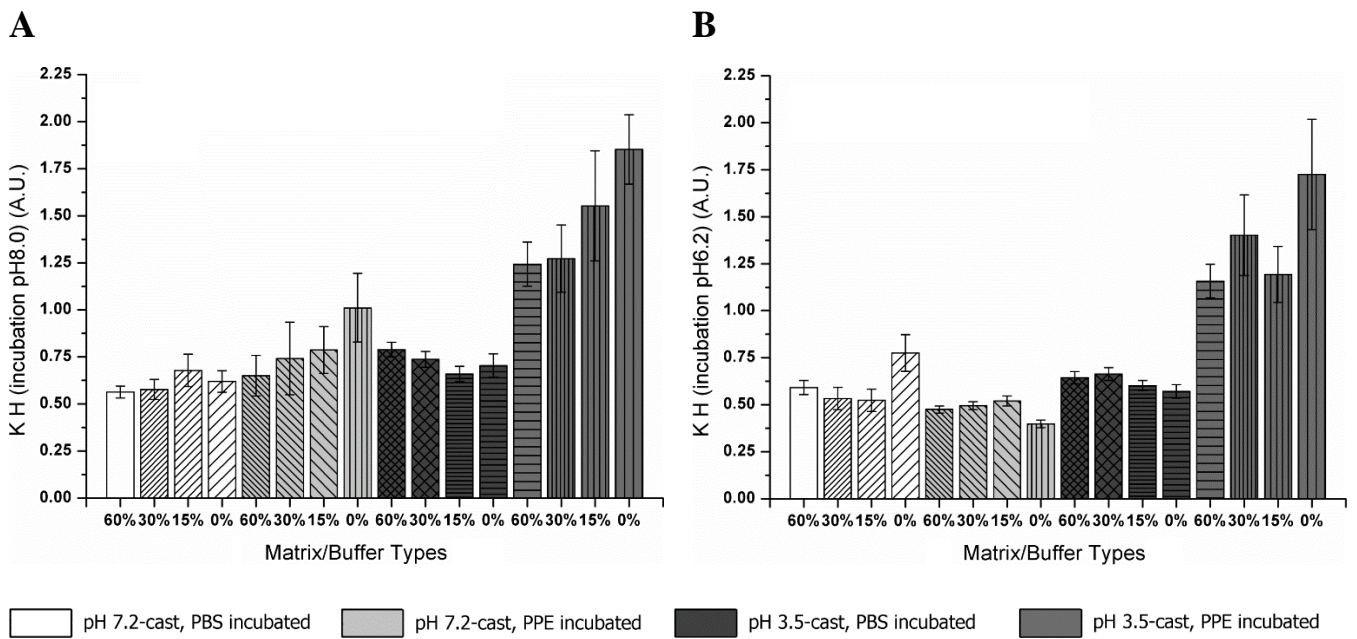


Figure 3.7. Kinetic values, obtained from substitution of MTX release profiling data to Higuchi model. The incubation of films in two distinct media (PBS or PPE) was done. Two discrete pH values of 8.0 or 6.2 were used. Higuchi diffusion, K_H , values for different phosphorylated silk fibroin films, were computed by the corresponding model. Direct output of a fitting software. Data are reported with standard error and based on one release experiment with double sampling.

3.3.5. Indirect contact effect on cell proliferation

According to the literature [149, 150] and our previous experience [157] elevated hydrophilicity disfavors cell attachment. Therefore it was decided to evaluate the bioactivity of the films on mammalian cells by indirect contact. MTX-loaded films were incubated with cell culture medium as described, allowing the MTX to release into the medium. Cells were then cultivated in contact with the pre-conditioned medium and their proliferation was monitored. Based on Figure 3.8 it is evident that neutral-cast materials possess higher MTX retention, than their acidic pH-cast counterparts. As expected MTX acted as a non-proliferative agent. The proliferation rate was lower when the MTX release was higher. Additionally, films with higher extent of phosphorylation were able to retain the drug for longer time. This conclusion is clear from both casting pH values, however, in the neutral-derived films the trend falls within statistical error, whilst in the acidic pH-derived it does not.

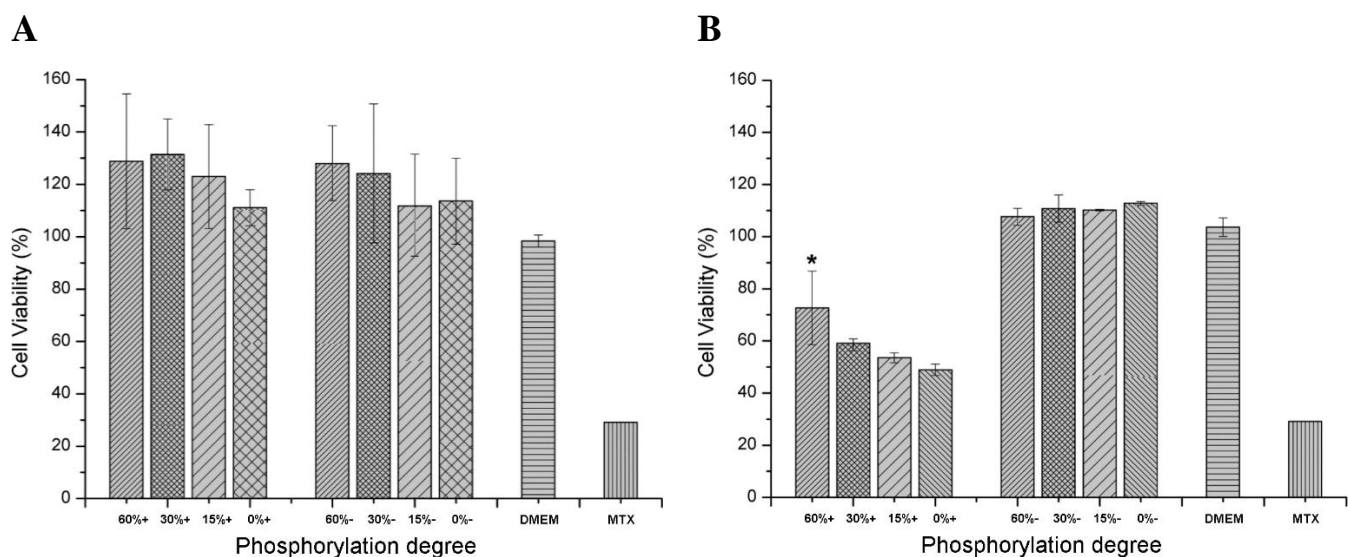


Figure 3.8. The viability of Caco-2 cell line, cultivated on lixiviates, derived from 6 hour-incubation of growth medium with silk fibroin MTX-loaded films. **A.**, pH 7.2-cast films; **B.**, pH 3.5-cast films. “+” and “-” denote the MTX –loaded or –devoid fibroin materials. DMEM = cell growth medium only, a positive control. MTX = methotrexate at 0.2 mg/ml concentration, a negative control. Statistically significant difference is denoted by asterisk.

3.4. Discussion

The current research examined the aspects of MTX–silk fibroin interactions in a changing environment of solution pH and silk phosphorylation levels. Owing to the hydrophobic nature of silk fibroin, it was our working hypothesis to examine whether a prolonged, time-controlled release of an incorporated, relatively non-hydrophilic drug [181], MTX, could be accomplished. The common practices are encapsulations of compounds into environments of similar hydro –phobicity or –philicity. Considerable amount of examples can be found in literature ([182] and references within), supporting this notion. From this perspective, the compartment of fibroin matrix was assumed to be suitable for MTX incorporation. The basis for sustained drug release was theoretically regarded to its low solubility in aqueous solutions. Hence, by tailoring silk hydrophobicity through its chemical alterations a trial was made to create the conditions of favored MTX retention within a fibroin matrix.

The mechanism of fibroin self-association (whether during natural spinning process or in the cast regenerated fibroin solutions) was postulated to be a thermodynamically favored β -sheet hydrophobic aggregation [10, 104]. It was also established that silk fibroin phosphorylation impedes fine β -sheet stacking in the secondary protein conformation [5, 157]. In this work, different blends (or batches) of

matrixes were used for all the studies because the physical amount of the elaborated material makes it very hard to use in all three tests. Moreover, we would like to demonstrate the repeatability and consistence of the production method. As can be seen very similar materials are obtained (in terms of phosphorylation, Table 3.1) for different batches. To examine the nature of occurring interactions, two distinct pH values were tested (3.5 versus 7.2). At low pH, actual net charges of both protein and drug appear to be considerably higher than their theoretical values. The measured z values were higher than could be expected, based on the theoretical estimation (Figures S3.1 and S3.2). This may be attributed to increased R_H estimation by DLS, resulting in decreased D_0 (see section 3.2.6), since the possible augmentation of μ is inconsistent with the tendency, previously reported for this variable[183]. In particular, fibroin is known to rapidly form aggregates below pH 4.59 [16]. These less soluble structures decrease diffusion rate [171] and result in higher estimation of a hydrodynamic radius, which leads to the calculation of elevated net charge. The hydrophobic clustering *per se* could however cause enhanced charge accumulation [184], in this case, positive. Given the fact that at nearly neutral pH electrostatic repulsion between both components should also exist, it is necessary to clarify why MTX affinity to fibrous film was significantly lower at acidic pH. It is possible that while forming a dense, β -sheet clustering, MTX is mainly excluded from the resulting structure, since no favorable electrostatic interaction is present, or it is not strong enough.

DSC analysis further enforces the observation of varying polymer–drug interactions as the function of pH. For silk fibroin, its self-assembly [16] during the drying process is comparable to that induced by methanol treatment of dried fibrous materials, obtained by solvent casting [130, 133, 134, 157]. The incorporation of phosphate groups causes T_g to shift slightly to lower values, inducing a plasticization effect [131] (Figures 3.2 and S3.3). Extensive phosphorylation (60%) eliminates T_g completely (Figure 3.2); moreover, T_g cannot be determined precisely (or possess a single value) in semi-crystalline polymers like silk fibroin and similar ones [185, 186]. Broad glass transition curves are ascribed to the composition heterogeneity of the elaborated materials, composed of polymer blends. For that reason only the onset of glass transition is marked in the DSC curves. Additionally, the phosphorylation *per se*

reduces β -structure formation [5], thus decreasing crystallinity and masking possible T_g by broadening distribution of relaxation times in the polymer.

Maximal MTX dehydration occurred at 91 °C, however this step was a part of a pre-treatment phase of DSC experiment (see section 3.2.7) and, therefore, is not seen during the recorded measurement. The thermal results and the characteristics peaks indicate that the drug used was of its tri-hydrate form [176]. MTX-derived pseudo-melting peak and the decomposition peaks shift to lower temperatures for pH 7.2-cast films. The shift of both pseudo-melting (\blacktriangledown) and recrystallization coupled to decomposition (\blacktriangledown) endotherms of MTX towards lower temperatures (175 \rightarrow 150 °C and 252 \rightarrow 240-250 °C; Figs. 3.3 and S3.5) suggests strong drug–polymer interaction [175]. Of special magnitude is MTX pseudo-melting endotherm observed in non-modified, neutral-cast fibroin (Figure S3.5, **A**), traversing other curves. The cause of such behavior is unknown and can't be explained on solely hydrophobicity basis, since the same film type, corresponding to acidic casting and thus considered more hydrophobic (Figure S3.5, **B**) shows no such profound peak. Much lesser evident is the thermal event, encountered for 15%-phosphorylated silk. More extensively modified matrixes of pH 7.2 show no MTX-derived events. The drug pseudo-melting peak, although weakly pronounced for pH 3.5-cast films (0% and 15%), is also shifted. This is the only peak type, clearly distinguishable for the acidic pH-cast materials (Figure S3.5). MTX decomposition-derived peaks are present for both discrete pH values at 0%-modified fibroin only. The described differences in DSC results, involved with various materials, could be attributed to the different aggregate state of both constituting proteins and MTX in the samples [175]. Additional phenomena [187], such as film thickness, inter-molecular mobility of chains within the polymer or its previous thermal history probably explain the example of out-of-trend DSC curve for 30% modified fibroin, acidic-cast (Figs. S3.4 and S3.5, **B**).

In vitro release profiling of MTX made it possible to affirm that the release process is somewhat more facilitated from the matrixes elaborated at acidic pH. The release exponent n values were not always consistent with the expected for a specific material type, for example, anomalous-type release for pH 7.2- and 3.5- casted and pH 6.2 PPE- or PBS- incubated, respectively; Figure 3.6, **B**. In that situation one would expect to obtain higher n , corresponding to (super) Case-II mechanism, especially in PPE-

assisted process. Yet, the actual inability to apply RP modeling on the PPE-mediated profiles for pH 8.0 incubated matrixes, both neutral- and acidic- cast, underlines a strong burst release phase that surpasses 60% of total drug amount, initially found in the fibroin. Thus, at optimum pH, PPE promotes the drug release from both major groups of materials. Moreover, for pH 3.5-cast films even at pH incubation of 6.2, in PPE-mediated process, n values surpass those of pH 7.2-cast films. Again, not all the n values were calculated, due to RP model restriction (but only those, corresponding to 60% and 0% modifications, last two columns on the right in Figure 3.6, **B**). That signifies a sizable burst effect upon initial MTX release. The burst is also seen at PBS incubation of pH 8.0 for 3.5-cast films (Figure 3.6, **A**). This phenomenon of elevated burst in acidified fibroin-derived materials needs explanation. Similarly to the reported findings [188, 189], increased migration of MTX during the drying of cast films may result in a non-homogeneous distribution of drug in the formed matrix and provoke a burst release. Another plausible cause for lesser MTX retention inside the acidified-cast silk matrixes is their increased (in comparison with neutral pH-cast matrixes) heterogeneity. Heterogeneity may result from formation of cracks or perforations during the device fabrication. Indeed, pH 3.5-casted materials were more brittle than their pH 7.2-casted counterparts. Examples of phenomena, when formulations are been made by solvent evaporation and an increased removal of the solvent causes elevated porosity, are known [190, 191]. All of the above considerations make the statement regarding super Case-II release (bearing release exponent $n > 1$) of MTX from the currently fabricated materials quite expected. Besides, super Case-II-controlled release was already observed for caffeine-loaded karaya gum hydrophilic matrixes [177], alprenolol-incorporated cellulose-derived tablets [192]; cross-linked chitosan membranes in aqueous media swelled in a super Case-II manner [193].

As for diffusion-related constants, both models show significant difference of the derived values for neutral solution-cast films, but not for acidic one. The two kinetic models used can be compared through their K_{RP} and K_H values, as neither K_{RP} nor K_H have obvious definition (although describing similar concepts). K_{RP} alternatively can be seen as an interaction parameter between a drug and the material harboring it [136]. Within each model, RP did not demonstrate differences among K_{RP} values of the films, yet statistical differences among K_H values of films, obtained by Higuchi model, seem to be more

discriminative. This may stem from the nature of calculations involved in both approaches. K_H parameter is given by fitting software directly, whilst K_{RP} is derived from n . Moreover, RP approach implies that only the profile data, obtained from 60% release of the initial content, may be included in calculations [13, 120, 136]. What does not hold for Higuchi model, where the full range of release values can be used.

Wilcoxon's matched pairs test showed that for neutral-cast materials K_{RP} - and K_H - derived values are significantly different. Based on t -test, Ritger–Peppas model reports no differences in K_{RP} values among films, yet Higuchi shows statistical differences among K_H values of films.

Finally, the indirect contact assay results support the observations that acidified solution-cast materials release the drug intensively, whereas neutral solution-derived do not. Importantly, a negative correlation between phosphorylated content and MTX release is evident for the acidified formulations. This underlines the importance of phosphorylation in disrupting β -sheet structures, as reported previously [5, 157], by creating a more favorable environment for MTX retention.

In summary, it can be concluded that our initial assumption for the enhanced MTX retention within a dense, acidified hydrophobic matrix of silk fibroin was not proved. We were not able to establish time-controlled release of the drug, although the term "time-controlled" itself is not precisely defined, and exists a distinction between burst release and short-term controlled release, observed for several systems [194]. In our case the statement that a *prolonged* time-controlled release was not established, will be more correct. According to the Biopharmaceutics Classification System (BCS), MTX falls in more than one category of compounds' solubility [181]: it can be highly or less soluble, depending on the experimental conditions. Indeed, MTX solubility mainly depends on the ionization of its α - and γ -carboxylic groups [195] ($pK_1 \approx 3.22$ and $pK_2 \approx 4.53$, respectively) [196] and slightly on the state of a basic pteridine moiety ($pK_3 \approx 5.62$) [196]. Hence, during casting solutions preparation, the partial aggregation of the added solubilized MTX to acidified silk fibroin solution occurred, corroborating previous observations of MTX precipitation as a function of pH [195]. Likely drug migration to the superficial layers of forming materials during their drying caused non-uniformity of its distribution. Thus, despite the increase of protein self-aggregation at acidic pH, it does not enhance the drug retention

inside the film matrix. Actually, a lesser polymer–drug association was obtained, though not because of decreased affinity of MTX to the fibroin, but resulting from heterogeneity of its final distribution in the films. Kinetic parameters, obtained throughout the current study, appoint on basic pH and PPE enzyme as factors, facilitating the drug release. It is of no surprise that increased ionization or matrix degradation promote MTX solubilization or the release from the films. However, with respect to PPE, the option to drive the MTX release under proteolysis is of questionable value, so far as significant burst effect occurred. If the designed material would possess a prolonged time-controlled release *per se*, PPE contribution to the process would probably be considered as beneficial. Future perspectives on enhancing phosphorylated silk-based films may include physical manipulations on the cast material, using lesser molecular weight fibroin as a source for downstream processing, or adding plasticizers like glycerol. The treatments mentioned above were found to increase dried films' plasticity [197], flexibility and water retention [198], or alter release rate of the incorporated compound from a film and the rate of film degradation [199]. Later, if the drug is to be added, it may experience different (desirably prolonged) release kinetics.

On the contrary, nearly neutral solution-casting produced materials with slower drug release. The explanation for descent density of those fabricated films and the following more uniform MTX incorporation, resulting in its slower dissipation, is quite reasonable. Several works reported a connection between elevated content of β -sheet crystals and the formation of high packing density in silk fibroin [200-203]. Crystallinity is directly related to β -sheet hydrophobic stacking and in the silk solution it is favored at dehydration [201], shear stress [204], heating [16], pH drop [16], among other modes. The conclusion for decreased density of pH 7.2-cast films stems from previous observations of decreased β -sheet amounts in phosphorylated fibroin by circular dichroism [5] and de-convolved FTIR spectra, reflecting on secondary structure analysis [157]. Moreover, being that none of the above treatments for crystallinity induction was done on neutral pH-cast films, they are considered to possess a less tight structure. Since the electrostatic interactions are considered to be mainly repulsive in both cases (Figures 3.1; S3.1 and S3.2), the matrix structure has a determinative effect on the drug retention.

Acknowledgements

The authors would like to acknowledge the support, granted by European NOVO Project, contract no. FP7-HEALTH 2011-two-stage 278402. This work was partially supported by FEDER through POFC—COMPETE and by national funds from FCT through the projects PEst-C/BIA/UI4050/2011 (CBMA). V.V. also wants to thank Dr. Cláudia Botelho for her helpful discussion and comments made during the critical reading of the manuscript.

Phosphorylated silk fibroin matrix for methotrexate release

S Supplementary material.

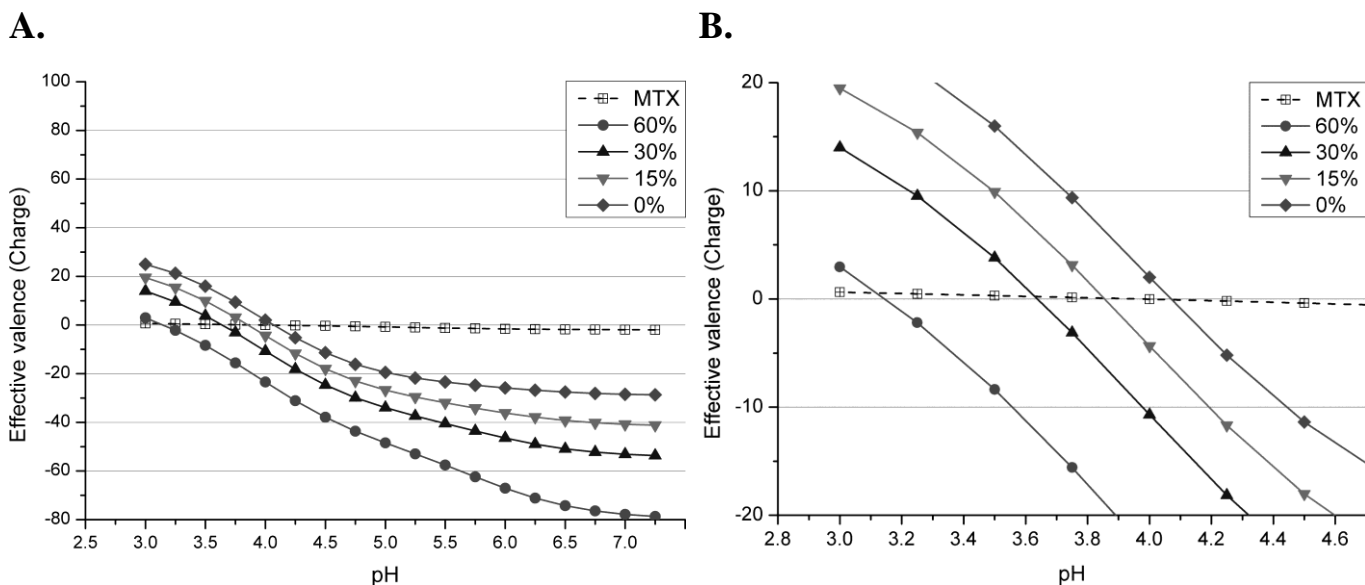


Figure S3.1. Theoretical estimation of silk fibroin and methotrexate (MTX) charges as pH function. **A.**, Full-scale representation. **B.**, Zoomed-in representation.

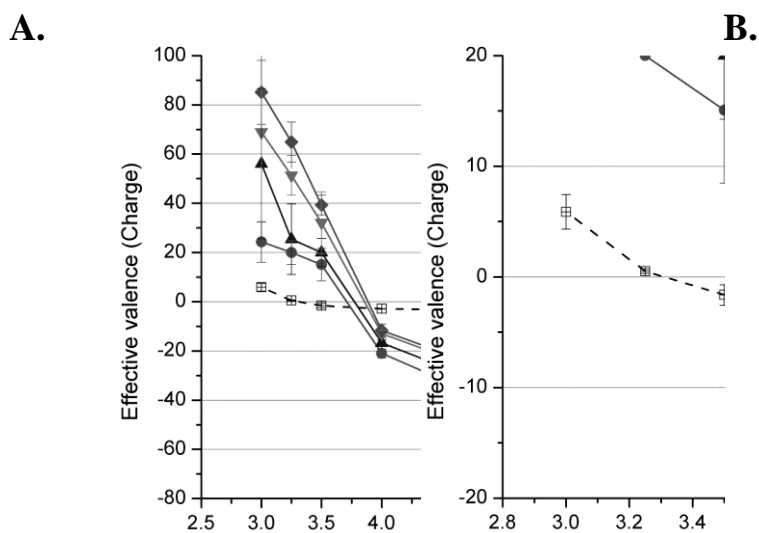


Figure S3.2. Experimental estimation of silk fibroin and MTX charges as pH function. **A.**, Full-scale representation. **B.**, Zoomed-in representation. Each line is a representative of three sample measurements.

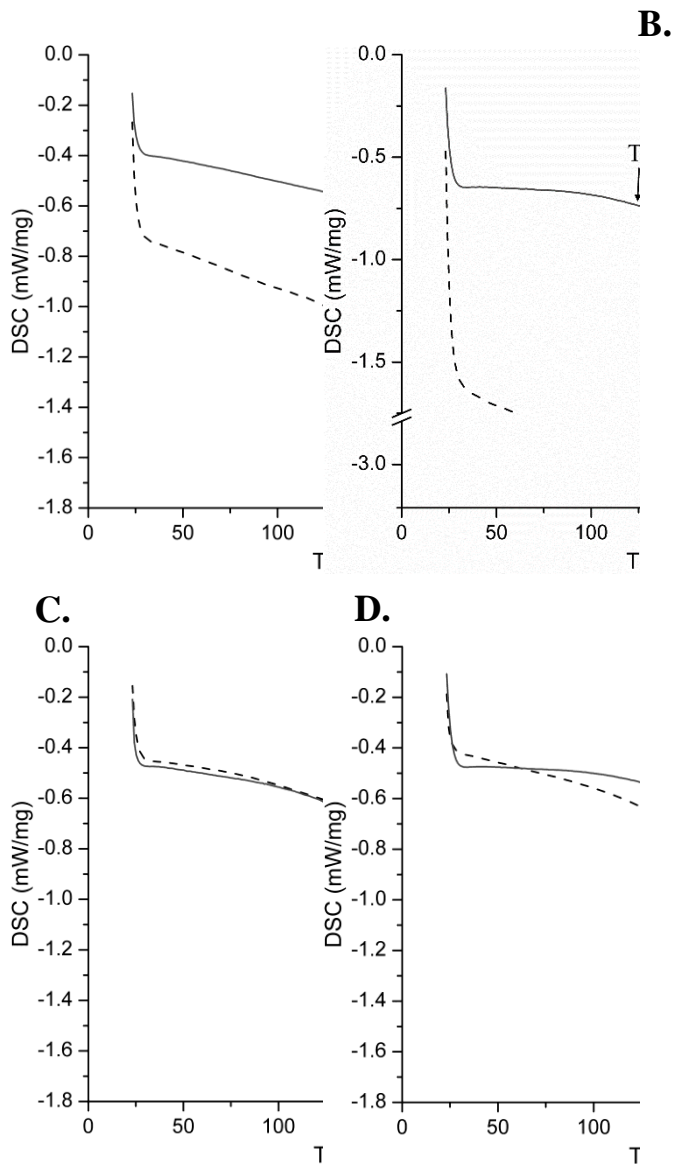


Figure S3.3. A pair-wise comparison of DSC curves corresponding to two main types (acidic- or neutral-pH cast) of elaborated materials. Different films of gradual phosphorylated content, without MTX are presented in panels **A.**, – **D.**, Where possible, the onset of glass transition temperature (T_g) and crystallization events (*) are indicated.

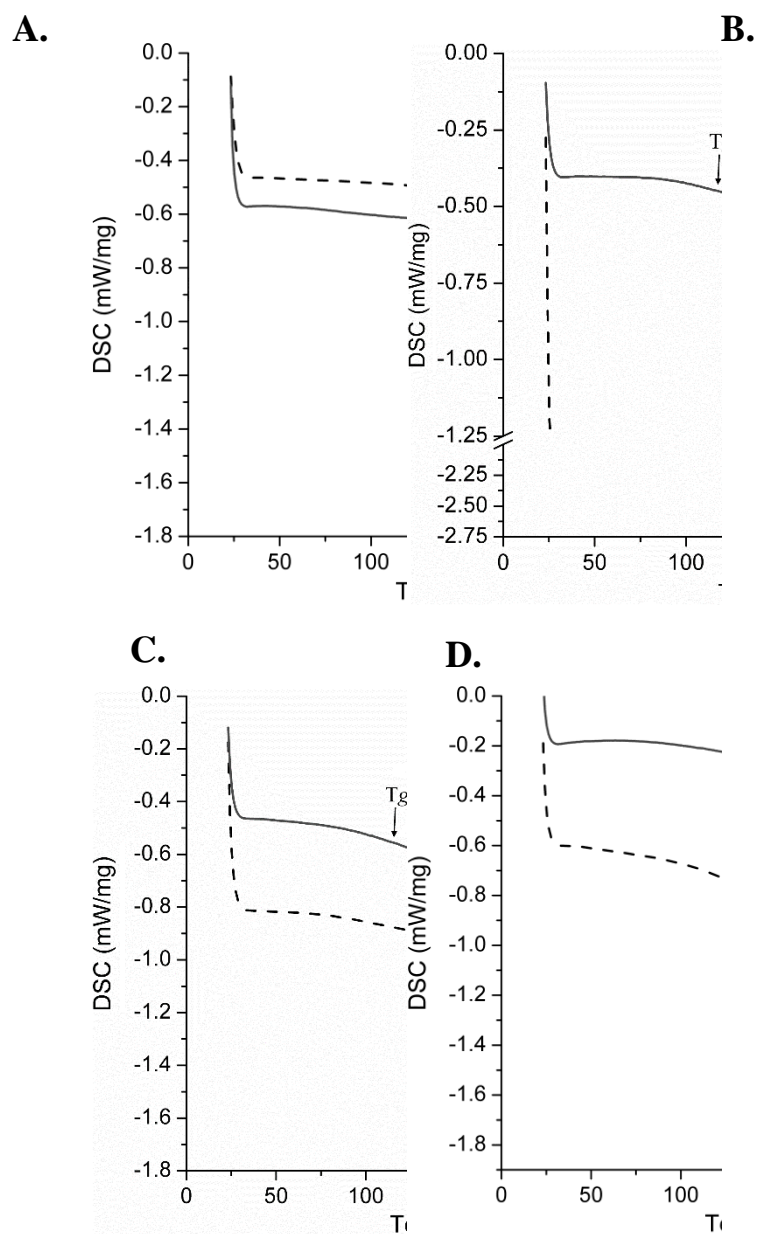


Figure S3.4. A pair-wise comparison of DSC curves corresponding to the two main types (acidic- or neutral- pH cast) of elaborated materials. Different films of gradual phosphorylated content, with MTX are presented in panels **A.**, – **D.**, Where possible, the onset of glass transition temperature (T_g) is indicated. Several thermal events, associated with MTX incorporation are marked with the corresponding left-directed arrows. \blacktriangledown – pseudo-melting; \blacktriangledown – recrystallization coupled to partial decomposition. In panel **B.**, due to graph scaling optimization, some of the curve of 30% type pH 3.5-cast material is truncated.

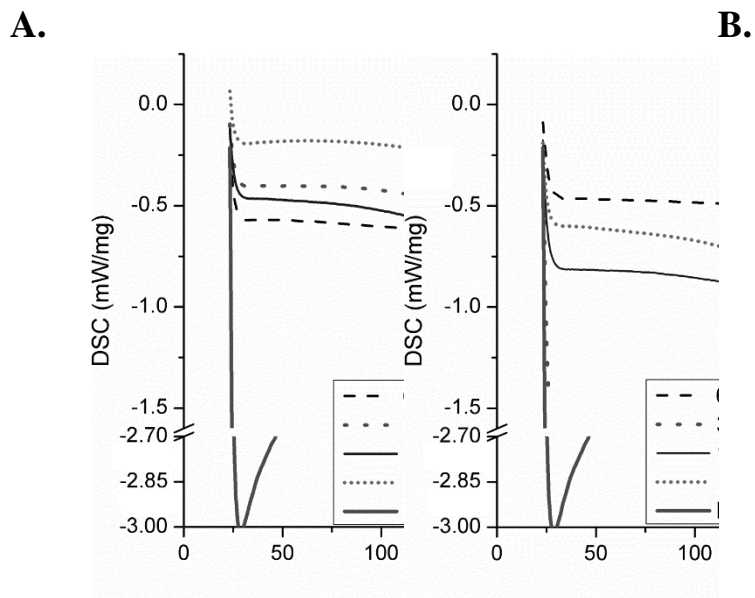


Figure S3.5. A group representation of DSC curves corresponding to the two main types (acidic- or neutral- pH cast) of elaborated materials, together with MTX only powder. Thermal events, occurring in the pure drug (right-directed arrows) and their presence in MTX-loaded matrixes (left-directed arrows) are shown. \blacktriangledown – pseudo-melting; \blacktriangledown – recrystallization coupled to partial decomposition. **A.**, Neutral- pH cast films. **B.**, Acidic- pH cast films. The aberrant 30% type pH 3.5-cast material, similarly to 60% does not show any MTX-derived thermal event. However, because of graph scaling optimization, it almost entirely falls within the Y-axis break range and is not seen.

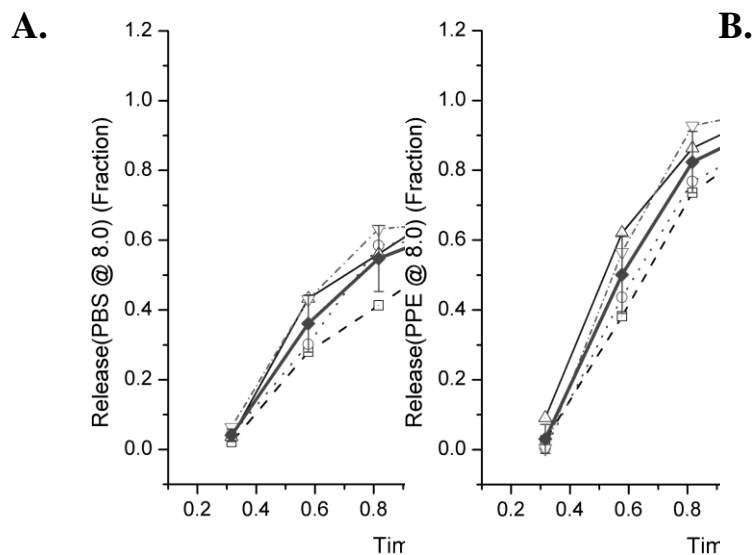
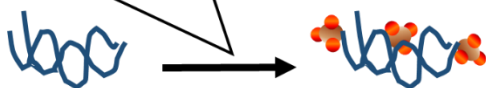
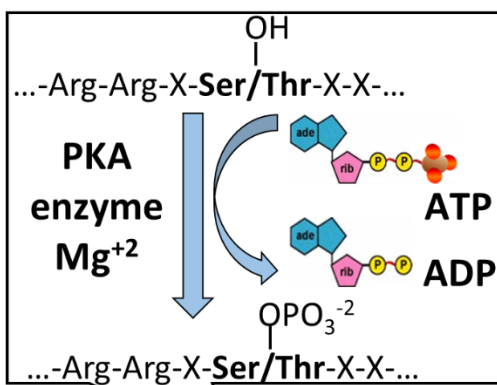
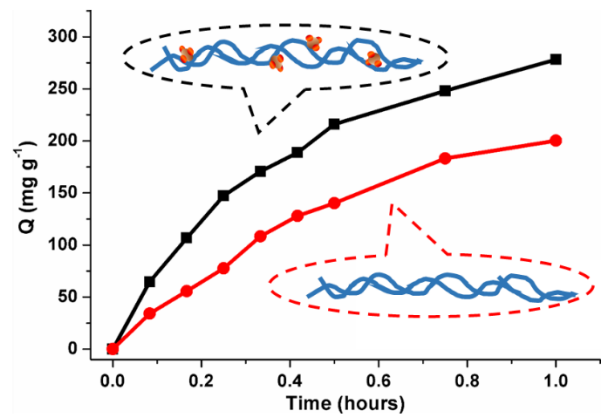


Figure S3.6. Representative examples of individual profiling curves of MTX release that served as a source for averaging. The bold averaged curves are presented with standard error bars. For simplicity, individual profiles for discrete material types of phosphorylation percentage are shown without error bars. **A.**, Neutral pH-cast materials, PBS-incubated at pH 8.0. **B.**, Acidic pH-cast materials, PPE-incubated at pH 8.0.

Chapter IV



In vitro Phosphorylation



Kinetic Outputs

Chapter IV

Enzymatic phosphorylation of hair keratin enhances fast adsorption of cationic moieties

Abstract

The current study examines human hair as adsorbent material for Methylene Blue (MB). The hair was subjected to chemical damage and subsequently phosphorylated by kinase for the first time, or left further unmodified. Phosphorylation was confirmed by NMR and DRIFT techniques. Hair adsorption capacity increased with increasing initial dye concentration and pH, but decreased with increasing temperature, indicating an exothermic process. Between two hair groups, regardless of the experiments performed, the phosphorylated group demonstrated higher affinity to the adsorbate. Moreover, phosphorylation induced a ≈ 1.5 times increase of adsorption capacity starting from the first 10 min for MB. In comparison to Freundlich and Dubinin–Radushkevich isotherm models, Langmuir isotherm fit empiric data the best way. A mean free energy of adsorption between 14–15 $\text{kJ}\cdot\text{mol}^{-1}$ for both hair types indicated a chemisorption process, occurring by ion exchange. Gibbs free energy calculations appointed on spontaneity of the dye uptake by the hair. The kinetic data were fit by a second-order model better, than by a first-order or intra-particle diffusion models. Reconstructed microscopic images depict distinct amounts of bound dye to the differently treated hair. The obtained findings suggest that enzymatic phosphorylation of keratins might have significant implications in hair shampooing and conditioning, where short application times of cationic components are of prime importance. The degree of affinity for the dye may be altered by enzymatically. Throughout the current work various important aspects, characterizing the adsorbent materials and governing the hair–dye interactions are been elucidated and thoroughly discussed.

This chapter is based on the following publication: **Vadim Volkov** and Artur Cavaco-Paulo, Enzymatic phosphorylation of hair keratin enhances fast adsorption of cationic moieties, *Biotechnology & Bioengineering*, submitted.

4.1. Introduction

Hard keratins found in human and animal hair, as well as nails, horns and feathers, are the basic building blocks of those complex morphological structures [51]. Apart of being a major target of an industry for cosmetic and care products [205, 206], keratin fibers are lately being reported as novel biocompatible materials in the areas of tissue engineering [207], wound dressings [208], surgical interventions [209] among others. Keratin and keratin-derived products may also be used as adsorbents for (toxic) pollutants [210-212]. For those numerous and different purposes keratin structure may be modified. Typically, the purely chemical alterations of keratin prevail upon the enzymatically-driven ones. However, several patents report on modification of keratin fibers using enzymes for applications such as the properties enhancement of harshly treated wool textiles [213], or for hair styling and coloring under mild conditions [78-80]. The usage of protein disulphide isomerase (PDI) enzyme for incorporation of functional molecules onto keratinous substrates was previously reported by our group [82, 214].

In vivo phosphorylation is considered an important post-translational modification of proteins. It affects intra- and inter- molecular interactions [105] and is stable under physiological conditions [106]. Specifically to keratins, phosphorylation and dephosphorylation affect the pool of its soluble molecules, deposited in granular aggregates and affect keratin interactions with other proteins [215]; and influence the organization of filaments [85]. The essential role of keratin remodeling by phosphorylation in living systems have been demonstrated through the observations of its different mutation and mis-expression experimental models [86]. The degree of phosphorylation may vary [216], and it is assumed to be carried out by several kinases: cAMP- and Ca²⁺/calmodulin- dependent kinases, protein kinase C [217]. Currently, no work on *in vitro* phosphorylation of hair tresses can be found.

Methylene Blue (MB) belongs to the family of thiazine dyes and is chemically a 3,7-bis(dimethylamino)phenothiazine-5-ium chloride. It is a cationic dye, widely used as colorant for a variety of materials, including the temporary coloration of hair-related structures [218]. Other chemical derivatives of MB are known, some of them are used as photo-inactivation agents for the molecules of biological significance (for example, viruses [219]).

Adsorption is a concentration change of a given substance between the boundaries of two phases as compared with the surrounding bulk phases [220]. Throughout years of research several consistent patterns of adsorption processes were described. For instance, it was shown that the adsorption of polyelectrolytes on solid surfaces is governed by many factors such as the nature of the solid surface, polyelectrolyte molecular structure, temperature and some others [221]. Furthermore, for the agricultural waste used as adsorbent, cationic dyes are known to possess high adsorption capacity, while anionic dyes typically have a lower one [222]. However, the underlying mechanisms of adsorption processes are usually complex because of structural and energetic heterogeneity of the surfaces that is common to a vast number of adsorbents routinely used [223]. Hence, extensive modelling is needed in many cases, in order to evaluate the adsorption mechanism pathways, to express the surface properties and capacities of adsorbents, and effectively construct the adsorption systems [224]. The heterogeneity of hair, whether physical and/or chemical, implies that the binding of applied adsorbents to its surface is expected to be more complex than that to homogeneous solid surfaces.

In the current work, a bleached human hair was used as adsorbent and the MB dye as adsorbate. Following the bleaching, the hair was optionally phosphorylated or left untreated. For the first time, *in vitro* phosphorylation of hair shafts was achieved by protein kinase A (PKA) with exogenously supplied ATP as a source of incoming phosphate group. Throughout the manuscript, the phosphorylated hair will also be referred to as a modified hair. Thus, two types of adsorbent material were obtained, the modified and the non-modified, both previously chemically damaged. Several adsorption/desorption studies were performed, aiming to check the feasibility of the elaborated sorption system. Acquired data were fit by different kinetic and thermodynamic models, and the arisen findings discussed.

4.2. Materials and methods

4.2.1. Materials

Human virgin hair of Caucasian origin was supplied by International Hair Importers & Products Inc. (USA) and used as provided. Methylene Blue dye was of Carlo Erba Reagents (Italy). Trizma® base,

NaOH, HCl, protein kinase A (Cat.nr. P5511) and Esperase® 8.0L protease (Cat.nr. P5860) were obtained from Sigma-Aldrich (Spain). All reagents were of analytical grade.

4.2.2. Preparation of (phospho-) keratin samples

Prior to phosphorylation, hair was subjected to 5 cycles of bleaching, similarly to the reported protocol [81]. During a separate cycle hair tresses were immersed in 12 wt% H₂O₂ in 0.1 M Na₂CO₃ pH 9.0 buffer at 50 °C for 1.5 hours. Bleaching solution was flashed after each cycle. Liquor-to-goods ratio was ≈101 (200mL solution for 2gr dry hair weight). Subsequently, bleached hair was thoroughly rinsed with distilled water, dried and stored at room temperature at 40-45% relative humidity. Prior to phosphorylation, the hair was pre-conditioned in PKA buffer for 1 hour; conditioning buffer was then replaced by a fresh one. Phosphorylation was carried out using PKA, as reported [157]. The reaction was terminated by the washings in ultra-pure water, samples were dried and stored as described previously. All of the above treatments were also performed on non-phosphorylated hair, with a single exception — no kinase enzyme was added to the reaction mixture.

4.2.3. Infra-red spectroscopic characterization of hair

Diffuse Reflectance Infrared Fourier Transform (DRIFT) analysis was performed on Spectrum 100 of Perkin Elmer Inc. (USA), equipped with diffuse reflectance sampling accessory. For the sampling of hair tresses, uncoated Si-C abrasive pads (Cat.nr. L1271021, Perkin Elmer) were used. The background was acquired with a clean pad. Data were collected from two independent measurements, each one was done in 64 rescan mode. The scan range was taken from 450 to 4000 cm⁻¹ with a resolution of 16 cm⁻¹. Spectral normalization was automatically performed by the software, Spectrum v6.3.5.0176 (Perkin Elmer).

4.2.4. Nuclear magnetic resonance spectroscopy of hair

NMR was performed on Bruker Avance III 400 MHz spectrometer (USA). ³¹P spectra were obtained at the frequency 162 MHz with the spinning rate of 20 RPM. ¹H decoupling was performed and 64K

data-points collected. For each sample, 20700-20900 transient scans were collected. External phosphoric acid was used to express the relativity of detected chemical shifts.

Hair samples of both types (non-phosphorylated and phosphorylated) were partially degraded with Esperase® 8.0L as following. 150 mg dry hair was incubated with 6 U protease at 50°C for 1 hour. The reaction buffer was 40 mM Tris-HCl, pH 9.4, devoid of any other salt. Proteinaceous debris were separated from the rest of solution by centrifugation and supernatant taken to NMR assay.

4.2.5. Methylene blue adsorption/desorption studies

Initially, dye stock solution was prepared, obtaining a final concentration of 2000 mg•L⁻¹. All the solutions of different MB concentrations and/or pH were prepared as described elsewhere [225]. Instead of water, 50 mM Tris-HCl buffer was used. The adsorption/desorption tests were performed in batch conditions by shaking the adsorbate at 40 RPM in 10 mL incubation solutions, at 20°C, unless other temperature was indicated. All the adsorption experiments were performed using a constant adsorbent dosage of 1.1, *i.e.* (11 mg dry hair mass)/(10 mL MB dye starter solution). For desorption examinations, the dye-loaded hair was previously and gently washed in 10mL ultra-pure water for 1 minute to remove any un-adsorbed dye. Discrete MB concentrations were determined spectrophotometrically by reading the solutions against standard curves at 665nm.

The adsorption capacities Q_t , Q_{equ} and Q_{max} (mg•g⁻¹) and the percentage removal efficiency R (%) were calculated as previously described [225, 226]:

$$Q = \frac{([MB]_{init} - [MB]_{fin})V}{m} \quad (4.1) \quad \text{and} \quad R = \frac{desorbed}{loaded} \times 100\% \quad (4.2)$$

where $[MB]_{init}$ and $[MB]_{fin}$ are initial and final dye concentrations (mg•mL⁻¹), V is MB solutions volume (mL), m is dry hair mass (g). *Desorbed* and *loaded* are the amounts of MB dye (mg), removed or deposited by adsorption/desorption experiments. All the assays were carried out in duplicate with double sampling at each time point; mean values were reported.

4.2.6. Acquired data processing

Data that needed fitting were exported to OriginPro software, v8.5.0 by OriginLab Corporation (USA). Linear fit was performed by using the appropriate routine with default software settings. DRIFT-derived spectra were smoothed in OriginPro software by Adjacent-Average method, without weighting. Filter window size of 15 points was used. Empiric data were fit by or substituted into several equations, presented below (Table 4.1):

Table 4.1. Different model equations used in the current work.

Model type applied/equation used	Equation (in linearized form, if necessary)
Kinetic	Pseudo-first order $\log(Q_{equ} - Q_t) = \log Q_{equ} - \frac{k_1 t}{2.303}$ (4.3)
	Pseudo-second order $\frac{t}{Q_t} = \frac{1}{k_2 Q_{equ}^2} + \frac{t}{Q_{equ}}$ (4.4)
	Intra-particle $Q_t = k_i t^{1/2} + C$ (4.5)
Isothermal	Langmuir $\frac{[MB]_{equ}}{Q_{equ}} = \frac{1}{Q_{max}} [MB]_{equ} + \frac{1}{K_L Q_{max}}$ (4.6)
	Freundlich $\ln Q_{equ} = \ln k_f + \frac{1}{n} \ln [MB]_{equ}$ (4.7)
	Dubinin-Radushkevich $\ln Q_{equ} = \ln Q_{max} - \beta \varepsilon^2$ (4.8)
van't Hoff thermodynamics	$\ln\left(\frac{Q_{equ}}{[MB]_{equ}}\right) = -\frac{\Delta H}{RT} + \frac{\Delta S}{R}$ (4.9)
Gibbs free energy change	$\Delta G = -R_B T \ln\left(\frac{Q_{equ}}{[MB]_{equ}}\right)$ (4.10)

The equations were taken from the literature [225, 226]. k_1 (min^{-1}), k_2 ($\text{g}\cdot\text{mg}^{-1}\cdot\text{min}^{-1}$) and k_i ($\text{g}\cdot\text{mg}^{-1}\cdot\text{min}^{-1/2}$) are the rate constants of pseudo-first order, pseudo-second order and intra-particle diffusion, respectively. C ($\text{mg}\cdot\text{g}^{-1}$) is a constant. K_L ($\text{L}\cdot\text{mg}^{-1}$) and k_f ($(\text{mg}\cdot\text{g}^{-1}) (\text{L}\cdot\text{mg}^{-1})^{1/n}$) are effective dissociation and adsorption capacity constants, respectively. β ($\text{mol}^2\cdot\text{kJ}^{-2}$) and ε are the constant related to the mean free energy of adsorption and the Polanyi potential [220], respectively. n is a dimensionless adsorption driving force-related constant. R_B is a Boltzmann molar gas constant ($8.314 \text{ J}\cdot\text{mol}^{-1}\cdot\text{K}^{-1}$), T is an absolute temperature (K).

4.2.7. Sample preparation for confocal microscopy, image acquisition and 3D modelling

Separate hair shafts were embedded in epoxy cold mounting system (Cat. nr. 40200029, Stuers, UK) according to the supplier's protocol, and the system was left to cure. Obtained solid material was polished and subsequently sliced by a blade microtome machine, producing slices of 15 μm thickness.

The sliced straps, containing hair, were mounted on glass slides and inspected on Olympus BX61/FV1000 confocal system, operating under Olympus Fluoview v4.0 software (Olympus Corp., Japan). 635 nm wavelength diode laser, operating at 2% of power, was used to excite the dye; emission was collected through BA 655-755 nm band-pass filter. PLAPONSC 60x oil objective with numerical aperture of 1.4 was utilized. During the image acquisition, depending on the fluorescent output, the High Voltage and PMT Gain parameters were manually adjusted until the appearance of first signs of saturation or a noisy background. Constant Offset parameter of 10 was used.

Acquired 3-dimensional (3D) images were loaded into Imaris® v.7.0.0 software (Bitplane AG, Switzerland) and the corresponding 3D models were built. For the sites of major dye affinity, background subtraction with thresholding of 1.035 μm was performed, the rest of the building algorithm parameters were set to automatic. For the bulk hair shaft volume visualization, automatic smoothing was performed.

4.3. Results

4.3.1. Evidence to the phosphorylation of hair keratin

To confirm the enzymatically-driven phosphate incorporation in chemically damaged hair, two methods were employed. Since regular ATR-FTIR was not able to detect phosphate-related vibrational peaks on modified keratin during preliminary examinations made on Merino wool (Figure S4.1), DRIFT was performed. Figure 4.1, **A** depicts IR spectra of differently treated hair in the region of interest (ROI) of 1800-400 cm^{-1} . First to be mentioned are the common peaks of Amide I, II and III (1650, 1540 and 1200 cm^{-1} , respectively) [227]. Two additional bands [227], also shared by all hair types, are the somewhat subtle peak from aromatic and imidazole rings of Trp, His and Pro (1450 cm^{-1}); and the sharply appearing Thr/Ser C–O stretching vibrations (1050 cm^{-1}). Interestingly, the C–O vibration was hardly observed for the virgin hair, what may signify that its intact outer-layers together with lipid coating of 18-methyleicosanoic acid [228] (18-MEA) shield inner structures from IR irradiation. Finally, a bimodal peak at 830/800 cm^{-1} is observed solely for the phosphorylated hair. In-phase P–O–C stretching vibrations can produce such a peak ([229] or refer to triethyl phosphate IR spectrum available

[online](#)). The abnormal inverted peak at 980 cm^{-1} is most likely an artefact of *Restrahlen* reflection of the abraded hair samples [230].

To further confirm the existence of phosphate group introduced into keratin, NMR of differently treated and degraded hair shafts was performed (Figure 4.1C). From the Figure 4.1B (top) it is seen that non-phosphorylated hair peptides showed only a basal phosphate-related peak, whilst kinase-reacted hair indicated a pronounced peak. The very weak phospho-peak of non-phosphorylated keratin may be attributed to some basal level of phosphorylation, naturally present [231]. Taking into account the number of scans, required for the peaks in Figure 4.1B to appear (section 4.2.4) and the sensitivity of the equipment (Figure S4.2), the phosphate found within the fibers is considered to be at μ -molar amounts.

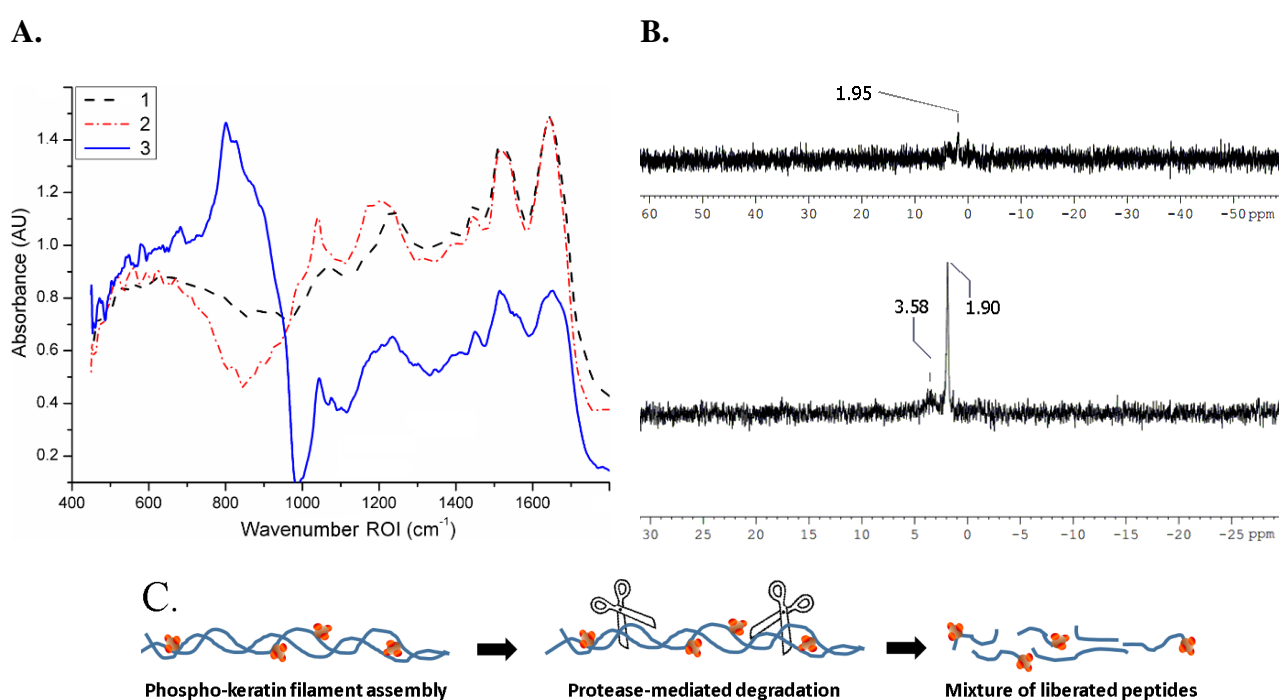


Figure 4.1. Experimental evidence of hair keratin phosphorylation. **A.**, DRIFT spectra of hair dust, obtained from its outermost layers. 1 – virgin hair, 2 – chemically damaged (bleached) hair, 3 – bleached and subsequently phosphorylated hair. **B.**, NMR spectra of keratin peptides, liberated by protease-mediated hair degradation. Top – bleached hair only, bottom – bleached and subsequently phosphorylated hair. **C.**, schematic representation of protocol,  employed for **B.**  designates a phospho-group.

4.3.2. Preliminary adsorption studies. Calculation of hair adsorption capacity

At first, the estimation of MB starting concentration(s) that will result in maximal adsorption capacity (Q_{\max}), along with Q_{\max} calculation were done. The results for different Q_t values are depicted in Figure 4.2. For both hair treatments, Q_t increases as the MB concentration ($[\text{MB}]_{\text{init}}$) in starter solution

increases, until an equilibrium, seen as graphs' plateau, is reached. It is evident that phospho-hair adsorb more of the dye, than the non-phospho-hair. Moreover, $[MB]_{init}$ for two hair types are 0.57 and 0.52 $mg \cdot mL^{-1}$ and Q values are 343 and 304 $mg \cdot g^{-1}$ for the phosphorylated and non-phosphorylated samples, respectively.

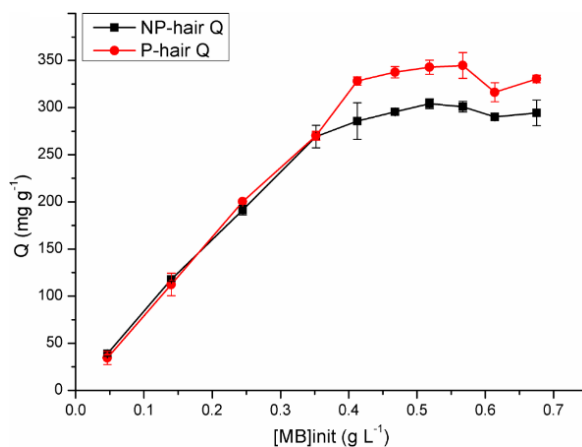


Figure 4.2. Determination of maximal adsorption capacity (Q_{max}) for the hair samples of two types. Hair was incubated in MB solutions of varying initial concentration, $[MB]_{init}$ and Q_{max} was assessed as described. NP- and P- designate the non-modified or enzymatically modified hair.

4.3.3. Kinetic, modelling and mechanistic aspects of MB adsorption

Once the best $[MB]_{init}$ for both hair types were known, it was possible to conduct extended kinetic investigations of the dye binding. Hair samples were incubated at 20°C for 24 hours and adsorption progress frequently monitored during the first 3.5 hours of experiment. The last time point collected was at 24th hour. Experimental outcome is presented in Figure 4.3. Since the $[MB]_{init}$ differs for phospho- and non-phospho- hair, there was a need to incubate both samples with two different dye starter concentrations. Again it is clear that keratin with additionally incorporated phosphate demonstrates better dye uptake. The differences in Q_t values within each group (modified and non-modified) stem from the different $[MB]_{init}$ in the incubation solutions. So that when the hair has some specific (and constant, for a particular treatment) adsorption capacity and different $[MB]_{init}$ are applied, the variation of remaining in the solution dye results in the variation of calculated Q_t .

To gain additional insights on the dye–hair interaction, several models were applied to empirically acquired data. Namely: the pseudo-first order (PFO), pseudo-second order (PSO) and intra-particle diffusion models. Empirical data points with matching fitted curves are presented in Figure S4.3, calculated kinetic values given in Table 4.2 and the corresponding equations appear in Table 4.1. Based on the similarity of Q_{\max} and Q_{equ} , as well as on the values of adjusted coefficient of determination \bar{R}^2 it can be concluded that the PSO model describes dye uptake kinetics the best way. What means that the uptake is dependent on both dye concentration and availability of binding sites in the adsorbent. Moreover, the values of constant C indicate additional factors [232], such as boundary layer thickness and boundary layer diffusion that also govern the mass-transfer of MB from solution to the hair adsorbent. The current findings on adsorption rate and on additional phenomena, arising from the intra-particle model, corroborate the previously reported conclusions for adsorption tests in various systems [225, 226, 232, 233].

The reaction of adsorption is commonly characterized by Langmuir and Freundlich isotherms. In addition, other isotherm models may be applied, depending on the need. As such, Dubinin-Radushkevich (D–R) isotherm serves the answer for qualitative evaluation of adsorption mechanism with a particular energy distribution onto a heterogeneous, porous surface. In the current work all of the aforementioned isotherm models were used [234], their linearized equations are given in Table 4.1. Langmuir model presumes that adsorption occurs at specific and homogenous sites within the adsorbent, adsorbate forms a monolayer covering the adsorbent; Freundlich model assumes that exists some heterogeneous adsorption surface with sites of different energies of adsorption and non-equal availability. Data, obtained from Q_{\max} determination experiments, were fitted by the chosen models. Resulting fits are presented in Figure S4.4 and the calculated parameters, corresponding to each isotherm model are given as Table 4.3. It can be seen that Langmuir isotherm describes the dye adsorption best, similarly to previous works [225, 226]. Yet this is not the case of dimethylpabamidopropyl laurdimonium tosylate (DDABDT) adsorption on delipided human hair. It was shown for a cationic surfactant, DDABDT, that Freundlich model fits the observed process in a better way [233]. In the latter case the molecular structures of both adsorbate (a long-chain alkylated

quaternary ammonium compound) and a hair adsorbent (virtually intact fibrous framework, except for 18-MEA removal) reflect on binding mechanisms that differ from other systems mentioned. Freundlich model was also found to be the most appropriate for description of MB removal from aqueous solution by silkworm exuviae [235]. The degree of surface heterogeneity $1/n$, known from slope of a curve by plotting $\ln Q_{equ}$ versus $\ln[MB]_{equ}$, indicates more heterogeneous surface if inequality $1/n \ll 1$ holds and the factor $1/n$ decreases [236]. Therefore it is worth noticing that the currently reported $1/n$ ($1/n_{NP\ hair} = 0.2474$ and $1/n_{P\ hair} = 0.2704$) is roughly twice smaller than the one presented previously [235] (for the closest temperature available: $1/n = 0.5370$). Thus the heterogeneity of chemically damaged hair is higher than that of silkworm exuviae, yet phosphorylation seems to decrease this property.

By using Langmuir model it can be assessed whether a given adsorption system is favorable or not. For that, a dimensionless constant, R_L , is defined as following:

$$R_L = \frac{1}{1 + K_L[MB]_{init}} \quad (4.11)$$

R_L indicates irreversible ($R_L = 0$), favorable ($0 < R_L < 1$), linear ($R_L = 1$) or unfavorable ($R_L > 1$) adsorption. Both modified and non-modified hair exhibited R_L values in the range: $3.00 \cdot 10^{-5} < R_L < 4.46 \cdot 10^{-4}$ (Figure S4.5), thus indicating a favorable process.

Similar conclusion can be drawn from Freundlich model-derived parameter n . n falling within the value range of 2–10 represents good, 1–2 moderately difficult, and less than 1 poor sorption [226]; therefore the values appearing in Table 4.3 point on a favorable sorption.

Table 4.3. Parameters of the isotherms, applied on MB dye adsorption curves for different hair types.

Model applied	Hair type	Types of isothermal parameters and their values		\bar{R}^2
Langmuir		Q_{max} (mg·g ⁻¹)	K_L (L·mg ⁻¹)	
	NP	322.580	$49.301 \cdot 10^3$	0.9868
	P	374.531	$46.675 \cdot 10^3$	0.9647
Freundlich		n	k_f (mg·g ⁻¹) (L·mg ⁻¹) ^{1/n}	
	NP	4.041	2275.602	0.716
	P	3.698	3387.677	0.8296

Dubinin- Radushkevich	Q_{\max} (mg·g ⁻¹)		E (kJ·mol ⁻¹)	
	NP	729.894	14.974	0.7669
P	976.72	14.315	0.8506	

Isothermal models for MB adsorption with the corresponding indicative constants. E is the mean energy of adsorption. NP- and P- designate the non-modified or enzymatically modified hair, the digits coming after indicate specific $[MB]_{\text{limit}}$. The designations of other parameters are as stated for Table 4.1.

Table 4.2. Estimated kinetic parameters of MB dye adsorption on different hair types.

Model applied	Hair and incubation types	Experimentally determined parameters		Kinetic parameters, calculated from modelling		
		[MB] _{init} (mg·mL ⁻¹)	Q _{max} (mg·g ⁻¹)	Q _{equ} (mg·g ⁻¹)	k ₁ (min ⁻¹)	R ²
Pseudo-first order	P-0.57	0.57	343	238.979	0.0159	0.9638
	P-0.52			220.206	0.0128	0.9066
	NP-0.52	0.52	304	198.458	0.0131	0.9381
	NP-0.57			206.262	0.0142	0.9844
Pseudo-second order	P-0.57	0.57	343	355.871	1.504*10 ⁻⁴	0.9924
	P-0.52			325.732	1.211*10 ⁻⁴	0.9827
	NP-0.52	0.52	304	283.286	1.239*10 ⁻⁴	0.9795
	NP-0.57			273.224	1.067*10 ⁻⁴	0.9747
Intra-particle diffusion	P-0.57	0.57	343	18.654	20.715	0.8746
	P-0.52			17.144	19.937	0.8845
	NP-0.52	0.52	304	13.548	17.318	0.9026
	NP-0.57			10.340	16.573	0.9359

The table represents two general types of parameters, whether obtained empirically ([MB]_{init} and Q_{max}) or theoretically (Q_{equ}, k₁, k₂, k_i and C). NP- and P- designate the non-modified or enzymatically modified hair, the digits coming after indicate specific [MB]_{init}. The designations of other parameters are as stated for Table 4.1.

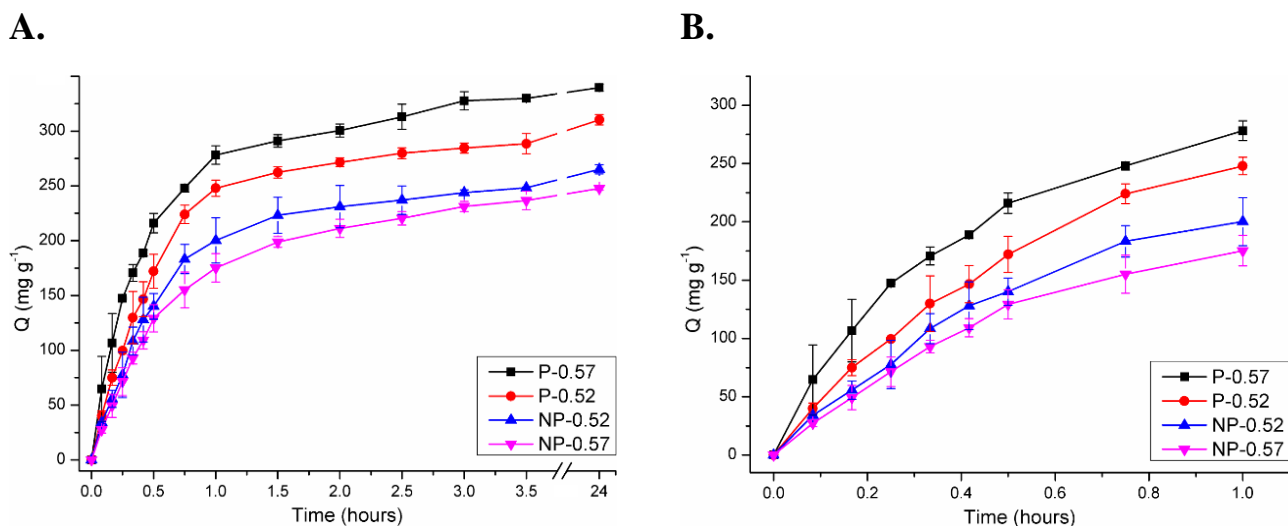


Figure 4.3. Time-lapse examination of MB adsorption onto differently treated hair. NP- and P- designate the non-modified or enzymatically modified hair, the digits coming after indicate specific $[MB]_{init}$. **A.**, Full-scale representation. **B.**, Hi-resolution representation of the first hour of incubation.

4.3.4. Thermodynamic aspects of MB adsorption

To gain additional important insights into dye–hair interactions D–R isotherm model was used. D–R isotherm, although being not the best model to describe our binding system, offers assessment of adsorption energy by the calculation of related constant β . The constant is presenting in the linearized equation of this isotherm (Table 4.1). It can be obtained from the slope of a curve by plotting $\ln Q_{equ}$ versus ε^2 . In turn, ε is equal to $RT \ln(1 + [MB]_{equ}^{-1})$. So that β enables the researcher to calculate the mean energy of adsorption E as defined [237]: $E = (2\beta)^{-0.5}$. Having $\beta_{NP \text{ hair}} = 0.00223$ and $\beta_P \text{ hair} = 0.00244 \text{ mol}^2 \cdot \text{kJ}^{-2}$, the resulting energy is obtained in the range of $14 < E < 15 \text{ kJ} \cdot \text{mol}^{-1}$ for both hair types, indicating an ion-exchange mechanism of dye uptake [238]. In a particular case, energy was needed to transfer the dye ions from the solution to the surface of two different adsorbents, yet for the phosphorylated hair this energy uptake was somewhat lower. This fact reflects the elevated favorability of phosphorylated hair as a material for MB adsorption.

In parallel, the changes in adsorption enthalpy ΔH , entropy ΔS and Gibbs free energy ΔG were calculated using the corresponding equations from Table 4.1. ΔH , ΔS and ΔG are presented in Table 4.4. It can be seen that dye adsorption was exothermic in nature and during this process the entropy slightly increased. The increase in entropy was more prominent for the non-modified hair. Since negative ΔG

values were obtained for all conditions examined, the adsorbate uptake was thermodynamically favorable. Due to high similarity of ΔG values between both dye concentrations for a specific material at discrete temperature, they were averaged and the mean resulting values $\bar{x} \Delta G$ were reported with a standard deviation. Owing to the exothermic nature of MB uptake, a trend of decreasing Q with incubation temperature augmentation was observed (Figure 4.4, **A**).

The thermodynamic behavior of our system can be viewed in the context of similar studies. Specifically for MB as adsorbate and keratin (or keratin-derived material) as adsorbent at least two papers exist. Both report on MB uptake as an exothermic process. One study estimates E of similar magnitude [225], the other describes spontaneous adsorption of the dye accompanied by significant decrease in ΔS [239]. The adsorption of haematoxylin (chemically similar to MB) onto yak hair was exothermic, spontaneity and the increase of entropy were reported for temperatures of 30°C and above [240]. Other systems for MB removal from industrial effluents are generally endothermic, spontaneous and cause ΔS elevation during the dye uptake [235, 241-243].

The ultimate factor to be elucidated was the pH of the MB incubation solution. In our experiments higher values of Q were observed with increased pH (Figure 4.4, **B**). As a cationic dye, MB tends to bind more easily to a negatively charged surface, whose electrostatic properties, in turn, depend on pH. All the conditions checked, except for P-0.57, showed moderately increasing adsorption as pH increments from 4.0 to 7.0; and after the neutral pH is passed Q rises abruptly. This is in line with earlier recorded data of MB adsorption onto several bio-sorbents [225, 235, 239, 241].

Table 4.4. Thermodynamic parameters of the MB dye adsorption onto different hair types.

Hair type and [MB]	van't Hoff equation-derived			$\bar{x} \Delta G$ at chosen temperature (kJ·mol ⁻¹)			
	ΔH (kJ·mol ⁻¹)	ΔS (J·mol ⁻¹)	R ²	20 °C	30 °C	40 °C	50 °C
P-0.57	-29.106	19.991	0.9882	-35.043 ±	-35.080 ±	-35.345 ±	-35.930
P-0.52	-24.050	36.967	0.9106	0.079	0.016	0.200	± 0.377
NP-0.52	-21.206	43.903	0.9665	-33.741 ±	-33.926 ±	-34.400 ±	-35.066
NP-0.57	-20.347	43.803	0.9573	0.616	0.655	0.612	± 0.631

Calculated values of enthalpy ΔH , entropy ΔS and Gibbs free energy ΔG . NP- and P- designate the non-modified or enzymatically modified hair, the digits coming after indicate specific $[\text{MB}]_{\text{init}}$. ΔG values are reported as averaged of two different $[\text{MB}]_{\text{init}}$ for the same material, with standard deviation.

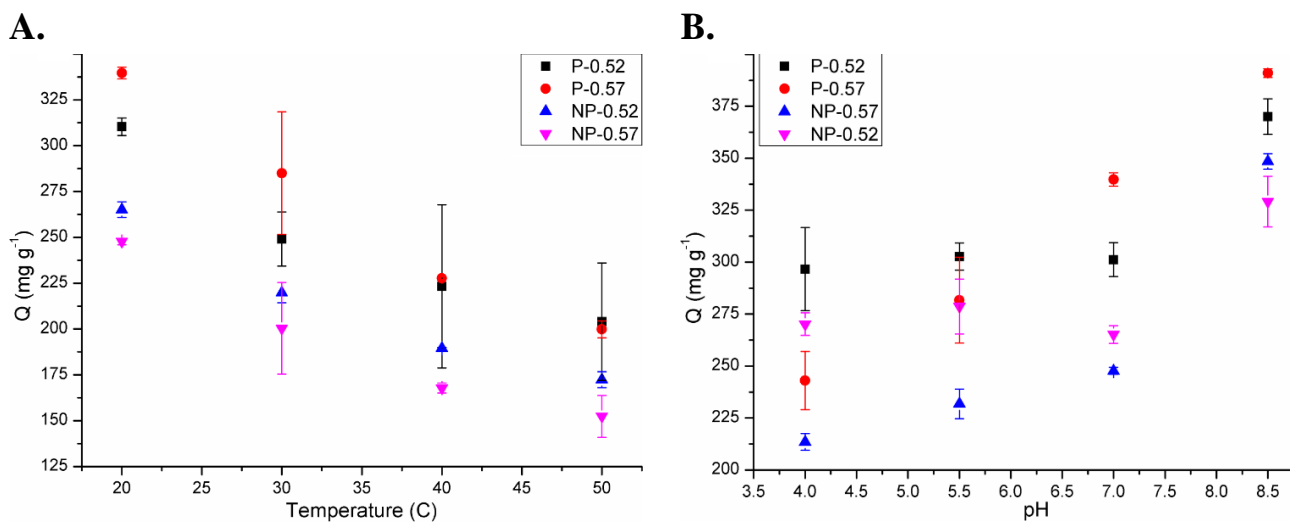


Figure 4.4. Additional factors of dye–hair association, examined in the current study. NP- and P- designate the non-modified or enzymatically modified hair, the digits coming after indicate specific $[MB]_{init}$. **A.**, Temperature-dependent adsorption. **B.**, pH-dependent adsorption.

4.3.5. 3D visualization of the hair-bound dye

It was of our interest to check if the images of differently bound dye onto various adsorbents can be obtained. For that, modified and non-modified dried hair shafts were incubated for 1 minute in $0.025 \text{ g}\cdot\text{L}^{-1}$ MB-containing buffer, fixed with epoxy resin and further processed (section 4.2.7). The short immersion time allowed for the dye binding preferably to the sites of highest affinity (whether phospho-sites or any others of similar binding capacity). Resulting images are presented in Figure 4.5.

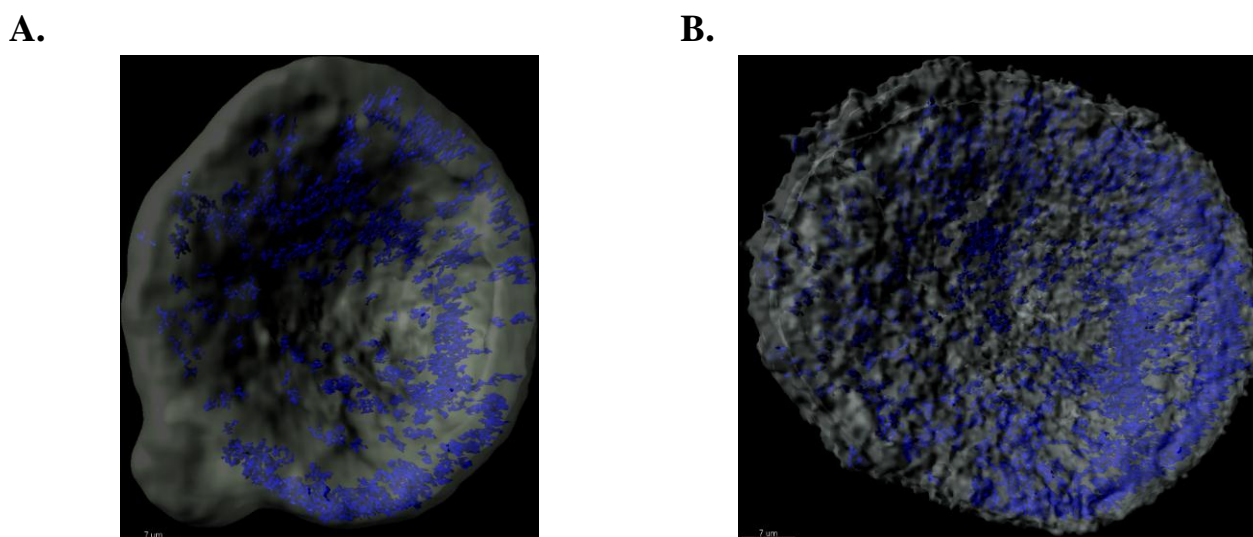


Figure 4.5. A view from the top of artificially colored 3D visualization of the sites of highest dye affinity (dark-blue) and the bulk hair adsorbent volume (light-gray). **A.**, non-modified adsorbent. **B.**, phospho-modified adsorbent. Scale bar, $7 \mu\text{m}$

It can be seen that the modified hair was able to adsorb more dye. Moreover, the calculated volumetric ratios for both hair types: $V_{dye-bound\ hair}/V_{total\ hair}$, reported by Imaris® program, are 0.0225 and 0.0317 for a non-phosphorylated and phosphorylated material, respectively. These values indicate a 29.1% increase in the specific dye binding sites as a result of phosphorylation.

4.3.6. Desorption studies of MB dye

Since the main scope of the current work was elucidation of mechanisms governing the MB uptake by the human hair-based adsorbent, only qualitative studies for the dye desorption were performed.

Time-lapse examination of desorption process was done as follows. MB-loaded samples were incubated at 20°C for 24 hours and adsorption progress frequently monitored during the first 3.5 hours. Resulting removal efficiencies R for various conditions are shown in Figure 4.6. As opposed to the tendency of Q to grow with phosphorylation presence, so R increases with its absence. MB that is bound non-specifically to the hair shafts is thought to be the most contributing factor for higher R values, seen both for NP-0.57 and P-0.57 conditions. It makes sense that the modified adsorbent P-0.57 possesses higher affinity for the dye, hence its calculated R is smaller.

Temperature- and pH- dependent examinations of MB desorption revealed that it is an endothermic process and disfavored at basic pH values (Figure 4.7). First observation contradicts the previously reported conclusion made for keratin-derived nanofibrous membranes [225], however it concurs with the study done on sheep wool as adsorbent [239]. Thus the result currently obtained is a plausible one, since our system physically resembles more the system of Khan *et. al.* [239], *i.e.* wool fibers and not electrospun membranes. Second observation contradicts the previously reported one as well [225], probably because higher amount of negatively charged groups *per se* and their further enhancement by a rising pH.

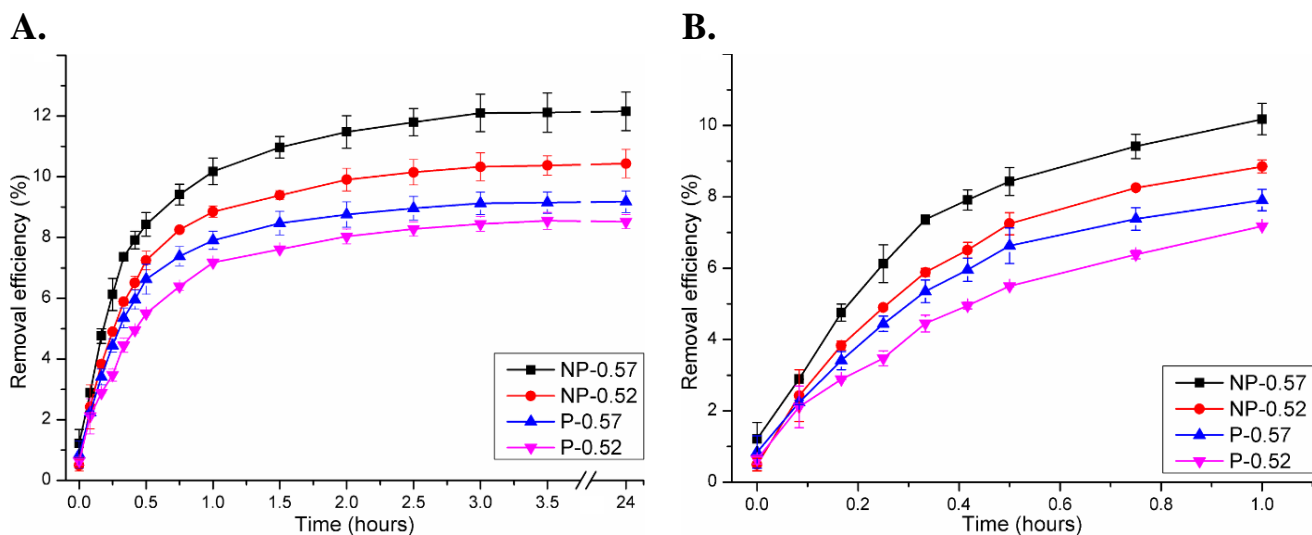


Figure 4.6. Time-lapse examination of MB desorption onto differently treated hair. NP- and P- designate the non-modified or enzymatically modified hair, the digits coming after indicate specific $[MB]_{init}$. **A.**, Full-scale representation. **B.**, Hi-resolution representation of the first hour of incubation.

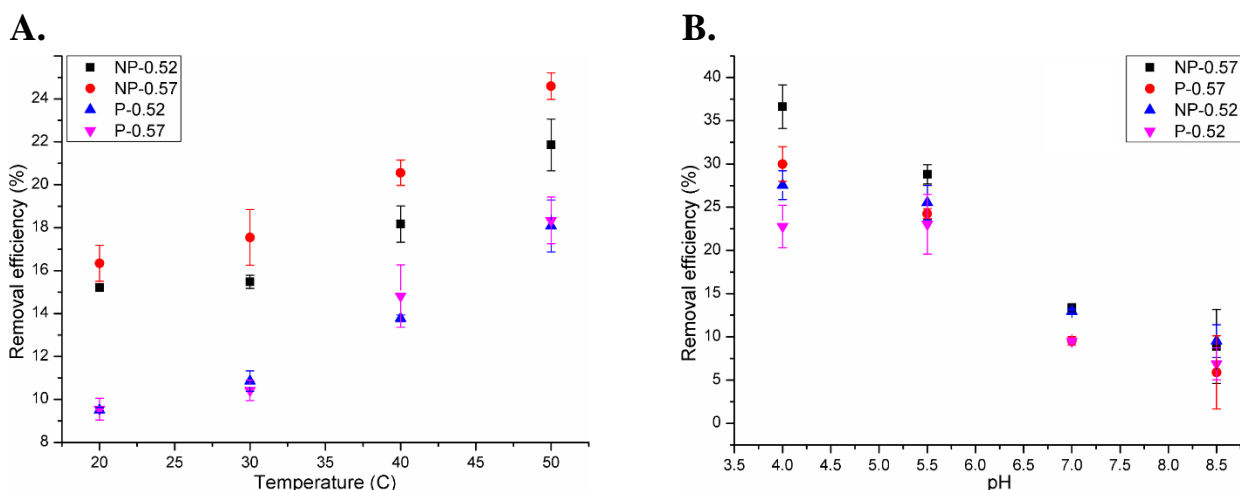


Figure 4.7. MB desorption experiments from a differently treated hair. NP- and P- designate the non-modified or enzymatically modified hair, the digits coming after indicate specific $[MB]_{init}$. **A.**, Temperature-dependent desorption. **B.**, pH-dependent desorption.

4.4. Discussion

The current work represents a trial of comprehensive description and explanation of the mechanisms, controlling the cationic (basic) dye adsorption onto differently treated human hair. Two major facts coerced us to conduct the study. First, keratinous waste was shown as one of the promising low-cost adsorbents for various pollutants. Second, keratin and its derived products are widely used in cosmetics,

and, lately, in the fields of novel biomimetic materials. The possibility to modify keratin enzymatically constitutes another important aspect, applying to the “green chemistry” approach. Therefore, for the first time, we present here a successful attempt to enzymatically phosphorylate hair keratin. As was previously shown by others [5] and by our group [157, 244], fibrous materials can be enzymatically modified by protein kinase A. Different physicochemical properties could be tailored by the attachment of incoming phospho-group, such as hydrophobicity and conformational changes in fibrous materials. During their biogenesis, keratinous fibers undergo post-translational modifications by endogenous enzymes [231]. Thus, any additional information on (modified) keratin behavior in different systems may be beneficial for future investigations.

Phosphorylation of hair and its subsequent detection was a somewhat challenging task, since the levels of phosphate incorporation onto keratin are considered to be very low. The main obstacle is the low availability of amino acid residues, suitable for phosphorylation by PKA. Of all residues, constituting different keratin polypeptide chains and that could undergo phosphorylation (Ser, Tyr, Thr), only Ser and Thr side residues are suitable substrates of PKA [88]. The enzymatic reaction, however, cannot proceed on intact hair fiber, it needs to be profoundly bleached. In the current work, $\approx 7\%$ of dry hair mass was lost due to the bleaching. The damage caused by the bleaching can be roughly divided into two categories: surface damage to the cuticle and structural damage to the bulk fiber. After the bleaching process severe cuticle perforations, breaking and lifting of cuticular scales, coupled to decreased crosslink density of the hair cortex were previously reported [245, 246]. Several amino acids: cystine, Lys, Arg, Pro and Thr are oxidized [247]; leaving merely Ser suitable for PKA action. As Ser constitutes $\approx 11.6\%$ of total amino acids in $\mu\text{mol}\cdot\text{g}^{-1}$ of a dry and chemically intact Caucasian hair [248], one should also consider the condition whether this Ser is a part of enzyme recognition sequence or not. All of the above statements lead to conclusion that the phosphorylation extent is quite low. Figure S4.1 supports that notion, although the wool presented there underwent only delipidation, whilst hair underwent both delipidation and bleaching. Final outcome is that PKA recognition sequence and general accession factors of enzyme towards a substrate (steric hindrance) probably play a pivotal role in limiting the phosphorylation extent.

ATR-FTIR and DRIFT techniques use different optical phenomena of specular and diffuse reflection, respectively. DRIFT is particularly useful in the investigations of powdered and diluted (or low-amount present) samples [249]. As such, for the modified hair it was possible to obtain phosphate-specific signal solely in a DRIFT-derived spectra. Different vibrations, originating from the phosphorylated Ser side chain are of P=O, P–OH and P–O–C major types. In the chosen ROI, P=O stretching ($1250\text{-}1300\text{ cm}^{-1}$) and P–OH deformation ($\approx 1050\text{ cm}^{-1}$) vibrations [12] were currently not observed; P–OH vibration was possibly masked by more intense P–O–C stretching vibration [250] (aliphatic, $1000\text{-}1100\text{ cm}^{-1}$). P–O–C vibration itself was seen shifted, along with the appearance of *Restrahlen* band (Figure 4.1, A). Since DRIFT performance depends on diffuse, or volume, scattering, the size of abraded sample particles may provoke unwanted specular reflection, thus resulting in the observed artefact [251].

Phosphate incorporation was further confirmed by NMR analysis of protease-degraded hair keratin. Due to a subtle phosphorus amounts present in the sample, no additional salts were used in the protease buffer formulation, to avoid possible precipitation of phosphate. Divalent metal cations like Mg^{+2} or Ca^{+2} are known to facilitate enzyme-driven reactions. Specifically, Esperase® 8.0L protease demonstrates enhanced stability and performance with Ca^{+2} ions present in reaction buffer [252]. However, no *in vitro* phosphorylation-specific peak was obtained for the digested hair samples, when calcium was present as buffer compound (data not shown). Calcium phosphate salt formation and its subsequent precipitation at elevated temperature and pH may be accountable for that result [253]. The already mentioned presence of a weak peak in the negative control (Figure 4.1, B, lower panel) may stem from an *in vivo* post-translational modification of keratin. Indeed, such phosphorylation of several human hard α -keratin and matrix proteins was previously visualized by immuno-blotting [231]. NMR studies, previously done on phosphorylated keratins, showed considerably low amounts of phosphate present within a tested samples [87, 254].

One of the main outcomes of this study is that phosphate-modified adsorbent demonstrated higher affinity towards the dye adsorbate. Keratin is a polyampholyte with pI of 4.7–5.4 [255], so the charge deployed on it is pH-dependent and negative at physiological pH. The incoming phosphate group further

enforces that negative charge, as its $pK_{a2} = 5.78$ [144], thus resulting in higher dye affinity to the hair and elevated Q values (Figures 4.2; 4.3; 4.4, **B**; 4.5, **B**).

Concordantly with the approach that adsorption reaction models are widely employed to describe the process of adsorbent uptake, in the current work three kinetic models were tested. It was found that model fitting decreased as following: PSO > PFO > Intra-particle model. For both PSO and PFO models, the reaction rate-limiting step is the surface adsorption. In the case of PSO for an observed system, MB removal from a solution and its deposition on hair is due to physicochemical interactions between the two phases (chemisorption). From the thermodynamic modelling, discussed later, it is clearly seen that the adsorption process is indeed of chemisorption type. On the contrary, PFO is thought to describe the dye deposition process by van der Waals forces between the dye and the hair (physisorption). Thus PFO model does not account for several adsorbate-related parameters and therefore is less accurate. Moreover, one of the deviations from the intra-particle model (Weber-Morris), used herein, represents another concept where the rate limiting step is the adsorbate diffusion through porous structure of adsorbent ([256] and references within). In some cases (as presented here and in the literature [226, 232]) adsorbent boundary layer diffusion effects impose additional outcomes on the total adsorption process. Adsorption kinetics may thus be controlled by external diffusion in the bulk phase and intra-particle diffusion simultaneously. A non-zero slope of the fit curves, shown in Figure S4.3, **C** and a non-zero values of constant C (Table 4.2) support the latter claim. However, the donation of intra-particle diffusion to the total process seem to be insufficient for that model to acquire superior \bar{R}^2 values. At the same time, it can be seen that phosphorylation increases dye affinity to the adsorbent and decreases dye picking times. All the modeling outputs, presented in Table 4.2, clearly show the differences between the modified and the non-modified fibers. Another important feature of the made system is that the differences in dye adsorption are starting to be visible already from the 10th minute of incubation (Figure 4, **B**), indicating rapid MB uptake by the phosphorylated fibers.

Other important insights on dye–hair interactions are elucidated by isothermal modelling. Three models fit the acquired data in the descending order: Langmuir > D–R > Freundlich. Apart of Langmuir isotherm assumptions (section 4.3.3) there is an agreed opinion that the adsorption on solid surfaces,

either physical or chemical, can be plausibly described by this model [234]. Q_{\max} values, originating from this model, appear similar to the experimentally found (compare Tables 4.2 and 4.3). The effective dissociation coefficient K_L is a measure of adsorbate affinity to the adsorbent. Compared to the literature [225, 226, 235, 239], K_L demonstrates unusually high values, what may be perceived as irreversible dye binding, especially in the range of lower $[MB]_{\text{init}}$ (Figure 4.2, 0.05-0.35 g·L⁻¹). R_L values for both adsorbent types indirectly support this notion, indicating more than just “favorable” adsorption. More recent studies on understanding the theoretical origins of empirical first- and second- order rate equations for adsorption showed that “the Langmuir kinetics indeed represents a hybrid rate equation with a variable reaction order of 1-2” [257]. This fact is important for understanding two outcomes: the relative goodness of data fitting by the pseudo -first and -second kinetic models (Table 4.2) and the suitability of Langmuir model itself for the specific adsorption data set (Table 4.3). Nevertheless this does not mean that the observed adsorption is solely constituted by a particular mechanism. In fact, in many cases the experimental systems are comprised by porous and/or disperse solids, exhibiting structural and energetic heterogeneity. Accordingly, our system is expected to possess both non-uniformities: structural (originating from hair shaft perturbations) [81, 245, 246], and energetic (originating from phosphorylation) [144]. To accommodate for the energetic surface heterogeneity Freundlich and D–R models were employed [234]. Energetic surface heterogeneity is a depth change of the local potential minima as demonstrated by physically separated adsorption sites of that surface [17]. The values of $1/n$, previously presented (section 4.3.3), support the latter notion and are similar to the reported: lower than some [226, 235] (indicating a more heterogenetic surface), or higher than others [225, 239] (indicating a less heterogenetic surface). Yet, on the basis of k_f , the adsorption capacity of our system was superior to the all others listed. Finally, the adsorption mechanism, clarified by D–R model is of chemisorption type, corroborating the reports mentioned earlier. Another feature to be noted is that Q_{\max} values seem to be overestimated by D–R isotherm, a common tendency seen also in the previous studies.

Of the thermodynamic values, calculated throughout the current work, ΔS attracts particular interest. This is due to a fact that estimations of both ΔH and ΔG for the very similar adsorption systems [225,

239] (section 4.3.4) resulted in the same tendencies. Specifically for ΔG (Table 4.4), whose values neither fall to the range of pure physisorption (-20 – 0 $\text{kJ}\cdot\text{mol}^{-1}$) nor chemisorption (-80 – -400 $\text{kJ}\cdot\text{mol}^{-1}$) [258], ion-exchange mechanism was proposed earlier in this work, on E values basis (section 5.3.4). The sole work dealing with MB uptake by virgin wool keratin, reports on significantly negative entropy change [239], while our study reports a slight positive change. Since both animal wool and human hair are very similar in structure and composition [57], there is a need to explain the observed discrepancy. It is known that positive entropic contributions upon binding mainly include the release of counter-ions, while negative contributions stem from the decreased mobility of adsorbates [259]. If one compares the oxidized keratin surface with the intact surface, the first is most probable to include various ions due to the oxidation by H_2O_2 -originating radicals ($\text{OH}\cdot$, ferryl radical). The radicals may emerge as H_2O_2 is reduced by a protein-bound metals [247], naturally occurring in the melanin granules of hair (Al, Mg, K, Ca, Fe and Zn) [260]. Some of the other mentioned adsorption systems, possessing ion exchange mechanism [235, 241], exhibited positive ΔS values during the adsorbate uptake, thus making the explanation of the current observation quite plausible.

An interesting outcome was obtained from 3D imaging. As a highly heterogeneous material, the hair possesses sites of variable dye affinity, and this affinity can be somewhat increased by phosphorylation. However, it was not possible to discriminate between the phospho-sites and the rest, based on fluorescent microscopy. Hence only the totally increased amount of a bound MB, visualized by 3D reconstruction, provides additional support to the rest of experimental data, currently collected.

To conclude, the performed study assessed hair keratin-based adsorption system. The system was found to be a highly non-homogeneous, physically and energetically alike. Several adsorption mechanisms, governed by the dye–hair interactions, were present during the same discrete time of the adsorption studies. Thus there was no single model to describe the total process accurately, instead, each of them (whether kinetic or thermodynamic) solely sufficed for the elucidation of a particular aspect. The idea of enzyme-driven tailoring of material properties sounds attractive, yet the meaningful drawbacks exist. These are comprised mainly by the enzyme costs and the low levels of modification

applied, thus making the idea currently inconceivable for the large-scale industrial applications. Further research on enzymatic stability and specificity may help solve the mentioned issues in the future.

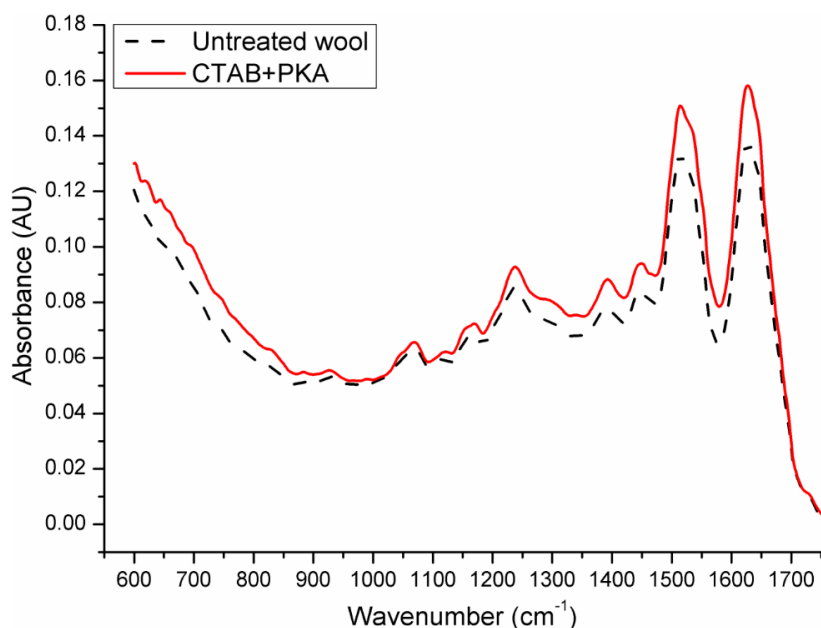
Acknowledgements

The authors would like to acknowledge the support, granted by the following projects: “**BioEnv**” - Biotechnology and Bioengineering for a sustainable world”, REF. NORTE-07-0124-FEDER-000048; and “**BioInd**” - Biotechnology and Bioengineering for improved Industrial and Agro-Food processes”, REF. NORTE-07-0124-FEDER-000028. Both projects are co-funded by the Programa Operacional Regional do Norte (ON.2 – O Novo Norte), QREN, FEDER.

Enzymatic phosphorylation of hair keratin enhances fast adsorption of cationic moieties

S Supplementary material.

A.



B.

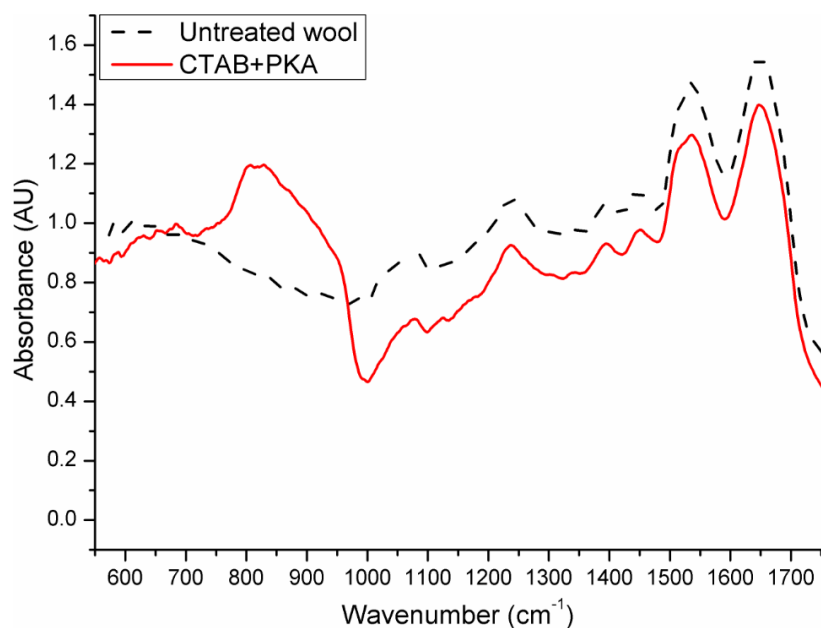


Figure S4.1. Representation of two different IR techniques for analyzing wool keratin sample. Woven 100% Merino wool fabrics (Albano Antunes Morgado Lda, Portugal) were delipided with cetyltrimethylammonium bromide (CTAB, Cat.nr. H6269, Sigma-Aldrich) and subsequently phosphorylated with protein kinase A (PKA), or left untreated. **A.**, ATR-FTIR-derived spectra. **B.**, DRIFT-derived spectra, smoothed prior to final plotting as described in the text.

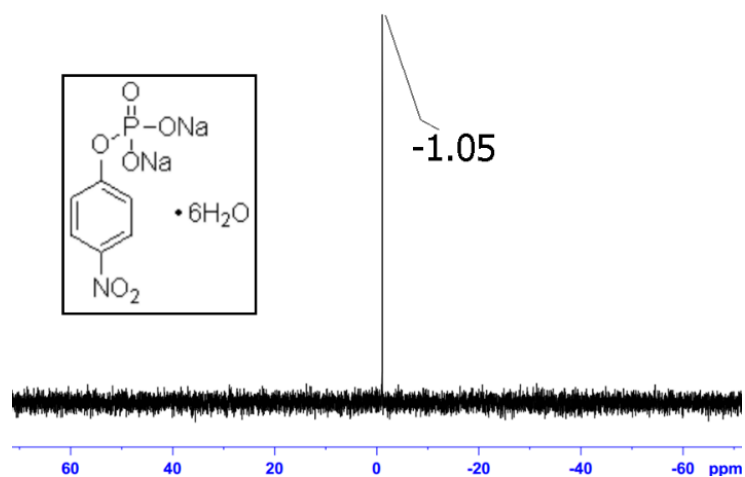


Figure S4.2. Sensitivity of used NMR equipment to ^{31}P . 2 mM para-Nitrophenylphosphate (pNPP, Cat.nr. P4744, Sigma-Aldrich) in ultra-pure water were scanned as described in the text. 256 transient scans were performed. Inset shows the structure of pNPP.

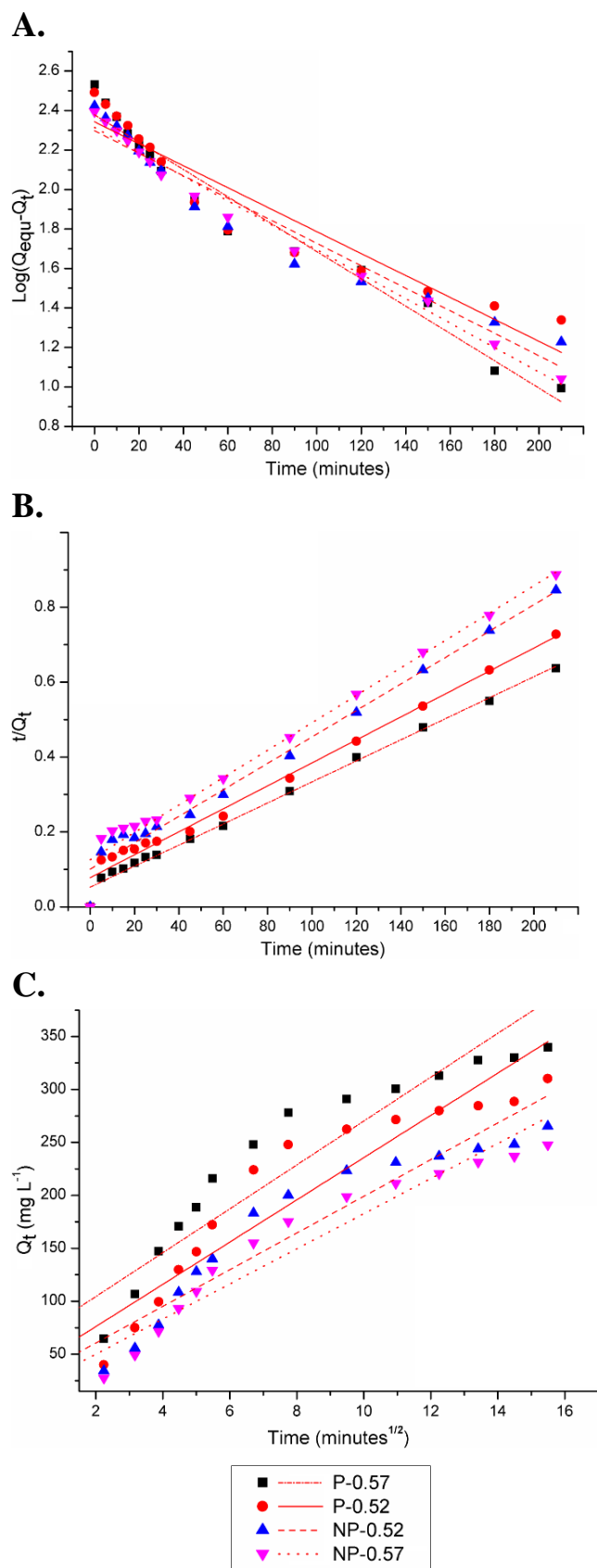


Figure S4.3. Modelling of MB adsorption onto hair samples. **A.**, **B.** and **C.** correspond to pseudo-first, pseudo-second and intra-particle diffusion models. Q_{equ} and Q_t correspond to adsorption capacities at experimental equilibrium or at specific time t . All the panels share a common legend, given at bottom. The designations of hair types and dye concentrations are stated in the text.

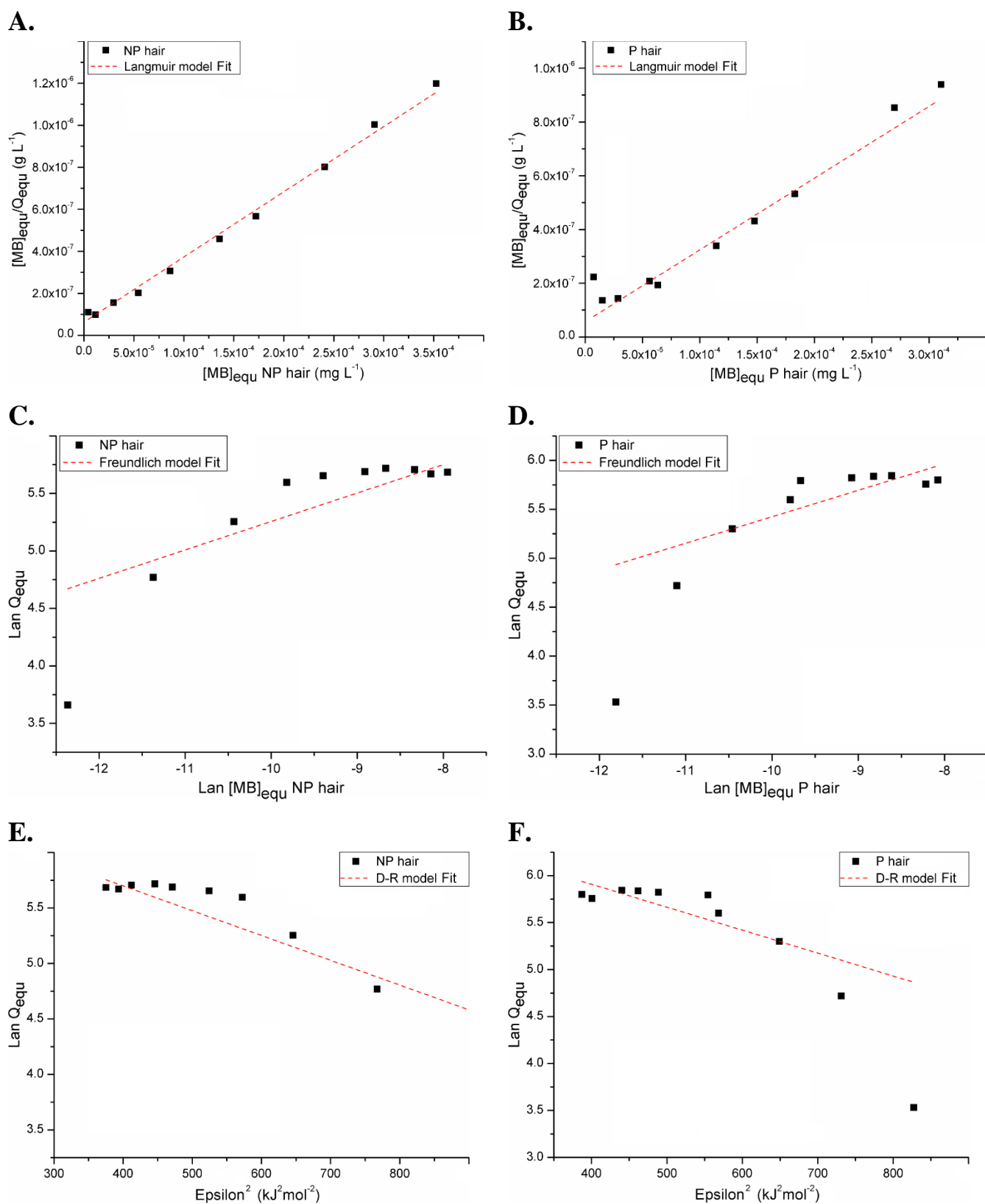


Figure S4.4. Modelling of MB adsorption onto hair samples. **A.** and **B.**, Langmuir-fitted data. **C.** and **D.**, Freundlich-fitted data. **E.** and **F.**, Dubinin–Radushkevich-fitted data. Q_{equ} and $[MB]_{\text{equ}}$ correspond to adsorption capacities and MB concentration, at experimental equilibrium, respectively. ε is a constant related to the Polanyi potential. Fitting was performed as described in the text.

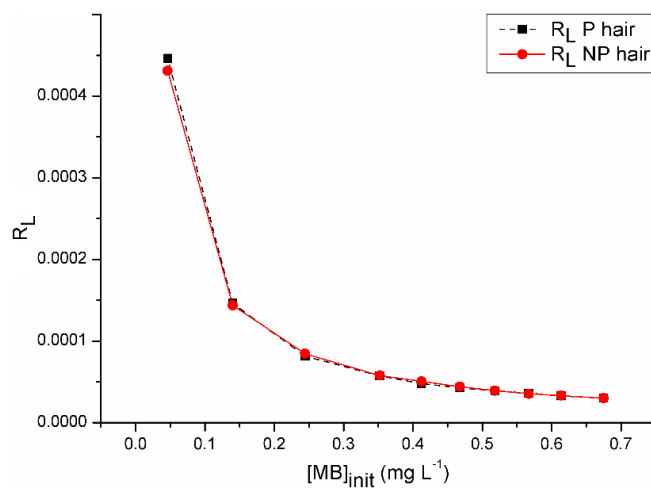


Figure S4.5. The separation factor R_L for (non-)phosphorylated hair. R_L , a Langmuir-derived dimensionless constant, was calculated as described in the text. $[MB]_{init}$ corresponds to the initial MB concentration.

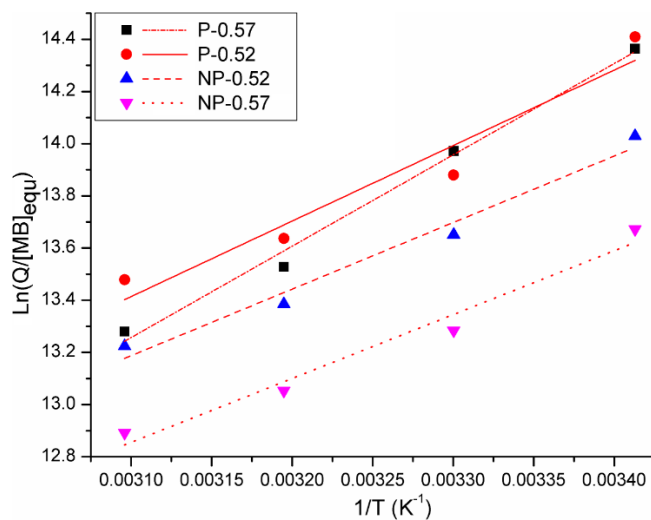
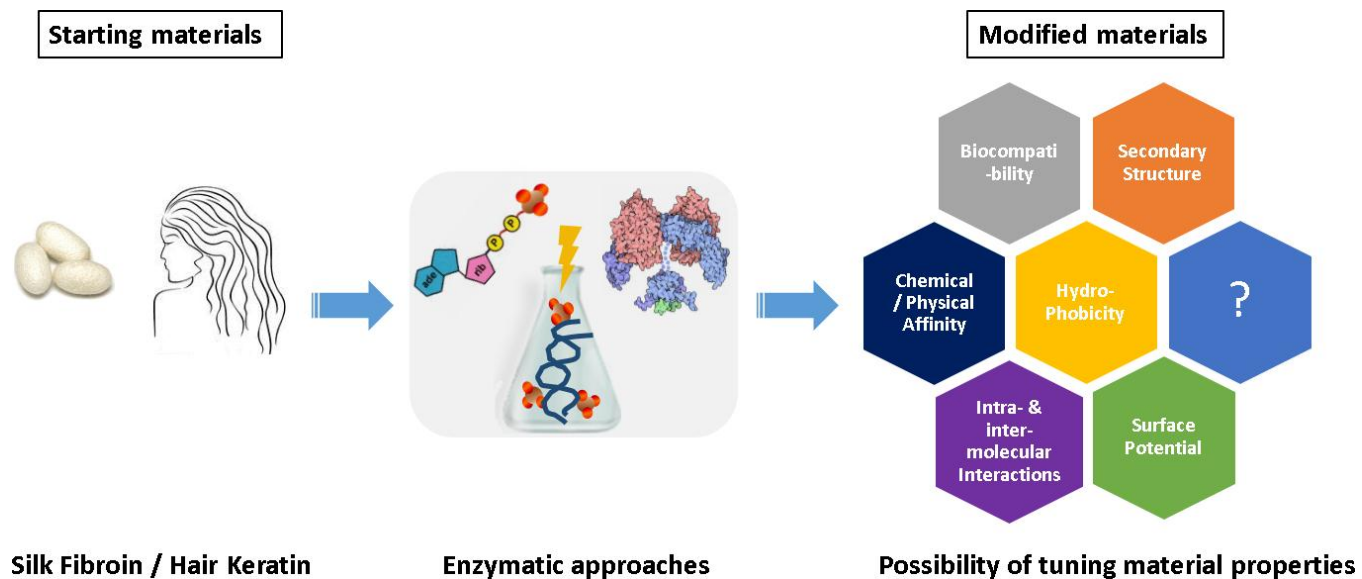


Figure S4.6. van't Hoff plots for MB dye adsorption onto (non-)phosphorylated hair. $[MB]_{equ}$ corresponds to MB concentration at experimental equilibrium, T is temperature in °Kelvin.

Chapter V



Chapter V

***In vitro* phosphorylation as tool for modification of protein fiber materials**

Abstract

The current communication aims to show the concept of *in vitro* enzymatic phosphorylation of the chosen fibrous materials, wild type silk fibroin and human hair keratin. An overview of three studies, presented herein, illustrates two important outcomes: 1. natural fibrous materials can undergo enzymatic phosphorylation; 2. phosphorylation made it possible to tailor various structural and physicochemical properties of the materials of interest. Additional attractive aspects of the proposed modification are constituted by the fact that mild reaction conditions are employed, and the treatment falls within “green chemistry” approach. The latter statements are particularly significant in the view of alleviating future possible issues of biocompatibility and avoiding the usage of harsh chemicals or treatments. In spite of the fact that in the last decades enzyme-mediated reactions are gaining more abundance, phosphorylation seems to be largely underestimated and unexplored. Hence, the current communication presents a noteworthy piece of scientific study stating that phosphorylation *per se* may be used as a valuable biochemical tool.

This chapter is based on the following publication (to be submitted): **Vadim Volkov** and Artur Cavaco-Paulo, *In vitro* phosphorylation as tool for modification of protein fiber materials.

5.1. Introduction

Fibrous materials, whether natural or man-made, are been intensely studied and used in the variety of applications, such as civil engineering [261], medicine [262], chemistry [263], industry [264], among others due to their attractive and tunable properties. Nature demonstrates numerous examples where materials in a fibrous form are utilized to compose highly complex and multifunctional structures (reviewed in [265, 266]). However, in some cases and under specific conditions, inherently non-fibrous proteins may form thin and extended fibrils, which are closely related to a number of pathological amyloid and prion states [267].

Mulberry silk fibroin (SF) and, especially, hair keratin are probably one of the most recognized natural fibrous materials by a broad community. The silk of domesticated silkworm has been a basis of sericulture for many centuries [268], while hair keratin appears a target of an industry for cosmetic and care products [47]. Since when the scientists and engineers began to realize the potential of SF and keratin in novel application fields, considerable amount of data regarding their structure, properties and possible usages was reported. Several examples, covering both materials, include, but are not limited to [10, 31, 48, 63, 65, 66, 155, 269].

While working with some raw material, in most cases the researches wish to customize a final product, rendering (bio-) chemistry indispensable. In the last decades numerous attempts were made to substitute the “conventional”, purely chemical methods, by a more environment-friendly, so-called “green chemistry” techniques [270]. In that extent, enzymatically-driven reactions attract significant attention, not only for being relatively non-hazardous or harsh treatments, but also due to their high specificity towards the substrates [94]. Working particularly on biomaterials like silk and keratin, it seems reasonable to employ enzymatic reactions for the diversification of the aforementioned substrates. *In vivo* enzymatic phosphorylation is one of the best studied post-translational modifications (PTMs) [271], with fibrous material targets as no exception. In general, phosphorylation may induce conformational changes at both local and global levels *via* allosteric regulation of protein networks [272]. Other important aspects of this modification type like its physiological stability [106] and molecular interactions modulation [105] have been presented previously. Specifically to SF [273, 274]

and (solid) keratin fibers or filaments [85, 86, 215, 216, 231, 254], some pieces of evidence regarding *in vivo* phosphorylation were demonstrated in the past. However, only single works exist on enzymatic *in vitro* phosphorylation of both SF [5] and keratin [87]. In the first case, a transgenic short variant of spider silk was modified, whereas in the second bovine hoof-extracted keratin was processed. Both fibrous materials were phosphorylated in saluted forms, protein kinase A (PKA, EC 2.7.11.11) was the enzyme of choice.

In the current communication we summarize the experimental outcomes of three works, dealing with the reconstituted enzymatic reaction for modification of the chosen fibrous materials. It was of our interest to evaluate the possibility of enzyme-driven phosphorylation of the saluted wild type SF and solid human hair keratin fiber. We clearly show that similarly to the natural processes, the phosphorylation of substrates, challenging to work with, can be performed in laboratory. This communication reports a more profound work on SF. Owing to this fact, we were able to elucidate the effects of phosphorylation on silk more extensively than on keratin.

5.2. Phosphorylation feasibility and its implications on fibrous materials

5.2.1 The feasibility of phosphorylation reaction

5.2.1.1. Silk fibroin

Prior to attempting the phosphorylation reaction of SF, the very possibility of this modification was assessed *in silico* as described [157]. As such, 20 potential PKA recognition sites, of which 14 are found within hydrophobic region and are of primary importance, were detected (Figure 5.1). SF was degummed and solubilized *via* the common protocols [111, 157], with the PKA-mediated phosphorylation followed. The optimized enzymatic reaction resulted in $\approx 60\%$ of all predicted sites, as reported by colorimetric estimation of amounts of transferred phosphoryl group. The presence of the incorporated phosphate was further shown by FTIR (Figure 5.2) for different blended fibroin films, elaborated by solvent casting and subsequent evaporation. P–OH deformation vibration-specific peak at 1039 cm^{-1} [12] supported the concept of *in vitro* phosphorylation.

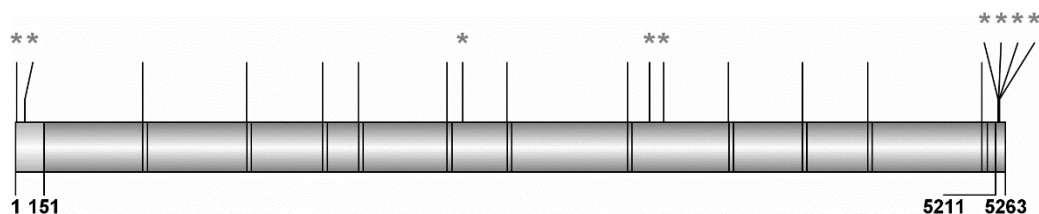


Figure 5.1. The representation of predicted phosphorylated residues in *B.mori* SF. Asterisks denote the positions, estimated by the software, whilst the remaining sites were deduced upon protein sequence analysis using the consensus motif of PKA. Three major segment types, present in the protein, are indicated. Those include the N-terminal acidic and C-terminal basic domains, and 11 “amorphous” sequences. The rest is repetitive crystalline region [10]. Borders of N- and C-terminal domains are indicated. This image was elaborated using the software, included with GPS v2.1 pack [11] and taken from [157].

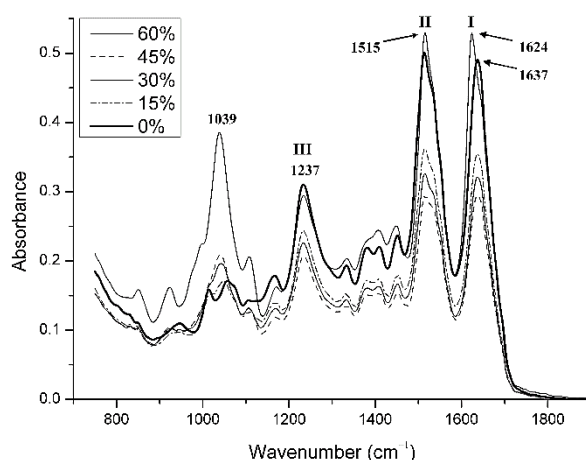


Figure 5.2. FTIR spectra of SF films of various phosphorylation degrees. Main Amide-related peaks (I, II and III) and phosphorylation-derived peak are indicated. 0%...60% indicate the final phosphorylation degree. Figure was taken from [157].

5.2.1.2. Hair keratin

As opposed to silk, the keratin (in the solid form of hair tresses) was solely bleached and taken into kinase reaction (manuscript submitted). Due to the specificity of its processing, no bioinformatics-based prediction regarding the number of possible phospho-sites could be drawn. Yet, the previous successful attempt of keratin *in vitro* phosphorylation [87] made it possible to assume the feasibility of such modification. Indeed, Diffuse Reflection Infrared Spectroscopy (DRIFTS) and NMR assays of the modified keratin demonstrated although somewhat subtle, but present phosphate (Figure 5.3). The word “subtle” signifies the fact that, similarly to SF, where only 20 phosphorylation-suitable amino acids of 5263 ($\approx 0.38\%$) were found, keratin modification was accomplished to some low levels. For instance,

instead of performing regular FTIR, a more sensitive DRIFTS was done [249]. Accordingly, 20700-20900 transient scans were taken during NMR analysis to make the phospho-peak in Figure 5.3, **B** form.

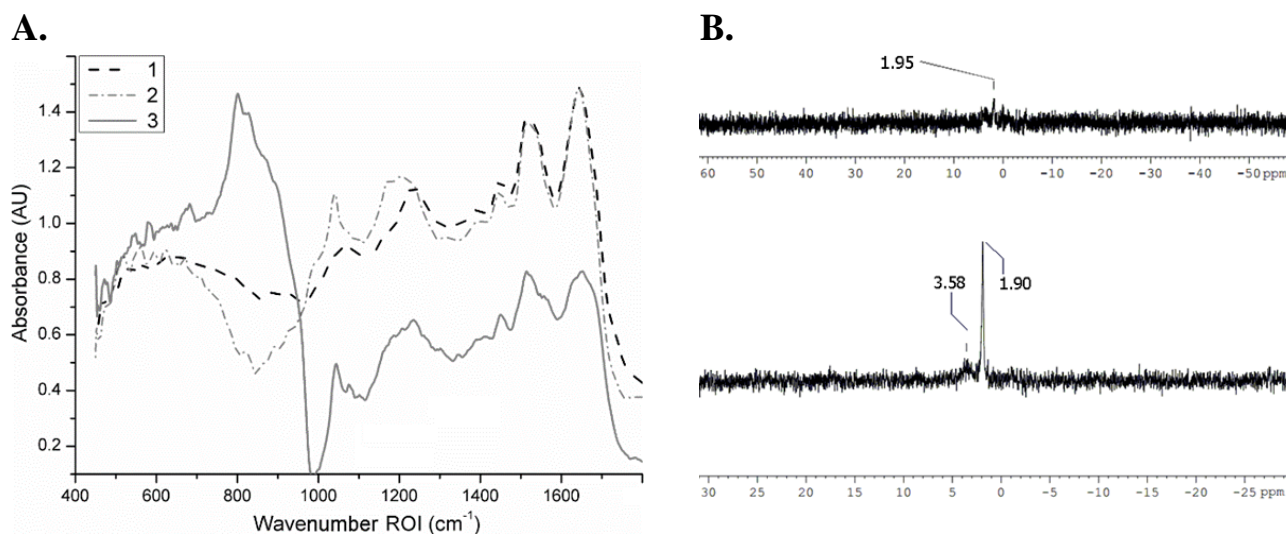


Figure 5.3. Experimental evidence of hair keratin phosphorylation. **A.**, DRIFT spectra of hair dust, obtained from its outermost layers. 1 – virgin hair, 2 – chemically damaged (bleached) hair, 3 – bleached and subsequently phosphorylated hair. **B.**, NMR spectra of keratin peptides, liberated by protease-mediated hair degradation. Top – bleached hair only, bottom – bleached and subsequently phosphorylated hair.

5.2.2. Phosphorylation implications on fibrous materials

5.2.2.1. Silk fibroin

In general, β -sheet-forming proteins are difficult to maintain in aqueous solution due to the presence of hydrophobic domains that exclude water. Hydrophobic domains constitute a major part of silk heavy chain (H-chain) proteins and lead to the formation of strong intra- and inter- molecular β -related secondary structures, responsible for insolubility, high strength and thermal stability of the silk fibers. Those secondary structures of silks, reflected in the polymorphic behavior of fibrous proteins, are a critical issue in the control of solubility of these proteins. Working on wild type mulberry silk of domestic silkworm (H-chain protein), we corroborated previously published results of Winkler *et al.* [5], while they had chosen a significantly different experimental system to work on. Winkler *et al.* demonstrated a system of transgenic spider silk fragment with the attached PKA recognition sequence. Their system was clearly tuned by (de-) phosphorylation in terms of β -sheet content and the resulting solubility. Notwithstanding, the transgenic system represented a ≈ 25 kDa protein, whilst our protein of

target is estimated to be $\approx 350 - 391$ kDa in size. The latter undoubtedly means that potential impacts of phosphorylation (if any) are much harder to elucidate. Nevertheless, all the different works (preceding this communication and presented herein) show that innate hydrophobicity of silk, as well as its self-assembly, are highly dependent on polypeptide charges and steric hindrance factors, introduced by the phospho-group. This view, emerging from the currently presented works, is constituted by several experimental outcomes.

As such, FTIR-derived secondary structure analysis and DSC assessment of (phospho-) SF films depict the degree of β -sheet formation as a function of introduced phosphoryl group and the presence of phosphate-derived plasticization effect, respectively (Figure 5.4). Another structure-related finding was the enhanced ability of the modified films to swell. It was found that the material swelling is phosphorylation dependent and is highest when half of the starting SF is phosphorylated. Besides that, a moderately increasing tendency to swell exists at a specific phosphorylation range; if the final material possesses higher phospho-content, swelling will decrease. The latter finding was explained from the basis of silk polymer relaxation degree and the ability to retain the solvent within the fibroin matrix.

When conducted at near neutral pH, the release of incorporated model compounds, whether Piroxicam [157] or Methotrexate (MTX) [244], underlined additional aspects of polymer–drug interactions. In the first case, phosphorylation decreased drug retention within the matrix, whilst no significant phosphorylation-dependent trend was detected for the second case. Decreased hydrophobicity of the modified SF matrix promoted the release of mostly hydrophobic Piroxicam. As a compound of more prominent amphoteric character, MTX presents a highly pH dependent solubility and the ability to form interactions with the embedding material. Thus the immediate impact of phosphate groups in the bulk phase may be masked or surpassed by the conditions of pH. In addition, it was clarified that structural clustering of SF chains at acidic pH values generally levelled out the phosphorylation effects [244].

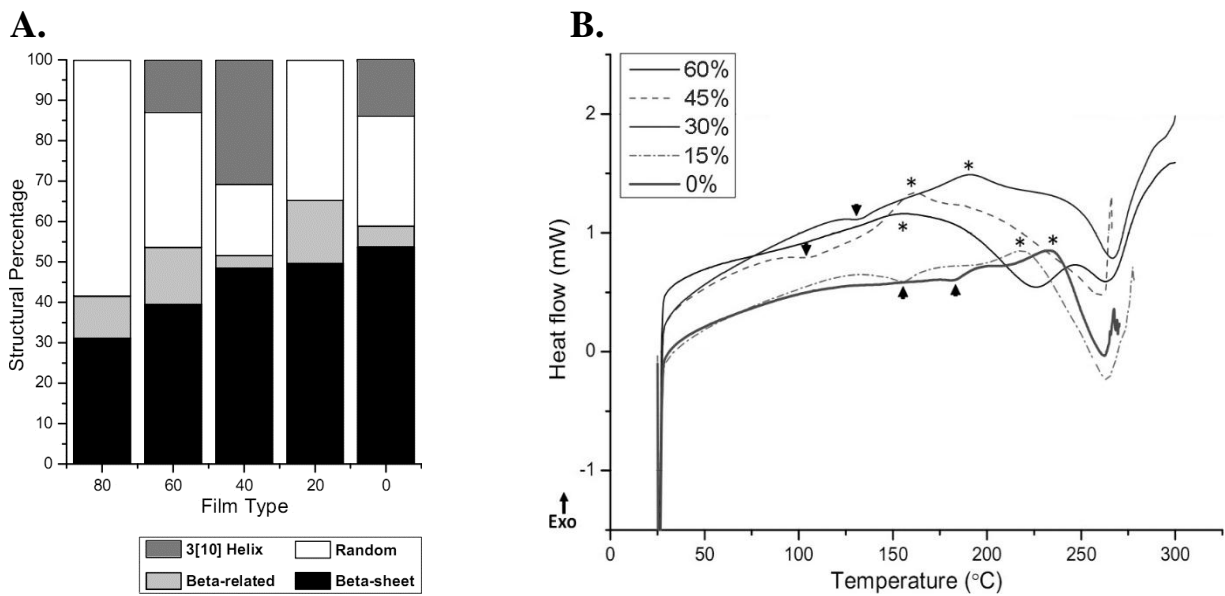


Figure 5.4. Phosphorylation impact on silk. **A.**, Dependency between phospho-content and the observed SF secondary structure. **3[10] Helix**, 3_{10} Helix; **Random**, Random coiled structure; **Beta-related**, β -related turns. **B.**, Differential scanning calorimetric analysis of blended phospho-fibroin films. Individual thermograms of the corresponding samples are shown. T_g values are represented (marked by the ▼ symbol). Crystallization endotherms are designated by the * symbol. A shift towards lower glass transition temperature as function of phosphorylated content, is recognized. Resulting figure is compiled from [157].

Silk polypeptide chain collapse and subsequent hydrophobic self-association at lower pH overcomes the phosphorylation repulsion effects due to its “modest” levels. Mechanistically, the acidified pH-driven fibroin precipitation is very similar to the ongoing self-gelation of SF aqueous solutions with time (Figure 5.5). The difference mainly stems from hydrophobic self-association and solvent exclusion speeds of the saluted material. Depending on SF concentration, solution ionic strength and surrounding temperature, the precipitation process onset and/or propagation may range from hours to weeks. In our particular case, precipitates were started to be observed from the second week of storage of $\approx 2\%$ w/t fibroin solution in dH_2O at 4°C and $\text{pH} \approx 7.3$. pH drop to ≈ 3.5 usually caused irreversible precipitation/gelation within 24 hours at room temperature, regardless of presence of the introduced phosphate. Although direct charge calculations for the modified silk demonstrated a tendency towards negative potential formation (and thus chain repulsion), as was noticed previously, this tendency is surpassed by acidification [244]. Particularly important is the role of carboxyl groups (Glu and Asp) in determining fibroin chain interactions at acidic pH values.

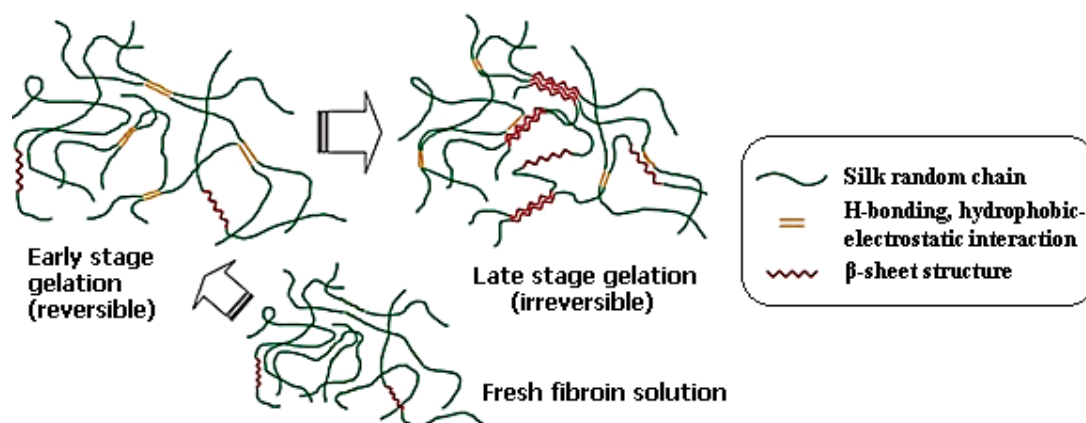


Figure 5.5. Schematic illustration of SF solution gelation development. The steps of fibroin gelation are shown as a three-stage model, according to [16].

As a hydrophilic domain, the N-terminus of H-chain of the fibroin is dominated by acidic amino acid side chains with the predicted pI of 4.59 [16]. Decreasing pH below 4.59 facilitates silk aggregation due to protonation of the carboxyl groups, and thus promotes their intra- or inter- molecular interactions. Therefore, and similarly to the previous researches, we conclude that phosphorylation of SF caused a decrease in the hydrophobic content of the fold protein, but did not completely inhibit β -sheet assembly.

Finally, in terms of cytotoxicity, it was shown that phospho-silk fibroin films seem not to promote cell attachment and, possibly, proliferation [157]. Some previously cited works [150, 151] state that increased hydrophilicity disfavors cell attachment on the surfaces. Since the cellular membrane is known to be negatively charged from the outer side at physiological conditions [275, 276], phospho-silk fibroin films will be prone to repel seeded cells. Thus, it can be solely stated with high degree of confidence that lesser attachment will occur. Conclusions relating the surface charge and proliferation levels are thought to be too biased without any empiric confirmation. Furthermore, bioactivity evaluation of the MTX-loaded films on Caco-2 cells by indirect contact showed lower proliferation rate when the MTX release was higher ([244], Figure 5.6). Thus, films of higher phosphorylation were able to retain MTX for longer time, and, importantly, denser films possessed lesser drug retention (Figure 5.6, **B**). This phenomenon was explained by some studies [188, 189] and by us previously, as a drug exclusion during the formation of the hydrophobic β -sheet network.

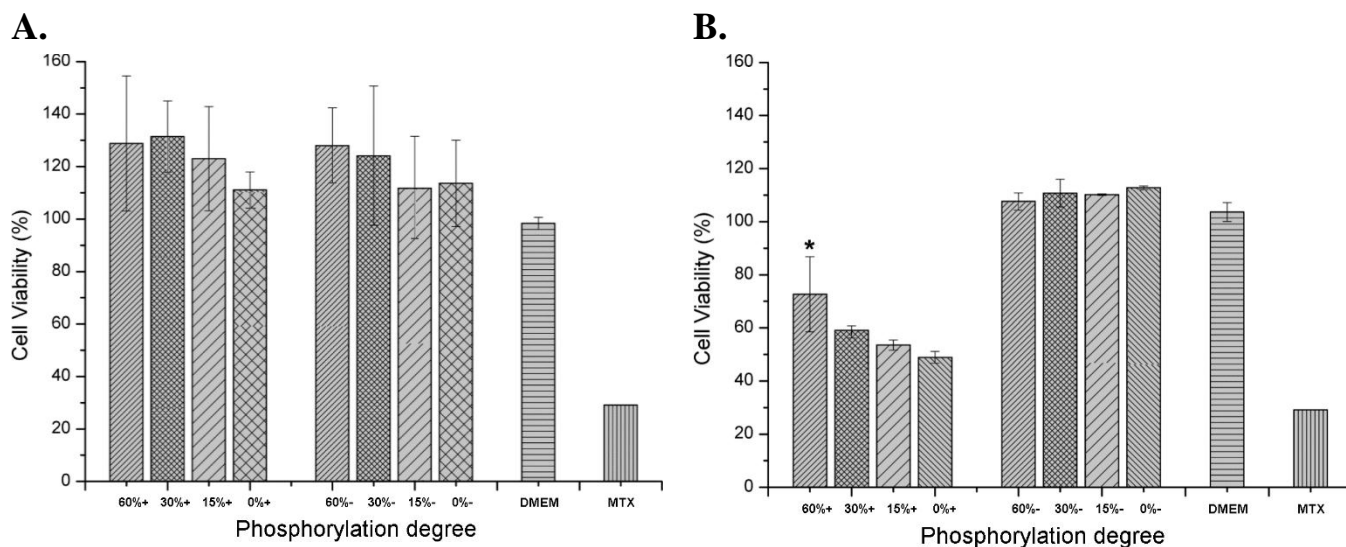


Figure 5.6. The viability of Caco-2 cell line, cultivated on lixiviates, derived from 6 hour-incubation of growth medium with silk fibroin MTX-loaded films. **A.**, pH 7.2-cast films; **B.**, pH 3.5-cast films. “+” and “-” denote the MTX –loaded or –devoid fibroin materials. DMEM = cell growth medium only, a positive control. MTX = methotrexate at 0.2 mg/ml concentration, a negative control. Statistically significant difference is denoted by asterisk. Figure taken from [244].

5.2.2.2. Hair keratin

The third article reported that for the hair keratin, the immediate outcome of phosphorylation is enhanced affinity of a model cationic compound towards the phosphorylated material, as assessed by adsorption capacity Q measurements of Methylene Blue (MB) dye (Figure 5.7, manuscript submitted). Since the enzymatic reaction was carried out on pre-formed solid material, only the considerations of adsorbent surface potential and adsorbate–adsorbent interactions were thoroughly studied and presented (manuscript submitted).

Hair is known to possess high natural heterogeneity, for the most compositional, but also structural [277, 278]. During the experimental processing human hair was extensively bleached and later phosphorylated. Structural and electric potential-related features, concurrently associated with the experimental treatments, are thought to include highly rough, perforated surface with areas of differential electrostatic potential energy. Since the later usage of a charged adsorbate, MB, as a model compound for clarification of aspects of the binding process, adsorbent surface was assumed to be energetically heterogeneous.

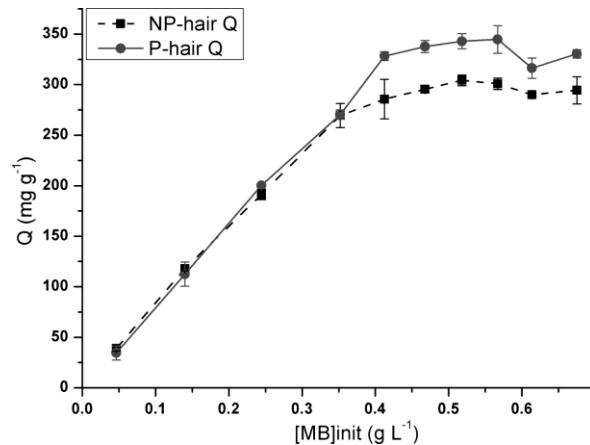


Figure 5.7. Determination of maximal adsorption capacity (Q_{\max}) for the hair samples of two types. Hair was incubated in MB solutions of varying initial concentration, $[MB]_{\text{init}}$. Q_{\max} was assessed as described. NP- and P- designate the non-modified or enzymatically modified hair.

This can be emphasized in Figure 5.8, showing different models of surface energetic heterogeneity [17]. We further assumed this surface to be of “Intermediate” type. In a “patch-wise” type the adsorption centers of the same properties are grouped in large patches. Those patches are considered to be large enough to constitute independent thermodynamic adsorption subsystems (Figure 5.8, A). On the contrary, the completely “Random” distribution of adsorption centers causes the microscopic composition of the adsorbed phase in the surrounding of any center to be the same and identical to the average composition

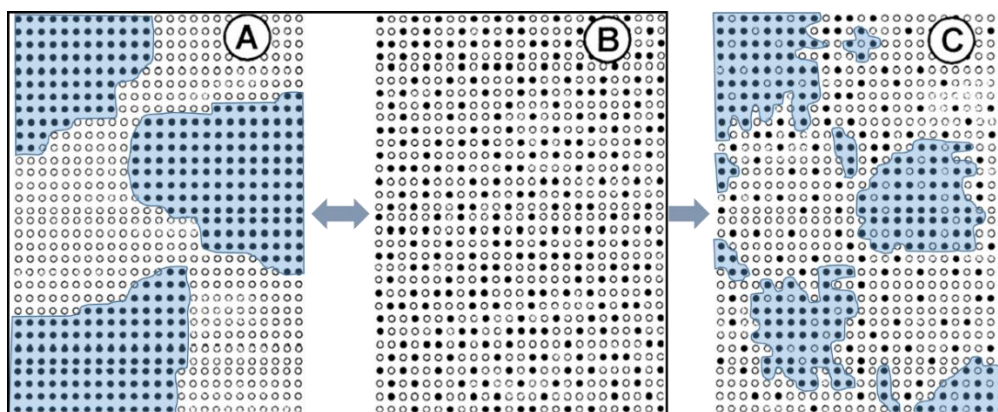


Figure 5.8. Distribution models of the surface topography of adsorption centers for various energies on the solid surface. A., “Patch-wise” type surface. B., “Random” type surface. C., “Intermediate” type surface. Two energetically distinct types of adsorption centers are marked with filled and blank circles. Where possible, the areas of similar energy potentials are marked by cyan filler. The image was adapted from [17].

of the phase on the bulk solid surface (Figure 5.8, **B**). Thus, the “Patch-wise” and “Random” surface topographies represent two boundary cases for any solid adsorbent. In the particular case inspected here, along with many others, intermediate topography exists so that the correlation between the energies of the adsorption of the closed neighbors or even the neighbors of the closed adsorption sites may be evident (Figure 5.8, **C**). The latter model is strongly supported by experimental evidence, depicted in Figures 9 and 10. The seemingly “pure” random distribution of dye-binding sites is disproved by the larger agglomerations of the bound MB, pointing on the locations of elevated affinity toward MB. Practically it means that whilst the distribution of these high-affinity locations may be random, the overall surface energetic heterogeneity of adsorbent falls within the pattern shown in Figure 5.8, **C**.

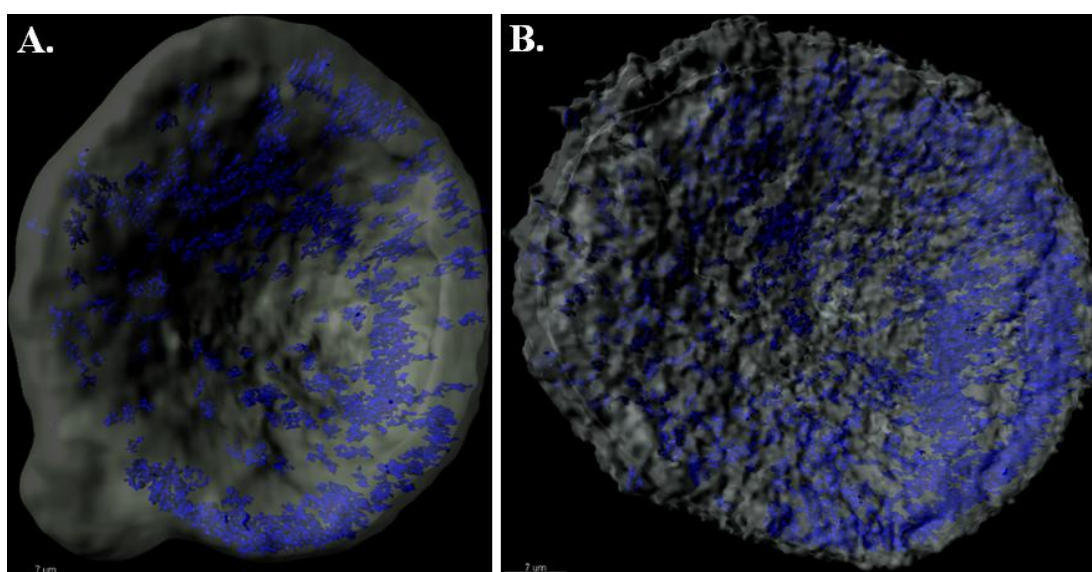


Figure 5.9. A view from the top of artificially colored 3D visualization of the sites of highest dye affinity (dark-blue) and the bulk hair adsorbent volume (light-gray). **A.**, non-modified adsorbent. **B.**, phospho-modified adsorbent. Scale bar, 7 μm. Figure taken from (manuscript submitted).

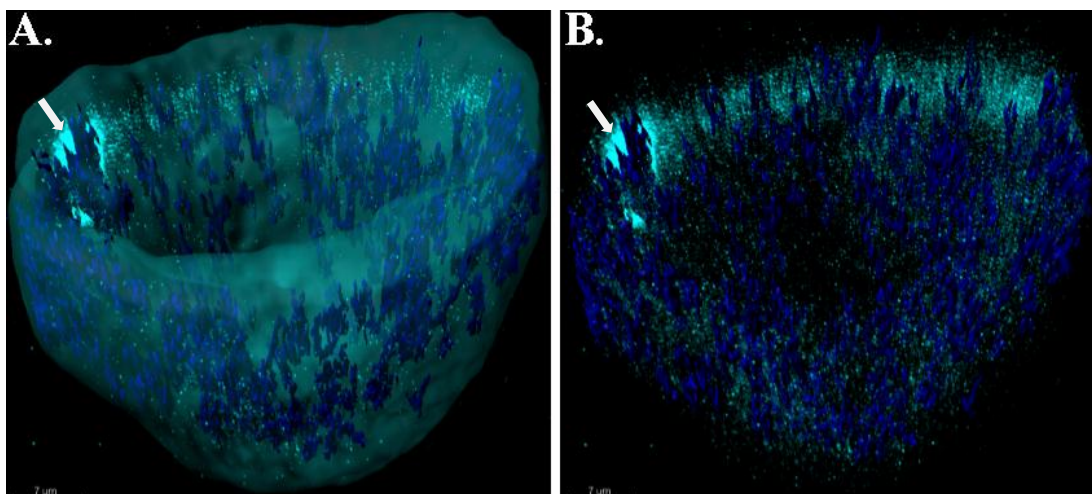


Figure 5.10. 3D reconstitution of the sites of highest dye affinity (dark-blue), other binding sites of lesser affinity and the bulk hair adsorbent volume (both in cyan). **A.**, Bulk hair adsorbent volume shown. **B.**, Bulk hair adsorbent volume omitted for clarity. Fluorescent artefact is denoted by an arrow. Scale bar, 7 μm .

From calculations, based on 3D reconstruction of the bound MB (2D imprint is shown as Figure 9), a 29.1% increase in the dye binding sites as a result of phosphorylation was detected. The data acquired throughout the third study advocate for phosphorylation as a binder enhancer for the cationic MB. Various kinetic and thermodynamic modelling approaches envisage the beneficial role of phosphorylation in hair–dye interactions. The chosen results of kinetic pseudo-second order and Langmuir isothermal modellings are presented in Tables 5.1 and 5.2, respectively. Several important aspects of adsorption, such as the rate-limiting step of MB removal from a solution and its deposition on hair, thermodynamic modelling outcomes like the mean energy of adsorption, among others, were elucidated (manuscript submitted). They made possible to conclude that pseudo-second order (PSO) model, along with Langmuir isothermal model characterize best the hair-based adsorption system. Moreover, for the observed system, MB adsorption was exothermic and energetically favored process, with entropy increase.

Table 5.1. Various estimated parameters of MB dye adsorption on different hair types.

Model applied	Hair types	Parameters, calculated from modelling		
Kinetic Pseudo-second order		Q_{\max} ($\text{mg}\cdot\text{g}^{-1}$)	k_2 ($\text{g}\cdot\text{mg}^{-1}\cdot\text{min}^{-1}$)	\bar{R}^2
	P	355.871	$1.504\cdot 10^{-4}$	0.9924
	NP	273.224	$1.067 \cdot 10^{-4}$	0.9747
Langmuir Isothermal		Q_{\max} ($\text{mg}\cdot\text{g}^{-1}$)	K_L ($\text{L}\cdot\text{mg}^{-1}$)	\bar{R}^2
	P	374.531	$46.675\cdot 10^3$	0.9647
	NP	322.580	$49.301\cdot 10^3$	0.9868

Q_{\max} , maximal dye absorption capacity; k_2 , adsorption rate constant; K_L , effective dissociation constant. NP and P designate the non-modified or enzymatically modified hair.

Table 5.2. Thermodynamic parameters of the MB dye adsorption onto different hair types.

Hair type	van't Hoff equation-derived			ΔG at chosen temperature (kJ·mol ⁻¹)			
	ΔH (kJ·mol ⁻¹)	ΔS (J·mol ⁻¹)	R ²	20 °C	30 °C	40 °C	50 °C
P	-29.106	19.991	0.9882	-34.990	-35.196	-35.204	-35.663
NP	-20.347	43.803	0.9573	-33.306	-33.463	-33.967	-34.620

Calculated values of enthalpy ΔH , entropy ΔS and Gibbs free energy ΔG . NP and P designate the non-modified or enzymatically modified hair.

Summarizing, from the pairwise comparison of virtually all kinetic and thermodynamic parameters, presented in Tables 5.1 and 5.2, it is seen that phosphorylation enhances the affinity of the hair to MB dye.

5.3. Conclusions

The three works, presented herein [157, 244] (manuscript submitted), clearly demonstrate that natural fibrous materials of SF and keratin can undergo *in vitro* enzymatic phosphorylation. For hair keratin the conclusion is even more striking, since it was processed as a solid fiber, and not a mixture of solubilized proteins, obtained by extraction. However, *in vivo* modification of the chosen fibrous materials still poses important questions. The biological meaning of post-translational modifications for both keratin [85, 86, 215, 216, 231, 254] and, particularly, SF [273, 274], still remain unclear. It is easily seen that the majority of available data correspond to keratin, and not silk. This fact stands to reason, as it has been established for a long time that keratin filaments (along with vimentin, desmin and neurofilament triplet proteins) play pivotal role in eukaryotic cell biology, for instance in cytoskeleton remodeling and mechanical stability of cellular compartments like nucleus [279]. Nevertheless, the aspects of keratin filaments function in cell biology are out of the scope of a current communication. Keratin filament self-organization and keratin binding regulation are additional plausible explanations, analogous to those already postulated for different tissues (reviewed in [14] and Figure 5.11). Previously cited literature only suggests the hypotheses of silk protein conformation remodeling and the alteration of binding to other factors. Unfortunately, the currently available data do not allow further conclusions for the role of silk *in vivo* phosphorylation. This lack of information is another important point that coerced us to

conduct the work. It may be possible, to some extent, to extrapolate the obtained *in vitro* outcomes for *in vivo* systems, thus enriching our understanding of them.

Another key finding gleaned from the following studies is that phosphorylation made it possible to tailor various structural and physicochemical properties of the materials of interest. For both SF and keratin, the hallmark of obtained results unambiguously demonstrates that phosphorylation considerably alters the surfaces of polypeptide chains. For silk, alteration of secondary structure and density of forming hydrophobic packaging leads to varying retention of the incorporated drugs and decreased cell affinity. The latter may be important in material design, where cell attachment to implant surface is unwanted [153]. For keratin, the improved affinity towards positively charged species, found in the surrounding solution, may implicate the feasibility of phosphorylation for hair pre-treatments in case of cosmetic applications, where cationic surfactants are commonly applied ([280] and references within).

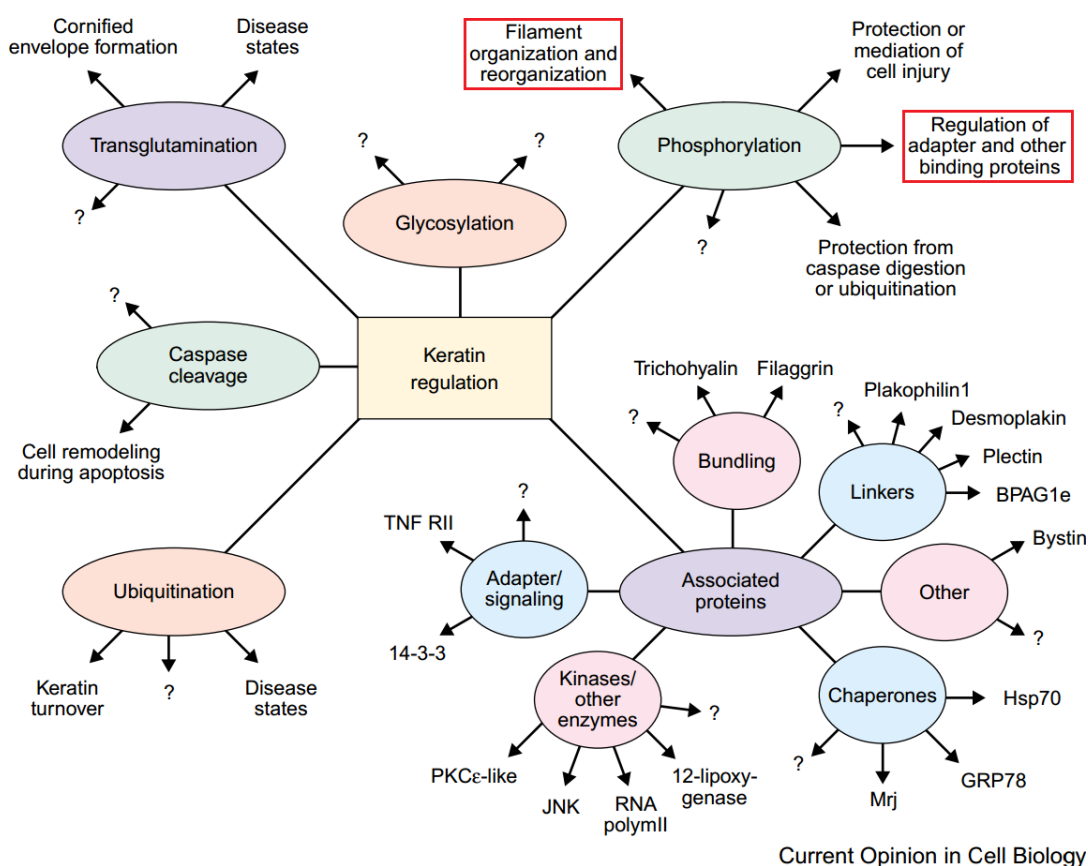


Figure 5.11. Regulation of keratin proteins family in live tissues, according to [14]. Proposed functions of hair keratin phosphorylation, emerging from the literature, are shown in red rectangles.

5.4. Further outlook on the feasibility of phosphorylation of fibrous materials

Accordingly to the empiric data, presented herein, this enzyme-driven modification represents a valuable tool in the field of material design, especially where discriminative, site-specific alterations are demanded. Another factor that strongly advocates for enzymatic processing is the mild nature of such treatment that is of importance in medical devices fabrication and the related biocompatibility issues. Even a quantitatively minor modification, for instance, of solely 0.38% from the total amino acid amount, comprising SF H-chain, leads to considerable alteration of silk properties and the subsequent behavior of SF-based materials. Regarding hair keratin, while it was not possible to estimate the modification extent, keratin surface charge was shifted to lower values, influencing the formed electrostatic potential. Therefore, it is concluded that similarly to live systems, enzymatic phosphorylation may be successfully applied to tune various physicochemical properties *in vitro*. Indeed, convincing amount of various enzymatic processes have been implemented in a broad range of applications in recent decades [281]. However, particularly for phosphorylation, its broad utilization in large-scale (industrial) applications is currently somewhat discouraged, due to significant cost of the enzyme and its decreased stability at the reaction conditions (if compared to purely chemical reagents). In cases where mass-modification of specific functional groups or sites is needed, utilization of “canonical” chemistry may be still preferable. Future potential improvements ([282] and references within) in enzymatic stability and diversification of their consensus sequences, including *de novo* enzyme design strategies [283] may help overcome the obstacles, stated above.

References



References

1. Li, G., et al., *Surface modification and functionalization of silk fibroin fibers/fabric toward high performance applications*. Mater. Sci. Eng., C, 2011. **32**(4): p. 627-636.
2. Yang, Y., et al., *Behavior of silk protein at the air–water interface*. Soft Matter, 2012. **8**: p. 9705-9712.
3. Numata, K., P. Cebe, and D.L. Kaplan, *Mechanism of enzymatic degradation of beta-sheet crystals*. Biomaterials, 2010. **31**(10): p. 2926-33.
4. Samal, S.K., et al., *Enzymatic mineralization of silk scaffolds*. Macromol Biosci, 2014. **14**(7): p. 991-1003.
5. Winkler, S., D. Wilson, and D.L. Kaplan, *Controlling beta-sheet assembly in genetically engineered silk by enzymatic Phosphorylation/Dephosphorylation*, by. Biochemistry, 2000. **39**(45): p. 14002.
6. Körner, A., *MALDI MS in Analysis of Keratin Fibre Proteins*, in *Applications of Mass Spectrometry in Life Safety*, C. Popescu, A.D. Zamfir, and N. Dinca, Editors. 2008, Springer Netherlands. p. 206.
7. Yu, D., et al., *Novel immobilization of a quaternary ammonium moiety on keratin fibers for medical applications*. Int J Biol Macromol, 2014. **70**: p. 236-40.
8. Cui, L., et al., *Transglutaminase-modified wool keratin film and its potential application in tissue engineering*. Engineering in Life Sciences, 2013. **13**(2): p. 149-155.
9. Kurimoto, A., et al., *Keratin sponge: immobilization of lysozyme*. J Biosci Bioeng, 2003. **96**(3): p. 307-9.
10. Zhou, C.Z., et al., *Silk fibroin: structural implications of a remarkable amino acid sequence*. Proteins, 2001. **44**(2): p. 119-22.
11. Xue, Y., et al., *GPS 2.0, a tool to predict kinase-specific phosphorylation sites in hierarchy*. Mol Cell Proteomics, 2008. **7**(9): p. 1598-608.
12. Bellamy, L.J. and L. Beecher, *The infra-red spectra of organo-phosphorus compounds. Part II. Esters, acids, and amines*. J. Chem. Soc., 1952(0): p. 1701-1706.
13. Ritger, P.L. and N.A. Peppas, *A simple equation for description of solute release I. Fickian and non-fickian release from non-swellable devices in the form of slabs, spheres, cylinders or discs*. J. Controlled Release, 1986. **5**(1): p. 23-26.
14. Coulombe, P.A. and M.B. Omary, *'Hard' and 'soft' principles defining the structure, function and regulation of keratin intermediate filaments*. Curr Opin Cell Biol, 2002. **14**(1): p. 110-22.
15. Adams, J.A., *Kinetic and catalytic mechanisms of protein kinases*. Chem Rev, 2001. **101**(8): p. 2271-90.
16. Matsumoto, A., et al., *Mechanisms of silk fibroin sol-gel transitions*. J Phys Chem B, 2006. **110**(43): p. 21630-8.
17. Charmas, B. and R. Lebeda, *Effect of surface heterogeneity on adsorption on solid surfaces. Application of inverse gas chromatography in the studies of energetic heterogeneity of adsorbents*. J Chromatogr A, 2000. **886**(1-2): p. 133-52.
18. Naskar, D., et al., *Introduction to silk biomaterials*, in *Silk Biomaterials for Tissue Engineering and Regenerative Medicine*, S. Kundu, Editor. 2014, Elsevier. p. 23-27.
19. Leal-Egana, A. and T. Scheibel, *Silk-based materials for biomedical applications*. Biotechnol Appl Biochem, 2010. **55**(3): p. 155-67.
20. Kaplan, D., *Silk : Biology , Structure , Properties , and Genetics*, in *Silk Polymers*, D.A. Kaplan, W Wade; Farmer, Barry; Viney, Christopher, Editor. 1994, American Chemical Society: Charlottesville, Virginia. p. 2-16.
21. Cao, Z., et al., *The preparation of regenerated silk fibroin microspheres*. Soft Matter, 2007. **3**(7): p. 910.
22. Vepari, C. and D.L. Kaplan, *Silk as a Biomaterial*. Prog Polym Sci, 2007. **32**(8-9): p. 991-1007.
23. Inoue, S., et al., *Silk fibroin of Bombyx mori is secreted, assembling a high molecular mass elementary unit consisting of H-chain, L-chain, and P25, with a 6:6:1 molar ratio*. J Biol Chem, 2000. **275**(51): p. 40517-28.
24. Chen, X., et al., *Conformation transition kinetics of regenerated Bombyx mori silk fibroin membrane monitored by time-resolved FTIR spectroscopy*. Biophys Chem, 2001. **89**(1): p. 25-34.
25. Zhou, C.Z., et al., *Fine organization of Bombyx mori fibroin heavy chain gene*. Nucleic Acids Res, 2000. **28**(12): p. 2413-9.
26. Foo, C.W.P., et al., *Role of pH and charge on silk protein assembly in insects and spiders*. Appl. Phys. A, 2006. **82**(2): p. 223-233.
27. Cao, Y. and B. Wang, *Biodegradation of silk biomaterials*. Int J Mol Sci, 2009. **10**(4): p. 1514-24.

28. Takeuchi, H., et al., *Neutrophil elastase contributes to extracellular matrix damage induced by chronic low-dose UV irradiation in a hairless mouse photoaging model*. J Dermatol Sci, 2010. **60**(3): p. 151-8.
29. Valluzzi, R., et al., *Orientation of silk III at the air-water interface*. Int J Biol Macromol, 1999. **24**(2-3): p. 237-42.
30. Padamwar, M.N. and A.P. Pawar, *Silk sericin and its applications: A review*. J. Sci. Ind. Res., 2004. **63**: p. 323-329.
31. Rockwood, D.N., et al., *Materials fabrication from Bombyx mori silk fibroin*. Nat. Protoc., 2011. **6**(10): p. 1612-31.
32. Altman, G.H., et al., *Silk-based biomaterials*. Biomaterials, 2003. **24**(3): p. 401-16.
33. Wen, C.M., et al., *Silk-induced asthma in children: a report of 64 cases*. Ann Allergy, 1990. **65**(5): p. 375-8.
34. Zhang, Y.Q., et al., *Synthesis, characterization and immunogenicity of silk fibroin-L-asparaginase bioconjugates*. J Biotechnol, 2005. **120**(3): p. 315-26.
35. Cao, T.T., Y.J. Wang, and Y.Q. Zhang, *Effect of Strongly Alkaline Electrolyzed Water on Silk Degumming and the Physical Properties of the Fibroin Fiber*. PLoS One, 2013. **8**(6): p. e65654.
36. Wang, H.-Y. and Y.-Q. Zhang, *Effect of regeneration of liquid silk fibroin on its structure and characterization*. Soft Matter, 2013. **9**: p. 138-145.
37. Shang, K., et al., *Accelerated In Vitro Degradation of Optically Clear Low -Sheet Silk Films by Enzyme-Mediated Pretreatment*. Transl Vis Sci Technol, 2013. **2**(3): p. 2.
38. Horan, R.L., et al., *In vitro degradation of silk fibroin*. Biomaterials, 2005. **26**(17): p. 3385-93.
39. Sampaio, S., et al., *Enzymatic grafting of chitosan onto Bombyx mori silk fibroin: kinetic and IR vibrational studies*. J Biotechnol, 2005. **116**(1): p. 21-33.
40. Freddi, G., et al., *Tyrosinase-catalyzed modification of Bombyx mori silk fibroin: grafting of chitosan under heterogeneous reaction conditions*. J Biotechnol, 2006. **125**(2): p. 281-94.
41. Kang, G.D., et al., *Structure modifications induced in silk fibroin by enzymatic treatments. A Raman study*. Macromol. Res., 2004. **12**(5): p. 534-539.
42. Monti, P., et al., *Structure modifications induced in silk fibroin by enzymatic treatments. A Raman study*. J. Mol. Struct., 2005. **744-747**: p. 685-690.
43. Chen, Z., et al., *Preparation of Zn(II)-Poly(acrylonitrile-co-silk fibroin peptide) Complexes : Their Odor-Removal and Antibacterial Activities*. Fiber, 2004. **60**(3): p. 81-87.
44. Chen, Z., et al., *Synthesis and Characterization of New Acrylic Polymer Containing Silk Protein*. Fiber, 2003. **59**(5): p. 168-172.
45. Chen, Z., et al., *Synthesis and characterization of spinning poly(acrylonitrile-co-silk fibroin peptide)s*. J. Appl. Polym. Sci., 2004. **92**(3): p. 1540-1547.
46. Mansour, E., et al., *Assessment of health implications related to processing and use of natural wool insulation products*. Environ Int, 2014. **73**: p. 402-12.
47. Weathersby, C. and A. McMichael, *Brazilian keratin hair treatment: a review*. J. Cosmet. Dermatol., 2013. **12**(2): p. 144-148.
48. McKittrick, J., et al., *The Structure, Functions, and Mechanical Properties of Keratin*. JOM, 2012. **64**(4): p. 449-468.
49. Parry, D.A.D. and P.M. Steinert, *Intermediate filament structure*. 1995, Heidelberg, Germany: Springer-Verlag.
50. McLaren, R.J., et al., *Linkage mapping of wool keratin and keratin-associated protein genes in sheep*. Mamm Genome, 1997. **8**(12): p. 938-40.
51. Heid, H.W., I. Moll, and W.W. Franke, *Patterns of expression of trichocytic and epithelial cytokeratins in mammalian tissues. I. Human and bovine hair follicles*. Differentiation; research in biological diversity, 1988. **37**(2): p. 137-57.
52. Yu, J., et al., *Human hair keratins*. J Invest Dermatol, 1993. **101**(1 Suppl): p. 56S-59S.
53. Fraser, R.D., et al., *Intermediate filaments in alpha-keratins*. Proc Natl Acad Sci U S A, 1986. **83**(5): p. 1179-83.
54. Koehn, H., et al., *The proteome of the wool cuticle*. J Proteome Res. **9**(6): p. 2920-8.
55. Robbins, C.R., *Chemical Composition of Different Hair Types*, in *Chemical and Physical Behavior of Human Hair*. 2011, Springer: Germany. p. 105-176.
56. Moll, R., M. Divo, and L. Langbein, *The human keratins: biology and pathology*. Histochem Cell Biol, 2008. **129**(6): p. 705-33.

57. Menkart, J., L.J. Wolfram, and I. Mao, *Caucasian Hair, Negro Hair, and Wool: Similarities and Differences*. J. Soc. Cosmet. Chem., 1966. **17**(13): p. 769-788.
58. Robbins, C.R., *Morphological and Macromolecular Structure*, in *Chemical and Physical Behavior of Human Hair*. 2002, Springer-Verlag: New York/Berlin/Heidelberg. p. 2-3.
59. Bragulla, H.H. and D.G. Homberger, *Structure and functions of keratin proteins in simple, stratified, keratinized and cornified epithelia*. J Anat, 2009. **214**(4): p. 516-59.
60. Plowman, J.E., *The proteomics of keratin proteins*. J Chromatogr B Analyt Technol Biomed Life Sci, 2007. **849**(1-2): p. 181-9.
61. Antunes, E., et al., *The effects of solvent composition on the affinity of a peptide towards hair keratin: experimental and molecular dynamics data*. RSC Adv., 2015. **5**(16): p. 12365-12371.
62. Silva, N.H.C.S., et al., *Protein-based materials: from sources to innovative sustainable materials for biomedical applications*. J. Mater. Chem. B, 2014. **2**(24): p. 3715-3740.
63. Lee, H., et al., *Human hair keratin and its-based biomaterials for biomedical applications*. Tissue Engineering and Regenerative Medicine, 2014. **11**(4): p. 255-265.
64. Arivithamani, N., et al., *Keratin hydrolysate as an exhausting agent in textile reactive dyeing process*. Clean Technol. Environ. Policy, 2014. **16**(6): p. 1207-1215
65. Ghosh, A. and S. Collie, *Keratinous Materials as Novel Absorbent Systems for Toxic Pollutants*. Def. Sci. J., 2014. **64**(3): p. 209-221.
66. Khosa, M.A. and A. Ullah, *A sustainable role of keratin biopolymer in green chemistry: a review*. J. Food Process. Beverages, 2013. **1**(1).
67. Ji, Y., et al., *Extraction of keratin with ionic liquids from poultry feather*. Sep. Purif. Technol., 2014. **132**(20): p. 577-583.
68. Xu, H., Z. Ma, and Y. Yang, *Dissolution and regeneration of wool via controlled disintegration and disentanglement of highly crosslinked keratin*. Journal of Materials Science, 2014. **49**(21): p. 7513-7521.
69. Yu, D., et al., *Modifying surface resistivity and liquid moisture management property of keratin fibers through thiol-ene click reactions*. ACS Appl Mater Interfaces, 2014. **6**(2): p. 1236-42.
70. Yuan, J., et al., *Novel wound dressing based on nanofibrous PHBV-keratin mats*. J Tissue Eng Regen Med, 2012.
71. Sando, L., et al., *Photochemical crosslinking of soluble wool keratins produces a mechanically stable biomaterial that supports cell adhesion and proliferation*. J Biomed Mater Res A, 2010. **95**(3): p. 901-11.
72. Gupta, R., et al., *Biotechnological applications and prospective market of microbial keratinases*. Appl Microbiol Biotechnol, 2013. **97**(23): p. 9931-40.
73. Liu, B., et al., *Expression and characterization of extreme alkaline, oxidation-resistant keratinase from Bacillus licheniformis in recombinant Bacillus subtilis WB600 expression system and its application in wool fiber processing*. World J Microbiol Biotechnol, 2013. **29**(5): p. 825-32.
74. Lopes, F.C., et al., *Production of Proteolytic Enzymes by a Keratin-Degrading Aspergillus niger*. Enzyme Res, 2011. **2011**: p. 487093.
75. Cavello, I.A., et al., *Purification and characterization of a keratinolytic serine protease from Purpureocillium lilacinum LPS # 876*. Process Biochem. (Oxford, U. K.), 2013. **48**(5-6): p. 972-978.
76. Zhang, R. and A. Wang, *Modification of wool by air plasma and enzymes as a cleaner and environmentally friendly process*. J. Cleaner Prod., 2015. **87**(January 2015): p. 961-965.
77. King, R.D. and B.E. Brockway, *Treatment of wool materials*, 1988.
78. Huang, X., R.K. Kobos, and G. Xu, *Peptide-based carbon nanotube hair colorants and their use in hair colorant and cosmetic compositions*, 2005, Google Patents.
79. Norman, K.R., et al., *Covalent bonding of active agents to skin, hair or nails*, 1996, Chesebrough-Pond's USA Co., Division of Conopco, Inc. (Greenwich, CT): US.
80. Green, H., et al., *Attaching agents to tissue with transglutaminase and a transglutaminase substrate*, 2001, Google Patents.
81. Fernandes, M. and A. Cavaco-Paulo, *Protein disulphide isomerase-mediated grafting of cysteine-containing peptides onto over-bleached hair*. Biocatal. Biotransform., 2012. **30**(1): p. 10-19.
82. Fernandes, M.M., et al., *Protein disulphide isomerase-assisted functionalization of keratin-based matrices*. Appl Microbiol Biotechnol, 2011. **90**(4): p. 1311-21.
83. Mohamed, S.A., A.A. Darwish, and R.M. El-Shishtawy, *Immobilization of horseradish peroxidase on activated wool*. Process Biochem. (Oxford, U. K.), 2013. **48**(4): p. 649-655.
84. Mohamed, S.A., et al., *Immobilization of Trichoderma harzianum alpha-amylase on treated wool: optimization and characterization*. Molecules, 2014. **19**(6): p. 8027-38.

85. Liao, J., et al., *Dynamics of human keratin 18 phosphorylation: polarized distribution of phosphorylated keratins in simple epithelial tissues*. J Cell Biol, 1995. **131**(5): p. 1291-301.
86. Pekny, M. and E.B. Lane, *Intermediate filaments and stress*. Exp Cell Res, 2007. **313**(10): p. 2244-54.
87. Yeagle, P.L., J. Frye, and B.S. Eckert, *Phosphorylation modulates keratin structure*. Biochemistry, 1990. **29**(6): p. 1508-14.
88. Bramson, H.N., E.T. Kaiser, and A.S. Mildvan, *Mechanistic studies of cAMP-dependent protein kinase action*. CRC Crit Rev Biochem, 1984. **15**(2): p. 93-124.
89. Tao, M., M.L. Salas, and F. Lipmann, *Mechanism of activation by adenosine 3':5'-cyclic monophosphate of a protein phosphokinase from rabbit reticulocytes*. Proc Natl Acad Sci U S A, 1970. **67**(1): p. 408-14.
90. Adams, J.A., et al., *Phosphorylation modulates catalytic function and regulation in the cAMP-dependent protein kinase*. Biochemistry, 1995. **34**(8): p. 2447-54.
91. Kreegipuu, A., et al., *Statistical analysis of protein kinase specificity determinants*. FEBS Lett, 1998. **430**(1-2): p. 45-50.
92. Cook, P.F., et al., *Adenosine cyclic 3',5'-monophosphate dependent protein kinase: kinetic mechanism for the bovine skeletal muscle catalytic subunit*. Biochemistry, 1982. **21**(23): p. 5794-9.
93. Zhou, J. and J.A. Adams, *Is there a catalytic base in the active site of cAMP-dependent protein kinase?* Biochemistry, 1997. **36**(10): p. 2977-84.
94. Demarche, P., et al., *Harnessing the power of enzymes for environmental stewardship*. Biotechnol Adv, 2012. **30**(5): p. 933-53.
95. D. Kaplan, W.A., B. Farmer and C. Viney, *Silk polymers: material science and biotechnology*. Polym. Adv. Technol., 1995. **6**(11): p. 717.
96. Tanaka, K., et al., *Determination of the site of disulfide linkage between heavy and light chains of silk fibroin produced by Bombyx mori*. Biochim Biophys Acta, 1999. **1432**(1): p. 92-103.
97. Numata, K., S. Yamazaki, and N. Naga, *Biocompatible and biodegradable dual-drug release system based on silk hydrogel containing silk nanoparticles*. Biomacromolecules, 2012. **13**(5): p. 1383-9.
98. Numata, K. and D.L. Kaplan, *Silk-based delivery systems of bioactive molecules*. Adv Drug Deliv Rev, 2010. **62**(15): p. 1497-508.
99. Liu, X., et al., *Blend films of silk fibroin and water-insoluble polyurethane prepared from an ionic liquid*. Mater. Lett., 2011. **65**(15-16): p. 2489-2491.
100. Shang, S., L. Zhu, and J. Fan, *Intermolecular interactions between natural polysaccharides and silk fibroin protein*. Carbohydr Polym, 2013. **93**(2): p. 561-73.
101. Wang, X. and D.L. Kaplan, *Functionalization of silk fibroin with NeutrAvidin and biotin*. Macromol Biosci, 2011. **11**(1): p. 100-10.
102. Karageorgiou, V., et al., *Bone morphogenetic protein-2 decorated silk fibroin films induce osteogenic differentiation of human bone marrow stromal cells*. J Biomed Mater Res A, 2004. **71**(3): p. 528-37.
103. Li, M., M. Ogiso, and N. Minoura, *Enzymatic degradation behavior of porous silk fibroin sheets*. Biomaterials, 2003. **24**(2): p. 357-65.
104. Winkler, S. and D.L. Kaplan, *Molecular biology of spider silk*. J Biotechnol, 2000. **74**(2): p. 85-93.
105. Mandell, D.J., et al., *Strengths of hydrogen bonds involving phosphorylated amino acid side chains*. J Am Chem Soc, 2007. **129**(4): p. 820-7.
106. Westheimer, F.H., *Why nature chose phosphates*. Science, 1987. **235**(4793): p. 1173-8.
107. Tabata, Y., *Biomaterials Design of Culture Substrates for Cell Research*. Inflamm Regen, 2011. **31**: p. 137-145.
108. Mieszawska, A.J. and D.L. Kaplan, *Smart biomaterials - regulating cell behavior through signaling molecules*. BMC Biol, 2010. **8**: p. 59.
109. Dawson, E., et al., *Biomaterials for stem cell differentiation*. Adv Drug Deliv Rev, 2008. **60**(2): p. 215-28.
110. Khorasani, M.T. and H. Mirzadeh, *BHK cells behaviour on laser treated polydimethylsiloxane surface*. Colloids Surf B Biointerfaces, 2004. **35**(1): p. 67-71.
111. Hu, X., et al., *Biomaterials derived from silk-tropoelastin protein systems*. Biomaterials, 2010. **31**(32): p. 8121-31.
112. Samuel, D. and B.L. Silver, *Elimination reactions and hydrolysis of serine phosphate*. J. Chem. Soc., 1963(0): p. 289-296.
113. Geladopoulos, T.P., T.G. Sotiroudis, and A.E. Evangelopoulos, *A malachite green colorimetric assay for protein phosphatase activity*. Anal Biochem, 1991. **192**(1): p. 112-6.
114. O'Toole, M., et al., *Determination of phosphate using a highly sensitive paired emitter-detector diode photometric flow detector*. Anal Chim Acta, 2007. **597**(2): p. 290-4.

115. D'Angelo, E., J. Crutchfield, and M. Vandiviere, *Rapid, sensitive, microscale determination of phosphate in water and soil*. J Environ Qual, 2001. **30**(6): p. 2206-9.
116. Huang, H.D., et al., *KinasePhos: a web tool for identifying protein kinase-specific phosphorylation sites*. Nucleic Acids Res, 2005. **33**(Web Server issue): p. W226-9.
117. Xue, Y., et al., *PPSP: prediction of PK-specific phosphorylation site with Bayesian decision theory*. BMC Bioinformatics, 2006. **7**: p. 163.
118. Kong, J. and S. Yu, *Fourier transform infrared spectroscopic analysis of protein secondary structures*. Acta Biochim Biophys Sin (Shanghai), 2007. **39**(8): p. 549-59.
119. Silva, R., et al., *Protein microspheres as suitable devices for piroxicam release*. Colloids Surf B Biointerfaces, 2012. **92**: p. 277-85.
120. Higuchi, T., *Mechanism of sustained-action medication. Theoretical analysis of rate of release of solid drugs dispersed in solid matrices*. J. Pharm. Sci., 1963. **52**(12): p. 1145-1149.
121. Ann H. Cory, J.G.C., *5-(3-carboxymethoxyphenyl)-2-(4,5-dimethylthiazolyl)-3-(4-sulfophenyl)tetrazolium, inner salt (MTS) and related analogs of 3-(4,5-dimethylthiazolyl)-2,5-diphenyltetrazolium bromide (MTT) reducing to purple water-soluble formazans As cell-viability indicators*. Bioorg. Med. Chem. Lett., 1991. **1**(11): p. 611-614.
122. Skehan, P., et al., *New colorimetric cytotoxicity assay for anticancer-drug screening*. J Natl Cancer Inst, 1990. **82**(13): p. 1107-12.
123. Motomizu, S. and Z.H. Li, *Trace and ultratrace analysis methods for the determination of phosphorus by flow-injection techniques*. Talanta, 2005. **66**(2): p. 332-40.
124. Tsukada M, G.Y., Nagura M, Minoura N, Kasai N, Freddi G, *Structural changes of silk fibroin membranes induced by immersion in methanol aqueous solutions*. J. Polym. Sci., Part B: Polym. Phys., 1994. **32**(5): p. 961-968.
125. N. V. Bhat, S.M.A., *Investigation of the structure of silk film regenerated with lithium thiocyanate solution*. J. Polym. Sci., Part A: Polym. Chem., 1983. **21**(5): p. 1273-1280.
126. Mo, C., et al., *Near-infrared characterization on the secondary structure of regenerated Bombyx mori silk fibroin*. Appl Spectrosc, 2006. **60**(12): p. 1438-41.
127. Silva, R.A., et al., *Discriminating 3(10)- from alpha-helices: vibrational and electronic CD and IR absorption study of related Aib-containing oligopeptides*. Biopolymers, 2002. **65**(4): p. 229-43.
128. Ha, S.W., A.E. Tonelli, and S.M. Hudson, *Structural studies of Bombyx mori silk fibroin during regeneration from solutions and wet fiber spinning*. Biomacromolecules, 2005. **6**(3): p. 1722-31.
129. Fuller, A.A., et al., *Evaluating beta-turn mimics as beta-sheet folding nucleators*. Proc Natl Acad Sci U S A, 2009. **106**(27): p. 11067-72.
130. Motta, A., L. Fambri, and C. Migliaresi, *Regenerated Silk Fibroin Films: Thermal and Dynamic Mechanical Analysis*. Macromol Chem Phys, 2002. **203**(10-11): p. 1658-1665.
131. Budhavaram, N.K., et al., *Protein substitution affects glass transition temperature and thermal stability*. J Agric Food Chem, 2010. **58**(17): p. 9549-55.
132. Bruylants, G., J. Wouters, and C. Michaux, *Differential scanning calorimetry in life science: thermodynamics, stability, molecular recognition and application in drug design*. Curr Med Chem, 2005. **12**(17): p. 2011-20.
133. Magoshi, J., et al., *Physical properties and structure of silk. V. Thermal behavior of silk fibroin in the random-coil conformation*. J. Polym. Sci., Polym. Phys. Ed., 1977. **15**(9): p. 1675-1683.
134. Magoshi, J. and S. Nakamura, *Studies on physical properties and structure of silk. Glass transition and crystallization of silk fibroin*. J. Appl. Polym. Sci., 1975. **19**(4): p. 1013-1015.
135. Aminuddin, M., U. Nazim, and I. Ahmad, *Photo- and thermal degradation of piroxicam in aqueous solution*. Indian J Pharm Sci, 2011. **73**(4): p. 387-91.
136. Costa, P. and J.M. Sousa Lobo, *Modeling and comparison of dissolution profiles*. Eur J Pharm Sci, 2001. **13**(2): p. 123-33.
137. Kamlesh, K., S. Charu, and K. Patit, *In-vitro Release of Metformin Hydrochloride from Films of Chitosan-Methylcellulose Blends*. Asian J. Chem., 2009. **21**(10): p. 148-152.
138. Mann H.B., W.D.R., *On a Test of Whether one of Two Random Variables is Stochastically Larger than the Other*. Ann. Math. Stat., 1947. **18**(1): p. 50-60.
139. Liu, T.L., et al., *Cytocompatibility of regenerated silk fibroin film: a medical biomaterial applicable to wound healing*. J Zhejiang Univ Sci B, 2010. **11**(1): p. 10-6.
140. Mai-ngam, K., et al., *Evaluation of the properties of silk fibroin films from the non-mulberry silkworm Samia cynthia ricini for biomaterial design*. J Biomater Sci Polym Ed, 2011. **22**(15): p. 2001-22.

141. Polyansky A.A, Z.B., *Protein Electrostatic Properties Predefining the Level of Surface Hydrophobicity Change upon Phosphorylation*. J. Phys. Chem. Lett., 2012. **3**(8): p. 973–976.
142. Ganguly, D. and J. Chen, *Atomistic details of the disordered states of KID and pKID. Implications in coupled binding and folding*. J Am Chem Soc, 2009. **131**(14): p. 5214-23.
143. Potoyan, D.A. and G.A. Papoian, *Energy landscape analyses of disordered histone tails reveal special organization of their conformational dynamics*. J Am Chem Soc, 2011. **133**(19): p. 7405-15.
144. Śmiechowski, M., *Theoretical pKa prediction of O-phosphoserine in aqueous solution*. Chem. Phys. Lett., 2011. **514**(4-6): p. 123-129.
145. C. Wong Po Foo, E.B., J. Hensman, D.P. Knight, R.V. Lewis, D.L. Kaplan, *Role of pH and charge on silk protein assembly in insects and spiders*. Applied Physics A, 2006. **82**(2): p. 223-233.
146. Yang, A.S. and B. Honig, *On the pH dependence of protein stability*. J Mol Biol, 1993. **231**(2): p. 459-74.
147. Krisztina Takács-Novák1, J.K., Benjámín Podányi, Béla Noszál, Ruey-Shiuan Tsai, Giuseppe Lisa, Pierre-Alain Carrupt, Bernard Testa, *Microscopic Protonation/Deprotonation Equilibria of the Anti-Inflammatory Agent Piroxicam*. Helvetica Chimica Acta, 1995. **78**(3): p. 553–562.
148. Hofmann, S., et al., *Silk fibroin as an organic polymer for controlled drug delivery*. J Control Release, 2006. **111**(1-2): p. 219-27.
149. Khorasani, M.T., et al., *Effect of surface charge and hydrophobicity of polyurethanes and silicone rubbers on L929 cells response*. Colloids Surf B Biointerfaces, 2006. **51**(2): p. 112-9.
150. Hezi-Yamit, A., et al., *Impact of polymer hydrophilicity on biocompatibility: implication for DES polymer design*. J Biomed Mater Res A, 2009. **90**(1): p. 133-41.
151. Richards, D. and A. Ivanisevic, *Inorganic material coatings and their effect on cytotoxicity*. Chem Soc Rev, 2012. **41**(6): p. 2052-60.
152. Chiao, E., et al., *Derivation of human embryonic stem cells in standard and chemically defined conditions*. Methods Cell Biol, 2008. **86**: p. 1-14.
153. Shen, M. and T.A. Horbett, *The effects of surface chemistry and adsorbed proteins on monocyte/macrophage adhesion to chemically modified polystyrene surfaces*. J Biomed Mater Res, 2001. **57**(3): p. 336-45.
154. Kundu, S.C., et al., *Invited review nonmulberry silk biopolymers*. Biopolymers, 2012. **97**(6): p. 455-67.
155. Kundu, B., et al., *Silk fibroin biomaterials for tissue regenerations*. Adv Drug Deliv Rev, 2013. **65**(4): p. 457-70.
156. Bhattacharjee, M., et al., *The role of 3D structure and protein conformation on the innate and adaptive immune responses to silk-based biomaterials*. Biomaterials, 2013. **34**(33): p. 8161-71.
157. Volkov, V., et al., *Phosphorylation of silk fibroins improves the cytocompatibility of silk fibroin derived materials: A platform for the production of tuneable material*. Biotechnol J, 2014. **9**(10): p. 1267–1278.
158. Duthie, S.J., *Folic-acid-mediated inhibition of human colon-cancer cell growth*. Nutrition, 2001. **17**(9): p. 736-7.
159. Belur, L.R., et al., *Methotrexate Accumulates to Similar Levels in Animals Transplanted with Normal versus Drug-resistant Transgenic Marrow*. Cancer Res., 2001. **61**: p. 1522–1526.
160. Widemann, B.C. and P.C. Adamson, *Understanding and managing methotrexate nephrotoxicity*. Oncologist, 2006. **11**(6): p. 694-703.
161. Banerjee, D., et al., *Novel aspects of resistance to drugs targeted to dihydrofolate reductase and thymidylate synthase*. Biochim Biophys Acta, 2002. **1587**(2-3): p. 164-73.
162. Miao, B., C. Song, and G. Ma, *Injectable thermosensitive hydrogels for intra-articular delivery of methotrexate*. J. Appl. Polym. Sci., 2011. **122**(3): p. 2139–2145.
163. Zhang, X., F. Chen, and J. Ni, *A novel method to prepare magnetite chitosan microspheres conjugated with methotrexate (MTX) for the controlled release of MTX as a magnetic targeting drug delivery system*. Drug Deliv, 2009. **16**(5): p. 280-8.
164. Cascone, M.G., et al., *Gelatin nanoparticles produced by a simple W/O emulsion as delivery system for methotrexate*. J. Mater. Sci. - Mater. Med., 2002. **13**(5): p. 523-526.
165. Nogueira, D.R., et al., *In vitro antitumor activity of methotrexate via pH-sensitive chitosan nanoparticles*. Biomaterials, 2013. **34**(11): p. 2758-72.
166. Abdelbary, G. and M. Haider, *In vitro characterization and growth inhibition effect of nanostructured lipid carriers for controlled delivery of methotrexate*. Pharm. Dev. Technol., 2013. **18**(5): p. 1159-1168
167. Chau, Y., F.E. Tan, and R. Langer, *Synthesis and characterization of dextran-peptide-methotrexate conjugates for tumor targeting via mediation by matrix metalloproteinase II and matrix metalloproteinase IX*. Bioconj Chem, 2004. **15**(4): p. 931-41.

168. Subia, B. and S.C. Kundu, *Drug loading and release on tumor cells using silk fibroin-albumin nanoparticles as carriers*. Nanotechnology, 2013. **24**(3): p. 035103.
169. Mathur, A.B., et al., *Preparation and methodology of silk fibroin nanoparticles*, 2011, Google Patents.
170. Lammel, A., et al., *Silk particles for controlled and sustained delivery of compounds*, 2011, Google Patents.
171. Ochi, A., et al., *Rheology and dynamic light scattering of silk fibroin solution extracted from the middle division of Bombyx mori silkworm*. Biomacromolecules, 2002. **3**(6): p. 1187-96.
172. Lehermayr, C., et al., *Assessment of net charge and protein-protein interactions of different monoclonal antibodies*. J Pharm Sci, 2011. **100**(7): p. 2551-62.
173. Matsumoto, A., et al., *Silk fibroin solution properties related to assembly and structure*. Macromol Biosci, 2008. **8**(11): p. 1006-18.
174. Vasconcelos, A., G. Freddi, and A. Cavaco-Paulo, *Biodegradable materials based on silk fibroin and keratin*. Biomacromolecules, 2008. **9**(4): p. 1299-305.
175. de Oliveira, A.R., et al., *Structural and thermal properties of spray-dried methotrexate-loaded biodegradable microparticles*. J. Therm. Anal. Calorim., 2013. **112**(2): p. 555-565.
176. Chadha, R., et al., *Characterization of solvatomorphs of methotrexate using thermoanalytical and other techniques*. Acta Pharm, 2009. **59**(3): p. 245-57.
177. Munday, D.L. and P.J. Cox, *Compressed xanthan and karaya gum matrices: hydration, erosion and drug release mechanisms*. Int J Pharm, 2000. **203**(1-2): p. 179-92.
178. Ritger, P.L. and N.A. Peppas, *A simple equation for description of solute release II. Fickian and anomalous release from swellable devices*. J. Controlled Release, 1987. **5**(1): p. 37-42.
179. Alfrey, T., E.F. Gurnee, and W.G. Lloyd, *Diffusion in glassy polymers*. J. Polym. Sci., C Polym. Symp., 1966. **12**(1): p. 249-261.
180. Lee, I.P., *Kinetics of drug release from hydrogel matrices*. J. Control. Release, 1985. **2**: p. 277-288.
181. Wu, C.Y. and L.Z. Benet, *Predicting drug disposition via application of BCS: transport/absorption/elimination interplay and development of a biopharmaceutics drug disposition classification system*. Pharm Res, 2005. **22**(1): p. 11-23.
182. Fu, Y. and W.J. Kao, *Drug release kinetics and transport mechanisms of non-degradable and degradable polymeric delivery systems*. Expert Opin Drug Deliv, 2010. **7**(4): p. 429-44.
183. Bahga, S.S., M. Bercovici, and J.G. Santiago, *Ionic strength effects on electrophoretic focusing and separations*. Electrophoresis, 2010. **31**(5): p. 910-9.
184. Dobrynin, A.V. and M. Rubinstein, *Theory of polyelectrolytes in solutions and at surfaces*. Progress in Polymer Science, 2005. **30**(11): p. 1049-1118.
185. Alves, N.M., et al., *Glass transition and structural relaxation in semi-crystalline poly(ethyleneterephthalate): a DSC study*. Polymer, 2002. **43**(15): p. 4111-4122.
186. Narladkar, A., et al., *Difference in Glass Transition Behavior Between Semi Crystalline and Amorphous poly(lactic acid) Thin Films*. Macromol. Symp., 2008. **273**(1): p. 146-152.
187. Keddie, J.L., R.A.L. Jones, and R.A. Cory, *Size-Dependent Depression of the Glass Transition Temperature in Polymer Films*. Europhys. Lett., 1994. **27**(1): p. 59-64.
188. Kishida, A., et al., *Polymer drugs and polymeric drugs X: Slow release of B-fluorouracil from biodegradable poly(γ -glutamic acid) and its benzyl ester matrices*. J. Bioact. Compat. Polym., 1998. **13**(4): p. 270-278.
189. Mallapragada, S.K., N.A. Peppas, and P. Colombo, *Crystal dissolution-controlled release systems. II. Metronidazole release from semicrystalline poly(vinyl alcohol) systems*. J Biomed Mater Res, 1997. **36**(1): p. 125-30.
190. Jalil, R. and J.R. Nixon, *Biodegradable poly(lactic acid) and poly(lactide-co-glycolide) microcapsules: problems associated with preparative techniques and release properties*. J Microencapsul, 1990. **7**(3): p. 297-325.
191. Ahmed, A.R., A. Dashevsky, and R. Bodmeier, *Reduced burst effect in drug release with solvent-treated microparticles prepared by the solvent evaporation method*. Proc. Int. Symp. Control. Release Bioact. Mater., 2000. **27**: p. 6112.
192. Ranga Rao, K.V., K. Padmalatha Devi, and P. Buri, *Cellulose Matrices for Zero-Order Release of Soluble Drugs*. Drug Dev. Ind. Pharm., 1988. **14**(15-17): p. 2299-2320.
193. Gierszewska-Drużyńska, M. and J. Ostrowska-Czubenko, *Mechanism of water diffusion into noncrosslinked and ionically crosslinked chitosan membranes*. PCACD (Poland), 2012. **17**: p. 59-66.

194. Brazel, C.S. and N.A. Peppas, *Mechanisms of solute and drug transport in relaxing, swellable, hydrophilic glassy polymers*. *Polymer*, 1998. **40**(12): p. 3383–3398.
195. Kono, K., M. Liu, and J.M. Frechet, *Design of dendritic macromolecules containing folate or methotrexate residues*. *Bioconjug Chem*, 1999. **10**(6): p. 1115-21.
196. Szakacs, Z. and B. Noszal, *Determination of dissociation constants of folic acid, methotrexate, and other photolabile pteridines by pressure-assisted capillary electrophoresis*. *Electrophoresis*, 2006. **27**(17): p. 3399-409.
197. Lu, S., et al., *Insoluble and flexible silk films containing glycerol*. *Biomacromolecules*, 2010. **11**(1): p. 143-50.
198. Zhang, C., et al., *Flexibility regeneration of silk fibroin in vitro*. *Biomacromolecules*, 2012. **13**(7): p. 2148-53.
199. Pritchard, E.M., et al., *Effect of silk protein processing on drug delivery from silk films*. *Macromol Biosci*, 2013. **13**(3): p. 311-20.
200. Lu, Q., et al., *Water-insoluble silk films with silk I structure*. *Acta Biomater*, 2010. **6**(4): p. 1380-7.
201. Wang, X., et al., *Nanolayer biomaterial coatings of silk fibroin for controlled release*. *J Control Release*, 2007. **121**(3): p. 190-9.
202. Motta, A., et al., *Silk fibroin processing and thrombogenic responses*. *J Biomater Sci Polym Ed*, 2009. **20**(13): p. 1875-97.
203. Hu, X., D. Kaplan, and P. Cebe, *Dynamic Protein–Water Relationships during β -Sheet Formation*. *Macromolecules*, 2008. **41**(11): p. 3939–3948.
204. Wang, X., et al., *Sonication-induced gelation of silk fibroin for cell encapsulation*. *Biomaterials*, 2008. **29**(8): p. 1054-64.
205. Miranda-Vilela, A.L., A.J. Botelho, and L.A. Muehlmann, *An overview of chemical straightening of human hair: technical aspects, potential risks to hair fibre and health and legal issues*. *Int J Cosmet Sci*, 2013.
206. Weathersby, C. and A. McMichael, *Brazilian keratin hair treatment: a review*. *J Cosmet Dermatol*, 2013. **12**(2): p. 144-8.
207. Reichl, S., *Films based on human hair keratin as substrates for cell culture and tissue engineering*. *Biomaterials*, 2009. **30**(36): p. 6854-66.
208. Burnett, L.R., et al., *Novel keratin (KeraStat) and polyurethane (Nanosan(R)-Sorb) biomaterials are hemostatic in a porcine lethal extremity hemorrhage model*. *J Biomater Appl*, 2014. **28**(6): p. 869-79.
209. Reichl, S., M. Borrelli, and G. Geerling, *Keratin films for ocular surface reconstruction*. *Biomaterials*, 2011. **32**(13): p. 3375-86.
210. Kar, P. and M. Misra, *Use of keratin fiber for separation of heavy metals from water*. *J. Chem. Technol. Biotechnol.*, 2004. **79**(11): p. 1313–1319.
211. Mittal, A., *Use of hen feathers as potential adsorbent for the removal of a hazardous dye, Brilliant Blue FCF, from wastewater*. *J Hazard Mater*, 2006. **128**(2-3): p. 233-9.
212. Aluigi, A., et al., *Study on the adsorption of chromium (VI) by hydrolyzed keratin/polyamide 6 blend nanofibres*. *J Nanosci Nanotechnol*, 2012. **12**(9): p. 7250-9.
213. King, R.D. and B.E. Brockway, *Treatment of wool materials*, 1988, Google Patents.
214. Fernandes, M. and A. Cavaco-Paulo, *Protein Disulphide Isomerase-assisted grafting of cysteine-containing peptides*. *Biocatal. Biotransform.*, 2012. **30**(1): p. 10-19.
215. Strnad, P., R. Windoffer, and R.E. Leube, *Induction of rapid and reversible cytokeratin filament network remodeling by inhibition of tyrosine phosphatases*. *J Cell Sci*, 2002. **115**(Pt 21): p. 4133-48.
216. Sun, T.T. and H. Green, *Keratin filaments of cultured human epidermal cells. Formation of intermolecular disulfide bonds during terminal differentiation*. *J Biol Chem*, 1978. **253**(6): p. 2053-60.
217. Inagaki, M., et al., *Intermediate filament reconstitution in vitro. The role of phosphorylation on the assembly-disassembly of desmin*. *J Biol Chem*, 1988. **263**(12): p. 5970-8.
218. Holmes, E.J., *Hot, acidified rhodamine B and methylene blue; a differential stain dichromatic for hair follicular keratins, achromatic for epidermal keratin*. *Stain Technol*, 1970. **45**(1): p. 15-8.
219. Floyd, R.A., J.E. Schneider, Jr., and D.P. Dittmer, *Methylene blue photoinactivation of RNA viruses*. *Antiviral Res*, 2004. **61**(3): p. 141-51.
220. Dabrowski, A., *Adsorption - its development and application for practical purposes*, in *Adsorption and its Applications in Industry and Environmental Protection: Applications in Industry*, A. Dabrowski, Editor. 1998, Elsevier Science Ltd: Netherlands. p. 3-16.
221. Nylander, T., Y. Samoshina, and B. Lindman, *Formation of polyelectrolyte–surfactant complexes on surfaces*. *Adv. Colloid Interface Sci.*, 2006. **123-126**: p. 105–123.

222. Gupta, V.K. and Suhas, *Application of low-cost adsorbents for dye removal – A review*. J. Environ. Manage., 2009. **90**(8): p. 2313–2342.
223. Dabrowski, A., *Theoretical foundations of physical adsorption from binary non-electrolytic liquid mixtures on solid surfaces: present and future*. Adv. Colloid Interface Sci., 1987. **27**(3-4): p. 211.
224. El-Khaiary, M.I., *Least-squares regression of adsorption equilibrium data: Comparing the options*. J. Hazard. Mater., 2008. **158**(1): p. 73-87.
225. Aluigi, A., et al., *Study of Methylene Blue adsorption on keratin nanofibrous membranes*. J Hazard Mater, 2014. **268**: p. 156-65.
226. Chen, H., et al., *Isotherm, thermodynamic, kinetics and adsorption mechanism studies of methyl orange by surfactant modified silkworm exuviae*. J Hazard Mater, 2011. **192**(1): p. 246-54.
227. Barth, A. and C. Zscherp, *What vibrations tell us about proteins*. Q Rev Biophys, 2002. **35**(4): p. 369-430.
228. Negri, A.P., H.J. Cornell, and D.E. Rivett, *A Model for the Surface of Keratin Fibers*. Text. Res. J., 1993. **63**(2): p. 109-115.
229. Fathi, F., et al., *Studies of the interaction of two organophosphonates with nanostructured silver surfaces*. Analyst, 2012. **137**(19): p. 4448-4453.
230. Anderson, M.S., et al., *Fourier transform infrared spectroscopy for Mars science*. Rev. Sci. Instrum., 2005. **76**(034101): p. 1-9.
231. Nakamura, A., et al., *A rapid extraction procedure of human hair proteins and identification of phosphorylated species*. Biol Pharm Bull, 2002. **25**(5): p. 569-72.
232. Kannan, N. and M.M. Sundaram, *Kinetics and mechanism of removal of methylene blue by adsorption on various carbons—a comparative study*. Dyes Pigm., 2001. **51**(1): p. 25-40.
233. Ran, G., et al., *The adsorption behavior of cationic surfactant onto human hair fibers*. Colloids Surf B Biointerfaces, 2009. **68**(1): p. 106-10.
234. Dabrowski, A., *Adsorption—from theory to practice*. Adv Colloid Interface Sci, 2001. **93**(1-3): p. 135-224.
235. Chen, H., J. Zhao, and G. Dai, *Silkworm exuviae—a new non-conventional and low-cost adsorbent for removal of methylene blue from aqueous solutions*. J Hazard Mater, 2011. **186**(2-3): p. 1320-7.
236. Papageorgiou, S.K., et al., *Heavy metal sorption by calcium alginate beads from Laminaria digitata*. J Hazard Mater, 2006. **137**(3): p. 1765-72.
237. Hobson, J.P., *Physical adsorption isotherms extending from ultrahigh vacuum to vapor pressure*, 1969. **73**(8): p. 2720–2727.
238. Helfferich, F., *Ion Exchange*. 1962, New York: McGraw-Hill Book Co. Inc.
239. Khan, A.R., et al., *Adsorption of methylene blue from aqueous solution on the surface of wool fiber and cotton fiber*. J. Appl. Sci. Environ. Mgt., 2005. **9**(2): p. 29-35.
240. Gao, L. and H. Gao, *Haematoxylin sorption onto yak hair: kinetic and thermodynamic studies*. . Color. Technol., 2014. **130**(1): p. 21-26.
241. Suteu, D. and T. Malutan, *Industrial Cellulignin Wastes as Adsorbent for Removal of Methylene Blue Dye from Aqueous Solutions*. BioResources, 2013. **8**(1): p. 427-446.
242. Akkayaa, G. and F. Güzel, *Application of Some Domestic Wastes as New Low-Cost Biosorbents for Removal of Methylene Blue: Kinetic and Equilibrium Studies*. Chem. Eng. Commun., 2014. **201**(4): p. 557-578.
243. Aroguz, A.Z., J. Gulen, and R.H. Evers, *Adsorption of methylene blue from aqueous solution on pyrolyzed petrified sediment*. Bioresour. Technol., 2007. **99**(6): p. 1503–1508.
244. Volkov, V., et al., *Phosphorylated silk fibroin matrix for methotrexate release*. Mol Pharm, 2015. **12**(1): p. 75-86.
245. Tate, M.L., et al., *Quantification and prevention of hair damage*. J. Soc. Cosmet. Chem., 1993. **44**(6): p. 347-371.
246. Ali, N., et al., *Accepted Article*. DOI: 10.1111/ics.12201. Int. J. Cosmet. Sci., 2015.
247. Shacter, E., *Protein oxidative damage*. Methods Enzymol, 2000. **319**: p. 428-36.
248. Wolfram, L.J., *Human hair: a unique physicochemical composite*. J Am Acad Dermatol, 2003. **48**(6 Suppl): p. S106-14.
249. Armaroli, T., T. Bécue, and S. Gautier, *Diffuse Reflection Infrared Spectroscopy (Drifts): Application to the in Situ Analysis of Catalysts*. Oil Gas Sci. Technol., 2004. **59**(2): p. 215-237
250. Bellamy, L.J. and L. Beecher, *The infrared spectra of some organophosphorus esters*. J. Chem. Soc., 1952: p. 475-483.
251. Salisbury, J.W. and A. Wald, *The role of volume scattering in reducing spectral contrast of reststrahlen bands in spectra of powdered minerals*. Icarus, 1992. **96**(1): p. 121–128.

252. Durham, D.R., D.B. Stewart, and E.J. Stellwag, *Novel alkaline- and heat-stable serine proteases from alkalophilic Bacillus sp. strain GX6638*. J Bacteriol, 1987. **169**(6): p. 2762-8.
253. Mekmene, O., et al., *Effects of pH and Ca/P molar ratio on the quantity and crystalline structure of calcium phosphates obtained from aqueous solutions*. Dairy Sci. Technol., 2009. **89**(3-4): p. 301-316.
254. Eckert, B.S. and P.L. Yeagle, *Site-specificity of ethanol-induced dephosphorylation of rat hepatocyte keratins 8 and 18: A 31P NMR study*. Cell Motil Cytoskeleton, 1996. **33**(1): p. 30-7.
255. Marshall, R.C., *Characterization of the proteins of human hair and nail by electrophoresis*. J Invest Dermatol, 1983. **80**(6): p. 519-24.
256. Ho, Y.S., J.C.-Y. Ng, and G. McKay, *Kinetics of pollutant sorption by biosorbents: review*. Sep. Purif. Rev., 2000. **29**(2): p. 189-232.
257. Liu, Y. and L. Shen, *From Langmuir kinetics to first- and second-order rate equations for adsorption*. Langmuir, 2008. **24**(20): p. 11625-30.
258. Jaycock, M.J. and G.D. Parfitt, *Chemistry of Interfaces*. 1981, Onichester: Ellis Horwood Ltd.
259. Turgeon, S.L., C. Schmitt, and C. Sanchez, *Protein-polysaccharide complexes and coacervates*. Curr. Opin. Colloid Interface Sci., 2007. **12**(4-5): p. 166-178.
260. Imai, T., *The influence of hair bleach on the ultrastructure of human hair with special reference to hair damage*. Okajimas Folia Anat Jpn, 2011. **88**(1): p. 1-9.
261. Fangueiro, R., et al., *Fibrous based materials in sustainable civil and architectural applications – a review*, in *INTERNATIONAL CONFERENCE ON ENGINEERING – ICEUB2011.*, 2011, RepositoriUM, Uminho: University of Beira Interior – Covilhã, Portugal.
262. Fujihara, K., et al., *Fibrous composite materials in dentistry and orthopaedics: review and applications*. Compos. Sci. Technol., 2004. **64**(6): p. 775-788.
263. Novoselova, L.Y. and E.E. Sirotkina, *Polyolefinic Fibrous Ion-Exchange Materials: Properties and Applications (Review)*. Chem. Sustainable Dev., 2006. **14**: p. 199-213.
264. Puglia, D., J. Biagiotti, and J.M. Kenny, *A Review on Natural Fibre-Based Composites—Part II*. J. Nat. Fibers, 2005. **1**(3): p. 23-65.
265. Biagiotti, J., D. Puglia, and J.M. Kenny, *A Review on Natural FibreBased Composites - Part I*. J. Nat. Fibers, 2004. **1**(2): p. 37-68.
266. Lintz, E.S. and T.R. Scheibel, *Dragline, Egg Stalk and Byssus: A Comparison of Outstanding Protein Fibers and Their Potential for Developing New Materials*. Advanced Functional Materials, 2013. **23**(36): p. 4467-4482.
267. Böckmann, A. and B.H. Meier, *Structural Studies of Protein Fibrils by Solid-State NMR*, in *NMR of Biomolecules*. 2012, Wiley-VCH Verlag GmbH & Co. KGaA. p. 394-405.
268. Khurana, P. and V.G. Checker, *The advent of genomics in mulberry and perspectives for productivity enhancement*. Plant Cell Rep, 2011. **30**(5): p. 825-38.
269. Yucel, T., M.L. Lovett, and D.L. Kaplan, *Silk-based biomaterials for sustained drug delivery*. J Control Release, 2014. **190**: p. 381-97.
270. Höfer, R. and M. Selig, *10.02 - Green chemistry and green polymer chemistry*, in *Polymer Science: A Comprehensive Reference*, K. Matyjaszewski and M. Möller, Editors. 2012, Elsevier B.V. p. 5-12.
271. Bononi, A., et al., *Protein kinases and phosphatases in the control of cell fate*. Enzyme Res, 2011. **2011**: p. 329098.
272. Xin, F. and P. Radivojac, *Post-translational modifications induce significant yet not extreme changes to protein structure*. Bioinformatics, 2012. **28**(22): p. 2905-13.
273. Chen, W.Q., et al., *Silk cocoon of Bombyx mori: proteins and posttranslational modifications--heavy phosphorylation and evidence for lysine-mediated cross links*. Proteomics, 2010. **10**(3): p. 369-79.
274. Zhang, P., et al., *Proteome analysis of silk gland proteins from the silkworm, Bombyx mori*. Proteomics, 2006. **6**(8): p. 2586-99.
275. Klapperstuck, T., et al., *Calibration procedures for the quantitative determination of membrane potential in human cells using anionic dyes*. Cytometry A, 2013. **83**(7): p. 612-26.
276. Emri, M., et al., *Wide applicability of a flow cytometric assay to measure absolute membrane potentials on the millivolt scale*. Eur. Biophys. J., 1998. **28**(1): p. 78-83.
277. Laatsch, C.N., et al., *Human hair shaft proteomic profiling: individual differences, site specificity and cuticle analysis*. PeerJ, 2014. **2**: p. e506.
278. Khan, I., et al., *Mammalian keratin associated proteins (KRTAPs) subgenomes: disentangling hair diversity and adaptation to terrestrial and aquatic environments*. BMC Genomics, 2014. **15**: p. 779.
279. Shih, Y.L. and L. Rothfield, *The bacterial cytoskeleton*. Microbiol Mol Biol Rev, 2006. **70**(3): p. 729-54.

280. Gavazzoni Dias, M.F., et al., *The Shampoo pH can Affect the Hair: Myth or Reality?* Int J Trichology, 2014. **6**(3): p. 95-9.
281. Jegannathan, K.R. and P.H. Nielsen, *Environmental assessment of enzyme use in industrial production – a literature review.* J. Cleaner Prod., 2013. **42**(March 2013): p. 228–240.
282. Kiss, G., et al., *Computational Enzyme Design.* Computational Enzyme Design. Angew. Chem. Int. Ed., 2013. **52**(22): p. 5700–5725.
283. Zanghellini, A., *de novo computational enzyme design.* Curr Opin Biotechnol, 2014. **29**: p. 132-8.